Development of Electrospun Nanofibrous Silk Fibroin Based Scaffolds for Bone Tissue Engineering

A THESIS SUBMITTED FOR AWARD OF THE DEGREE OF

Doctor of Philosophy

in

Biotechnology and Medical Engineering

by

NILADRI NATH PANDA

(Roll no. 509BM102)

Under the guidance of

Prof. Amit Biswas and Prof. Krishna Pramanik

Department of Biotechnology & Medical Engineering

National Institute of Technology, Rourkela

Development of Electrospun Nanofibrous Silk Fibroin Based Scaffolds for Bone Tissue Engineering

A THESIS SUBMITTED FOR AWARD OF THE DEGREE OF

Doctor of Philosophy

in

Biotechnology and Medical Engineering

by

NILADRI NATH PANDA

(Roll no. 509BM102)

Under the guidance of

Prof. Amit Biswas and Prof. Krishna Pramanik

Department of Biotechnology & Medical Engineering

National Institute of Technology, Rourkela

NATIONAL INSTITUTE OF TECHNOLOGY, ROURKELA

ROURKELA-769 008, ODISHA

Certificate

This is to certify that the thesis entitled, ***"Development of electrospun nanofibrous silk fibroin based scaffolds for bone Tissue Engineering"*** submitted by ***Niladri Nath Panda (509BM102)*** for the award of ***Doctor of Philosophy in Biotechnology & Medical Engineering*** at National Institute of Technology, Rourkela is an authentic work carried out by him under our guidance and supervision. The candidate has fulfilled all prescribed requirements for Ph.D. dissertation. To the best of our knowledge, the matter embodied in the thesis is based on candidate's own work and the thesis has not been submitted to any other university/institute for the award of any degree or diploma.

Dr. (Mrs.) Krishna Pramanik
Professor
Dept. of Biotechnology & Medical Engineering
National Institute of Technology
Rourkela-769 008
Odisha, INDIA

Dr. Amit Biswas
Asst. Professor
Dept. of Biotechnology & Medical Engineering
National Institute of Technology
Rourkela-769 008
Odisha, INDIA

Acknowledgements

First of all I would like to thank my supervisors Prof. Amit Biswas and Prof. Krishna Pramanik for accepting me as a doctoral student when I was struggling with my career. Thanks to both of you so much for being a strong support to me both in academic world and outside academia too. I will always cherish the patience of Prof. Krishna Pramanik to listen to my rapid conversations and her cool replies to all my queries without which these four years journey would have been a really difficult task. Thanks a lot for enriching my knowledge in Tissue Engineering that made my research easier despite my little background. Thanks a lot for everything you have done for me. I would like to thank my supervisor Dr. Amit Biswas for his relentless effort in finding out my faults and being the best critic to explanation of my work and for having valuable discussions during the whole course of research. I would like to praise his active efforts during the final stage of my thesis submission.

My special thanks are due to Prof. Sunil Kumar Sarangi, Director, National Institute of Technology, Rourkela for all the facilities provided to successfully complete this work.

I am also very thankful to all the members of my doctoral scrutiny committee - Prof. S. Paul and Prof. K. Pal, Department of Biotechnology and Medical Engineering, Prof. B.C.Roy, Department of Metallurgy and Material Engineering, Prof. M. Kundu, Department of Chemical Engineering, for their suggestion, inspiration and encouragement throughout the research work. I am also taking the opportunity to thank other faculty members and supporting staff members of the Department of Biotechnology and Medical Engineering for their timely cooperation and support at various phases of experimental work.

My special thanks to my uncle Mr. L.B.Sukla, Scientist-G and Head of the Biominerals Division, Institute of Minerals and Materials Technology, Bhubaneswar, India for his constant encouragement and support for this work. I would also like to thank all my friends in National Institute of Technology, Rourkela. Special thanks to Prof. Rajesh Balakrishnan, University of Michigan for his support and encouragement during my studies. I would also like to extend my heartfelt thanks to Dr. Kamal Jonnalagadda, University of Science Philadelphia for his support

during my manuscript writing. I would also like to thank Prof. Robert Langer, a distinguished Professor of Massachusetts Institute of Technology (MIT), for giving valuable suggestion in my plan of work. My warm and special thanks to Mr. Nadiya Bihari Nayak, Bibhu Kalyan Biswal, Prangya Ranjan Rout, Sailendra Mahanta and Akalabya Bissoyi for their constant support and help whenever I needed them. I would not forget to mention all the project trainee, B. Tech and M. Tech students for their continuous support from the beginning of my research. My special thanks to Miss Rachna Mund for helping me in writing this thesis. I would like to convey my heartiest thanks to my beloved parents, brothers and sisters for their support and love during my stay in Rourkela and finally my special thanks to my loving mother without whom I am nothing in this world.

Niladri Nath Panda

Abstract

The present research focuses on the development of a novel silk fibroin based 3D artificial nanofibrous structure for its usage as a scaffold in bone tissue engineering. Silk fibroin (SF) was extracted from eri and tasar silk cocoons by degumming method and a spinnable SF blend was developed by selection of an optimal binary solvent system i.e. chloroform and formic acid (60:40 w/v). Randomly oriented nanofibrous scaffolds were developed from SF blend by electrospinning. The morphological characteristics of the developed scaffolds were studied by SEM, TEM and AFM. The structural and thermal properties were investigated by XRD, FT-IR, TGA, DSC and TM-DSC. The scaffolds were also characterized for surface property (% water uptake and contact angle measurement) and mechanical property. In vitro cell culture study confirmed the excellent cell supportive property of the scaffold in terms of cell attachment, cell proliferation and cellular metabolic activity using hMSCs derived from umbilical cord blood. The scaffold possessed good osteogenic property as confirmed by ALP, biomineralization, osteocalcein and RUN X 2 expression. All these results suggest that the developed SF blend derived from eri and tasar can be used as a base polymeric scaffold material for tissue engineering application including bone tissue regeneration.

Surface property and osteogenic differentiation ability of the nanofibrous SF blend scaffold were further improved by the deposition of nanohydroxyapatite (nHAp) over the surface of the scaffold by surface precipitation method and thus, SF/nHAp composite scaffold was developed. Similar to SF blend scaffold, the composite scaffold was also characterized for surface, mechanical and biological property and the results were compared with that obtained with pure SF blend scaffold. It was demonstrated that the developed composite scaffold showed improved surface property and osteogenic differentiation ability as compared to SF blend as well as the widely used SF scaffold derived from Bombyx mori. Hence, it can be concluded that the developed SF/nHAp nanostructure is a promising scaffold in bone tissue engineering application.

Keywords: Bone tissue engineering, silk fibroin, hydroxyapatite, scaffold, polymer composite, eri silk, tasar silk, electrospinning

Table of Contents

List of Figures

List of Tables

List of Abbreviations

3D	3 Dimensional
3DP	3 Dimensional Printing
AFM	Atomic Force Microscope
ALP	Alkaline Phosphatase
BM	*Bombyx mori*
CAD	Computer Aided Designing
CBhMSCs	Cord Blood Derived Human Mesenchymal Stem Cells
Cp	Specific Heat at Constant Pressure
CPC	Calcium Phosphate Cements
CT	Computerized Tomography
De	Deborah Number Correlation
DMEM	Dulbecco's Modified Eagle Medium
EBM	Electron Beam Melting
ECM	Extracellular Matrix
FT-IR	Fourier Transform Infrared Spectroscopy
GAG	Glycosamino Glycan
HFIP	Hexafluro Isopropanol
HSC	Haematopoietic Stem Cells
MNCs	Mononuclear Cells
MRI	Magnetic Resonance Imaging
MSCs	Mesenchymal Stem Cells
MTT	[5-Dimethylthiazol-2-Yl]-2,5-Tetrazolium Bromide
nHAp	nanohydroxyapatite
OD	Optical Density
PBS	Phosphate Buffer Saline
PCL	Polycaprolactone
PEG	Polyethylene Glycol

PEO	Poly(ethylene oxide)
PLGA	Poly(Lactic-Co-Glycolic Acid)
PLLA	Poly L- Lactic Acid
PU	Polyurethane
RGD	Arginine, Glycine, Asparatic Acid
RH	Relative Humidity
RP	Rapid Prototyping
RUNX2	Runt Related Transcription Factor
SBF	Simulated Body Fluid
SEM	Scanning Electron Microscope
SF	Silk Fibroin
SFF	Solid Free Fabrication
SL	Steriolithography
SLS	Stereolithographic Sintering
TCP	Tricalcium Phosphate
TEM	Transmission Electron Microscopy
TGA	Thermogravimetric Analysis
THF	Tetrahydrofuran
TM-DSC	Temperature Modulated Differential Scanning Calorimetery
UCB	Umbilical Cord Blood
UTS	Ultimate Tensile Strength

CHAPTER 1

General Introduction

1.1 Background and significance of study

It is a well-known fact that millions of people are suffering from various tissue related diseases including bone tissue diseases and defects arising from trauma, injury, congenital and degenerative bone loss and pathologic conditions [1]. Currently, 1 million bone grafting procedures are performed only in U.S. every year with a growth of 13% per year. Loss of human lives is very alarming owing to the shortage of organ donors. Keeping this in view, bone tissue engineering has emerged as the most promising technique for repairing diseased and/or damaged bone tissues by developing biological substitutes that enable complete recovery of original state and tissue functions [2]. It has also been considered that the design and fabrication of a biologically active artificial extracellular matrix (ECM) is one of the most challenging tasks in bone tissue engineering. Scaffold must be biocompatible and have desired degradation rate, high mechanical strength, high porosity and the required resistance to foreign body reactions [3]. In addition, scaffold should also provide the required structural support to host bone cells and facilitate bone formation by stimulating cell adhesion, proliferation and finally regulate osteogenic differentiation of host cells [4]. In this context, material properties and appropriate fabrication technique are prerequisites for the development of 3D scaffold for bone tissue regeneration.

The component of natural bone matrix is the combination of organic and inorganic materials and a variety of proteins, the main type of which is collagen and apatite as biological minerals. To meet the above requirement, a lot of research interest has been generated in recent years to explore potential biopolymers and their composites that can be used as scaffold materials in bone tissue regeneration. Though a variety of biopolymers have already been used for scaffold development in bone tissue engineering, not a single candidate is so far available commercially that can meet all the desirable properties required for scaffold development. As the structural characteristics of scaffold can’t exactly mimic ECM, the mat of the scaffold didn’t recapitulate the microenvironment for proper proliferation, differentiation and neo tissue formulation. Recently, artificial ECM made from polymer nanofibers has been considered as the most important features for tissue regeneration. Besides the amplified available surface area, nanofibers resemble with body tissue mimicking ECM to a greater extent. In this context, electrospinning is reported to be a promising technique for various tissue engineering

applications. Hence, there is a strong and urgent need of a research program for the development of a novel scaffold material and the fabrication of a 3D nanofibrous structure using appropriate technology to mimic the unique hierarchical architecture of bone matrix.

1.2 Tissue engineering in regenerative medicine

Tissue engineering and regenerative medicine is an interdisciplinary field where new materials are added to heal and regenerate damaged body parts day by day. The study of structure-function relationship in both normal and pathological tissues has been coupled with the development of biologically active substitutes or engineered materials. Bone is a hard tissue and the present healing procedure through tissue engineering requires material properties complying with its specification. The National Science Foundation of U.S. has identified its significant importance and defined it as “Tissue Engineering is the application of principles and methods of engineering and the life sciences towards the fundamental understanding of structure/function relationships in normal and pathological mammalian tissues and the development of biological substitutes to restore maintain or improve functions" [5]. The final goal is to develop new therapies that are impossible to treat successfully with existing medical approaches.

Tissue formation and regeneration process occur in human body throughout life i.e. from embryogenesis to wound closure. This process consists of cellular migration, proliferation and extracellular matrix deposition [6]. Matrix deposition and its organization are very significant for new tissue development. Tissue formation is a two-step process: 1^{st} phase is often associated with migration of epithelial cells and ECM deposition while the later phase is associated with matrix remodeling and transformation of initial granulation tissue to connective tissue [7, 8]. The derived material for scaffold fabrication depends upon polymers that can be replicated in nanofibrillar network with modulated interaction with multiple biochemical-ECM derived signals. The guidance should facilitate restoration of structure and function of damaged or dysfunctional tissue through a provisional 3D matrix which control the cellular function with guidance to spatial and temporal complex multicellular processes for tissue formation and regeneration. The properties of material and design of scaffold should encounter rejection by our body (skin, blood, bone, etc.) [9].

Tissue construct preparation with merging of engineered biomaterial with stem cell technology opens a new era for wound healing. Certain properties such as: porosity, pore size distribution, mechanical strength and rate of degradation are required to be tailored based on the type of tissue required to be regenerated. Artificial 3D matrices called scaffolds provide the structural integrity similar to the natural extracellular matrix (ECM) in the body utilizing bioinert and tissue friendly material. Gradually, this idea is shifted from bioinert to bioactive while maintaining the same physical function, durability with enhanced surface biointegration. Emphasis has been given to provide various tissue specific function to construct while compromising certain physicochemical properties of the implant till it participate in tissue regeneration processes. This can be feasible through implantation of stem cells within scaffold.

In contrast, the regeneration of scarry tissue in lieu of functional tissue is of no use. Thus, the classic 'triad' of Tissue Engineering is based on the three basic tissue components: a scaffold on which cells are incorporated and signals provided to build and differentiate the tissue.

1.3 Tissue engineering scaffold as ECM

1.3.1 Scaffold and its properties

It is advantageous to design scaffold by taking guidance and inspiration from ECM. Thus, scaffold acts as a carrier of viable cells and function as a provisional ECM during regeneration [10], comply with practical handling of grafts and implants and thereby, synthesize the functional tissues. The role of various properties in defining its suitability for tissue regeneration has been given in Table 1.1.

1.3.2 Biomaterials for scaffold development

Metals, ceramics and polymers are generally used in tissue engineered constructs to replace the damaged body parts. Their use depends upon the type and location of tissue to be regenerated. Metals lack degradability while ceramics raise certain issues related to mechanical stability in addition to biodegradability.

Table 1.1: Properties of Scaffold

Property	Description
Porosity	Should have large volume fraction to facilitate nutrient diffusion and allows cell migration. It should not be large enough to provide sufficient binding site for cell adhesion.
Mechanical properties	Elastic modulus should match with the target tissue to avoid shear stress and fibrotic encapsulation formation while enduring tensile stress, compression and other forces at the site of implantation. It should be finely tuned for lineage specific differentiation [11].
Degradability	Degradation rate should be equal to rate of new tissue formation without toxic byproduct. Further, it should not be solubilized during tissue regeneration processes.
Surface chemistry	Either promotes or prevents protein adsorption and cell attachment.
Surface topography	Compelling for cell adhesion and tissue integration via mechanical and integrin mediated interlocking.
Biocompatibility	Material and its degraded products should be non-toxic, non-immunogenic and lack of geno-toxicity.
Bioactivity	Material should induce tissue synthesis (intrinsic property). Certain ligands such as RGD, YSIGR provide bioactive property to scaffold.
Specific tissue inducing properties	The scaffold should promote cell adhesion, proliferation and migration as well as differentiation of particular phenotypic tissue as desired e.g. osteoconductivity and osteoinductivity in case of bone [12].
Other properties	Structurally reinforce the defect, prevent ingress of surrounding tissue and act as a delivery vehicle for cells, GF and genes [13]. Further, controlled release of growth factors is essential for tissue development.

1.3.2.1 Polymers

Polymeric implants can be designed as hard or soft, rigid or elastic, inert or bioactive and degradable or non-degradable as per demand. The versatility of polymer finds a replacement for metals and ceramics [15]. Non-degradable polymers are required for electric cord in a pace maker, patches and intraocular lenses [16]. However, tissue engineering construct focuses on biodegradable polymer with non-toxic byproducts due to their replacement by body tissue. The degradation of material into non-toxic in vivo by-product is important for tissue regeneration [17]. Synthetic polymers such as poly(glycolic acid), poly(lactic acid), poly(ethylene glycol) and poly(vinyl alcohol) can be used for formation of functional biomimetic structure and extensively

explored for cellular compatibility. Knitted structures developed from these provide large specific surface area for cell adhesion and give enough space for cells to grow and develop an ECM environment.

Synthetic polymers

These are synthesized chemically so that it is possible to control the degradation rate and stiffness by varying its number of branching, polymerization and molecular weight. Additionally, they can withstand a range of processing techniques involving high temperature and pressure those are not possible in case of natural polymers. They can produce scaffold with complex architecture which is not possible for natural polymers. In contrast, cells do not recognize synthetic polymer surfaces. Cell integrin fails to bind the scaffold surface. Moreover, some synthetic polymers are non-degradable while others have cytotoxic degraded product.

Natural polymers

Natural biopolymers used for tissue engineering include collagen, polyhydroxy butyrate, chitosan, gelatin, fibronectin, hyaluronic acids and silk fibroin (SF). Collagen is found in body tissues such as teeth or bones, cartilage, skin, blood vessel and even muscles. The diversity of source affords different structure, function and molecular characteristics of extracted collagen. Since this is intimately related to the matrix components in all tissues, they are most promising polymer for regenerative and repair. Fibrin, a biodegradable protein takes part in provisional matrix formation after tissue damage that will be later replaced by cellular activity. This fibrous matrix is used for anchoring skin grafts. Curie et al. has found that presence of fibronectin enhance cell migration within the fibrin matrix [18]. Chitin, poly(β-(1-4)-N-acetyl-d-glucosamine), a natural biopolymer is synthesized by an enormous number of living organisms such as arthropods (exoskeleton) fungi and yeast (cell wall). Chitosan is the most important derivative of chitin obtained by (partial) deacetylation of chitin in the solid state under alkaline conditions (concentrated NaOH) or by enzymatic hydrolysis. Chitin and chitosan are biocompatible, biodegradable and non-toxic polymers. These properties make it application in tissue engineering, wound healing and drug delivery. Nevertheless, these biopolymers are endowed with poor mechanical properties and fail to meet the requirement for bone tissue

regeneration. The search for a new material with high tensile strength finally terminates with silk whose mechanical properties can with stand the desired strength and stiffness suitable for bone.

1.3.2.2 Bioceramics

Bioceramics such as β-Tri Calcium Phosphate, Octa Calcium Phosphate, Hydroxyapatite (HAp) are widely used in bone tissue engineering application. HAp is the major constituent of bone (nearly 75%) of dry weight and responsible for much stiffness and strength of scaffold. They are biocompatible, osteoinductive, bioactive and have unique capacity for bone binding with low degradation rate. The bioactive glass because of the presence of silicate (-O-Si-O-) network promotes the nucleation of natural HAp which is desired for bone tissue engineering. However, these materials are often associated with brittleness and thereby, limiting their applications.

1.3.2.3 Biopolymer and its composites

For high strength application, synthetic polymer, biopolymers and their composites with derivatives of calcium phosphate have been developed. However, most of the fabrication techniques involve synthetic polymer based application. Laurecin and his co-workers have developed composite PLGA/HAp via combination of emulsion freeze drying [29].

1.4 Scaffold fabrication techniques

A number of scaffold fabrication techniques have been evolved for the development of tissue engineering scaffold, a brief of these techniques are introduced here.

1.4.1 Salt leaching

Salt leaching is a simple, convenient and cost effective method to introduce porosity into tissue engineering scaffold [19]. These processes involve casting of a polymer-porogen solution followed by solvent evaporation and removal of porogen by solvent washing. Porogens for this method include sodium chloride, paraffin spheres, sugar crystals, gelatin and polymers. However, this method fails to produce controlled pore size (submicron and nanoscale), interconnectivity and irregular pore geometry. Ma et al. fabricated paraffin spheres of different sizes by changing the concentration of gelatin which is very effective to disperse paraffin liquids

to form spherical droplets. PLLA scaffold can be prepared through this method using paraffin spheres and PLLA/1,4-Dioxane solution [20].

1.4.2 Freeze drying

Freeze drying is used to produce porous open cell materials where the pore microstructure is controlled by a removable phase that is distributed in 3D space termed as removable template. The scaffold material is allowed to distribute around the removable template which is removed thereafter. The process includes an aqueous/organic solvent based solution of polymer which is solidified at atmospheric pressure to a specified final freezing temperature in a mold determining final geometry of scaffold. During solidification, the polymer content is localized between the growing ice crystals in aqueous phase. The process completion emerges with continuous interpenetrating network of ice crystals surrounded by polymer network. Application of very low pressure (P_{sub}) through a vacuum pump removes the ice phase with minimum effect on porous architecture of polymer network. The pore size and morphology are generally influenced by final freezing temperature (T_f) and heat transfer processes. The rate of nucleation (ice crystal formation) and diffusion are mediated by degree of undercooling required to initiate solidification [21].

1.4.3 Electrospinning

The architecture of the biomaterial is of great importance. Indeed, it must mimic the morphology of the tissues (i.e. the bone and the subchondral bone) to promote cell adhesion, growth, migration and differentiation. Successful tissue regeneration requires the development of a three-dimensional nanofibrous scaffold, which displays a large specific surface and a high porosity with appropriate pore size. Recently the very promising elaboration of nanoscaled (~50 nm) fibrous scaffold has emerged with the development of electrospinning techniques [22]. The developed non-woven mat has a very large specific surface area and a multiscale pore size distribution from nano to micrometers making them excellent candidates for biomaterial scaffolds improving cell interactions.

Electrospinning (first discovered in 1902 by Marley and Cooley) is the preparation of fiber from a polymer solution by applying an electrostatic field to a constant flow rate solution. It involves

pushing the solution through a syringe pump forming a Taylor cone on the tip. The electrostatic force generates a drawing force on the charged droplet to collect the produced fibers on the stationary grounded target [23]. In total 13 different parameters such as concentration of polymer, viscosity, surface tension, conductivity, volatility, applied voltage, tip-collector distance, flow rate, diameter of needle, temperature, humidity and air velocity of the chamber regulate the morphology of electrospun fibers. Besides these parameters, type of solvent system and nature of polymer decides the spinnability of polymer. Turning on the positive electrode from the voltage source attached to the metal tip of the syringe needle injects polar liquid jet. Increase in electric field strength creates repulsion in charged solution and the grounded plate creates tensile forces on the pendant drop to elongate generating fibers [24]. The random depositions of fibers on the ground target for several hours create a highly porous non-woven mat with standard deviation of fiber about 60-70%. Uneven jet stretching, possibly due to low polymer concentration creates fibers with beads. Continuous fiber formation happens if the jet does not undergo break up during elongation processes where elasticity of the solution act as restoring force. Elasticity is a function of molecular weight of polymer and solution viscosity while the other parameter surface tension is affected by the type of solvent and polymer concentration [25].

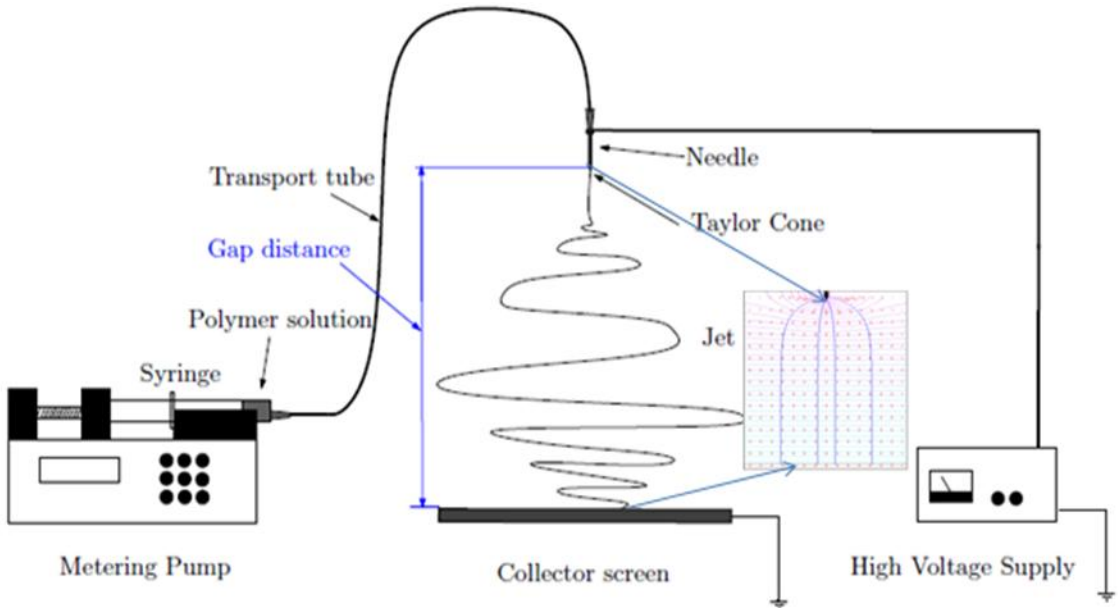

Figure 1.1: Schematic diagram of a typical electrospinning setup

Electrospinning is capable of producing micro/nanofibers from a list of synthetic and biopolymers too numerous to name. Biopolymers are of special interest in tissue engineering due to their complete removal after healing. The commonly used solvent include ethanol, methanol, HFIP, THF where choice depends on solubility, boiling point, and dielectric constant. Certain macromolecules fail to electrospun due to low molecular weight and high entanglement which require either a mixture of solvent or addition of co- polymer to produce nanofibers.

The terminal fiber diameter can be projected mathematically by a scaling law and Deborah number correlation (De) to predict the density of beads [26,27]. The terminal fiber diameter is the minimum achievable fiber diameter under a certain set of fluid and electric field conditions. Balancing the attractive and repulsive forces along the fiber backbone, the equation of the terminal fiber diameter will be $h_t = \left(\frac{Q}{I}\right)\frac{2}{3}\left(2\gamma\varepsilon/\pi(2ln\chi^{-3})\right)^{1/3}$. Flow rate current ratio is fundamental scaling for electrospinning processes. The second term, surface tension (γ), dielectric constant (ε) and a dimensionless whipping term (χ) play a minor role. The Deborah number gives an insight into relaxation time of a solution relative to processing time scale. For a solution to electrospun, the processing time equates the rate of whipping. Yu and company finds that no fibers (droplets only) are produced for De< 1 across all values of viscosity and surface tension force while De> 6 generates uniform fibers. De between 1-6 creates beads on string morphology.

1.4.4 Rapid prototyping

Rapid prototyping (RP), generally known as solid freeform fabrication (SFF) is a set of advanced manufacturing processes in which objects can be built by layer by layer deposition manner directly from computer data such as Computer Aided Design (CAD), Computed Tomography (CT) and Magnetic Resonance Imaging (MRI). The ability to incorporate advanced RP and CAD techniques to produce scaffold is now a mature application area of RP. The fabrication starts with a 3D design which is transferred into a STL (stereolithography) file format where thin virtual, horizontal cross sectional slices are transferred layer by layer. This technique is based on extrusion-based RP techniques, 3 Dimensional Printing (3DP), Selective Laser Sintering (SLS), Stereolithography (SL), Microstereolithograph (μSL) and Electron Beam Melting (EBM).

1.5 Stem cells for tissue engineering

Hematopoietic stem cells (HSCs) and mesenchymal stem cells (MSCs) [28,29] are endowed with multilineage differentiation potential and immunomodulatory properties. The HSCs possess immunomodulatory activity and promotes hematopoiesis. The major sources of MSCs include blood, bone marrow, adipose tissue, placenta, amniotic fluid, fetal tissue and umbilical cord blood (UCB). Among these, UCB is one of the potential sources for the isolation of MSCs and HSCs because of ample availability ease of handling and cheaper as being considered as hospital waste product. The failures to isolate and grow MSC from UCB in many cases raise questions regarding the presence of mesenchymal progenitors in full term UCB [30]. In fact the frequency of MSCs in UCB is very low and decline in fetal blood with gestational age from about $1/10^6$ to mononuclear cells in 1^{st} trimester of fetal blood to $0.3/10^6$ mononuclear cells in terms of cord blood [31]. Despite these limitations, isolation of CBhMSCs is possible through selection of critical parameters from processed cord blood units.

1.6 Thesis organization

The whole thesis work has been arranged in the following chapters. **Chapter 1** describes the general introduction including background and significance of scaffold materials and its properties, fabrication techniques and organization of the thesis. **Chapter 2** provides literature review on different varieties of Indian silk, a SF based scaffolds for bone tissue engineering, scaffold properties, and surface modification those have been performed till now. **Chapter 3** defines scope and objective of the study. **Chapter 4** describes the materials and detailed methodology adopted throughout the research work. **Chapter 5** describes results and discussion consisting of 3 parts that includes (i) preparation of SF blend solution (ii) development of electrospun nanofibrous SF blend scaffold (iii) development of SF/nHAp composite scaffold. **Chapter 6** provides summary and conclusion.

CHAPTER 2

Literature Review

Bone defects and diseases are increasingly becoming alarming worldwide due to the crisis of organ shortage. To overcome the shortage of donor and a long waiting list of patient with bone tissue defects, there is need for an effective and alternative therapeutic strategy. In this context, bone tissue has emerged as the alternative strategy to repair and replace bone tissue. Bone is considered as the 2nd most transplanted tissue in the world and there is great demand for treatment of bone tissue grafts [32], constructs and substitutes [33]. Bone tissue engineering requires a 3D scaffold that mimics the porous structure and excellent matrices functions of bone. Appropriate design and fabrication of this scaffold from a suitable material is a key challenge. Natural biopolymers and their composites through addition of ceramic materials are considered as the most attractive option for bone tissue regeneration [34, 35]. Polymer composites are combinations of two or more components usually containing an inorganic phase and a polymer phase that are essentially insoluble in each other [36]. Polymers have typically lower modulus and deformation resistance than the inorganic phase. Hence, attempts are made to adjust the mechanical properties of polymeric materials to approximate those of bone, using a composite structure. In fact, the matrix polymer containing filling components result in a complicated interaction between the properties of every constituent phase i.e. (a) the matrix (b) filling components and (c) the interfacial region between the filling components and the matrix polymer [37]. In the development of composites for bone tissue engineering scaffolds, two main approaches are being followed; the first approach considers the incorporation of bioceramic particles as inclusions into polymer structures e.g. foams, the second approach considers the incorporation of polymer coatings onto a 3D porous bioceramic [38].

In bone tissue, ECM consists of an organic phase made of type I and type III collagen and glycosaminoglycans (GAGs) and an inorganic phase made up of nanohydroxyapatite (nHAp). Calcium Phosphate (CaP) nanoparticles can be introduced into polymer-based scaffolds such as acid-soluble chitosan [39], alginate [40] and some soluble collagens. Alternatively, chemical deposition processes using calcium salts and phosphate or phosphoric acid can produce nano-featured CaP structures under controlled conditions. For example, flowing feed solution containing both calcium and phosphate ions has also been used to prepare collagen fibrils with CaP incorporated within the fibrils [41]. Studies have shown composite scaffolds of chitosan with HA and gelatin improves the biological responses of osteoblast cell type [42]. In another

study, authors found a decreased degradation rate and increased mineralization in SBF in composite scaffolds in the presence of nHAp [43].

CaP including HAp, tricalcium phosphate (TCP) and calcium phosphate cements (CPC) play an important role in the development of scaffolds for bone tissue engineering. Porous CaP ceramics with interconnected macropores (>200 μm) and microporosity (~5 μm) as well as high porosities (~ 80%) have been produced by firing polyurethane (PU) foams coated with calcium phosphate cement at 1200^0C [44]. The open micropores of the struts were infiltrated with poly(lactic-co-glycolic acid) (PLGA) to achieve an interpenetrating bioactive ceramic/biodegradable polymer composite structure. Miao et al. [45] have also developed highly porous HAp/TCP composite scaffolds (87% porosity) infiltrated with PLGA to form ceramic-polymer interpenetrating microstructures. In these composites the addition of PLGA led to a significant improvement of the compressive strength. In related investigations, HAp scaffolds have been coated with HAp particles and polycaprolactone (PCL) [46]. The PCL matrix acted also as carrier for the antibiotic drug tetracycline hydrochloride. Chen et al. [47] have developed Bioglass®-based scaffolds coated with PDLLA. It was found that the bioactivity of scaffolds upon immersion in simulated body fluid (SBF) was not impaired by the PDLLA coating. Polyhydroxyalkanoate (P(3HB) has been investigated in parallel investigations as an alternative coating material for tissue engineering scaffolds [48]. Bretcanu et al [49] used bacteria-derived P(3HB) to infiltrate 45S5 Bioglass® glass-ceramic scaffolds to enhance the work of fracture of the coated scaffold with respect to bare bioglass scaffold. Porous sponge scaffolds are suitable for bone tissue formation, as they enhance cell attachment, proliferation and migration. In addition, the high porosity (92-98%) facilitates nutrient and waste transport into and out of the scaffolds. It was found that the lamellar architecture of silk based scaffold induced increased alkaline phosphatase activity and demonstrated higher equilibrium modulus than the spherical-pore scaffolds [49].

With the advances of nanotechnology, material design can be exploited into the nanometer scale- and nano-structured biomaterials begin to emerge [50]. Among them nanofibrous biomaterials are exciting because of their similarity to ECM structure and functionality [51]. The collagen like fibrillar structure of the nanofibrous biomaterials along with their high surface to volume ratio enhance cell adhesion which in turn improves cell migration, proliferation and differentiated function on these biomaterials [52, 53]. Nanofibrous scaffolds have been shown to have better

cell attachment than solid walled scaffolds due to more cell adhesion proteins absorbance. Osteoblasts were cultured on both nanofibrous and solid-walled PLLA scaffolds and cells on nanofibrous scaffolds showed higher alkaline phosphatase (ALP) activity and an earlier and enhanced gene expression of the osteoblast phenotype [54].

Electrospinning generates connected 3D mats with high porosity and high surface area that can mimic ECM structure and are suitable for tissue engineering applications [24]. It also produces non-woven meshes containing fibers with diameters ranging from tens of microns to tens of nanometers. Fibrous scaffolds have a high surface-to-volume ratio that enhances cell adhesion. [51] Electrospinning is used to fabricate nanofibrous structures from natural and synthetic polymers such as collagen (Col), gelatin, chitosan, SF, poly(DL-lactide-co-glycolide), poly(lactide), polyurethane, polycaprolactone, etc. with a mean diameter down to 5 nm. PCL/HA, PCL/Col/HA, PCL/Gel/HA, poly-L-lactic acid (PLLA)/Col/HA and poly(3-hydroxy-butyrate-co-3-hydroxyvalerate (PHBV)/HA were fabricated by various research groups as a substitute for bone tissue engineering [55-59].

Tissue engineering approaches for bone repair with different morphology using SF have been reported. Initial effort starts with SF hydrogel [60] and membrane without cell seeding for guided bone tissue regeneration. Later on, in the last decade the regenerated SF was used as films [61]. SF based hydrogel has shown better in vivo bone growth than commercially available synthetic polymer [60]. In order to regenerate the complex defect at bone injury sites, several smaller scaffolds should be stalked instead of a large sized scaffold. Though large sized bones provide better mechanical strength, the mass transport limitation finds difficulty in its use [62]. Silk microparticles reinforced macroporous silk protein-protein composite scaffold was reported elsewhere [63]. Both the scaffold stiffness and bioactivities of composite scaffold was found to be enhanced on addition of silk microparticles to porous silk matrix. 3D porous scaffold with 90% porosity prepared from regenerated SF derived from *Bombyx mori* with average pore diameter 50 μm were suitable for tissue regeneration [64]. Further improvement of this SF scaffold prepared from salt leaching produced scaffold with porosity 84-98% and average pore diameter 200 μm [65]. Yan et al. has improvised the physicochemical properties of SF based scaffold by tailoring the 3D architecture through a combined salt leaching and freeze-drying method for its use in cartilage and meniscus tissue engineering [66]. Mandal et al. developed

micron-sized silk fibers (10-600 μm) through alkali hydrolysis for fabricating reinforced compact fiber composite with tunable compressive strength, surface roughness, and porosity for bone tissue regeneration [67]. The inter connectivity of the pore of the scaffold is also an important factor in aiding nutrient transport, promoting cellular migration, cellular bridging and in growth of bone tissue [68]. The continuity of fiber and its orientation control the transmission of shear stress along the fibers upon exertion of biomechanical forces [69]. The stiffness of the scaffold also depends on the porosity and architectural design of the scaffold which ultimately decides the cell specific lineage of MSCs. Williams et al. also reported that the PLC scaffold fabricated by selective laser sintering resulted in varied stiffness values with change in pore diameter [70]. Furthermore, the stiffness of the material is reported to be altered by change in scaffold architecture [71]. The stiffness of the material has an influence on the differentiation of MSCs to a particular cell lineage. The values of stiffness that differentiate into bone specific lineage have been reported to be 30-34 kPa [72]. Bailey et.al has demonstrated the importance of gradient scaffold in cell-material interactions i.e. in the regeneration of the interfacial tissues (e.g. osteochondral tissues) [73]. Furthermore, Discher et al. have reported 5 times more susceptibility of MSC population to neural lineage whereas the bone specific lineage is 8 times more under same culture condition which is far behind critical requirement for in vivo use where 100% cells with desired lineages are mandatory to avoid any abnormal tumor formation [72].

The most extensively researched silks all over the world are those derived from silkworm silk *B. mori* and spider silk *Nephila clavipes* [74]. Silk is considered as an advanced biomaterial owing to its biocompatible and biodegradable property. It has much superior mechanical properties than the traditional synthetic polymeric materials used for tissue engineering applications. Silk is a protein biopolymer obtained from insects, spiders and silk worm. It is a combination of light weight (1.3 gm/cc), high strength (4.8 GPa) with outstanding toughness and elasticity [75]. It is thermally stable up to 250^0C and hence can be processed for a wide range of temperature. Natural silk is composed of a filament core protein, SF and a glue-like coating consisting of a family of sericin proteins. The sericin is responsible for the inflammatory reaction in our body upon contact. SF from *B. mori* comprises of 12 repetitive crystalline regions and 11 non-repetitive interspaced amorphous regions. It constitutes 45.9% glycine, 30.3% alanine, 12.1% serine, 5.3% tyrosine, 1.8% valine and 4.7% other remaining amino acids. However, it is insoluble in most solvents, including water, dilute acid or dilute alkaline solutions. Its elastic

modulus is in the range of 15-17 Gpa and tensile strength 610-690 MPa [76]. Rockwood et al. have demonstrated the use of *B. mori* SF as hydrogels, tubes, sponges, composites, fibers, microspheres and thin films implants for scaffolding in tissue engineering in vitro disease models and drug delivery [77].

For the first time Vollrath et al. have used spider silk for artificial spinning to produce fibers [78]. Lazaris et.al have utilized soluble recombinant spider silk produced in mammalian cell for biomedical application [79]. For the first time Sen et al. have demonstrated the structure and compositional variation of amino acid in different types of SF based on its source [80]. Nevertheless, impure SF is often associated with Type I allergic response because of upregulation of Immunoglobulin E (IgE) levels and thus aggravating asthma. There are 5 different types of silk available in India that differs in their structure, property, composition and biological responses (Table 2.1).

Table 2.1: Types of silk and their sources

Sl no.	**Varieties of silk**	**Areas where found**
1	Mulberry	Karnataka, AP, Tamil Nadu, J&K, Maharashtra, Mizoram, West Bengal, Uttarakhand, Assam
2	Muga	West Bengal, Assam, Meghalaya
3	Eri	Nagaland, UP, Assam, Orissa
4	Tropical Tasar	Chhattisgarh, Orissa
5	Oak Tasar	Manipur, Uttarakhand

The production of *Vanya* silk in India (tasar, eri and muga) 2010-11 was reported to be 1166, 2760 and 124 MT while in 2009-10 was 803, 2460 and 105 MT. Thus an increase of 45.2% tasar, 12.2% eri and 18.1% muga silk has been achieved. The production of mulberry silk nearly remained constant at 16322 MT in 2009-10 and 16360 MT in 2010-11. The difference of eri and tasar from mulberry type of SF in structure and functional properties were studied and their application in tissue regeneration has been reviewed for fabrication of a novel material with improved tissue regenerative property. In this context, the potential of eri and tasar silk for tissue regeneration as compared to SF from *B. mori* has been compared. These three types of SF are different from each other in their immunocompatibility, presence of RGD epitope, anti-bacterial

and anti-inflammatory activity. Moreover, the regenerated SFs are highly heterogeneous in nature. The details of the structural heterogeneity is given in Table 2.2. Raghu et al. have shown that even 1% w/v of RSF shows structural heterogeneity. Therefore, their physicochemical and biological properties largely vary with respect to property modification and biological superiority [81].

Table 2.2: Different types of silk and their structural difference

Silk worm (species)	**Molecular weight (kDa)**	**Type/size of polypeptide**	**Amino acid**		
			Base/acid	**Hydrophobic /hydrophilic**	**Bulky/non-bulky**
Mulberry (B. mori)	440	Heterodimeric/H chain 390 L chain 26	0.65	0.28	0.17
Non mulberry (P. ricini)	400	Homodimeric/ H chain 230	1.30	0.35	0.24
Non mulberry (A. mylita)	395	Homodimeric/ H chain 197	0.97	0.44	0.34

Stevens et al. have shown that ECM of our body consists of collagen nanofibers with diameters in the range of 50-500 nm [82]. Electrospinning of SF obtained from wild source remains a challenge due to its high content of bulky group containing amino acids and large degree of heterogeneity among the side chains. Ramakrishna and co. in his book have highlighted the role of various factors and types of materials that can be electrospun into fibers [83]. Meanwhile, Chen et al. have developed aqueous microfibrous SF scaffold for the first time with 34% w/v of SF [84]. In contrast, this failed to meet the natural architecture of body. For example, an all aqueous process for silk electrospinning was developed [85] after blending regenerated SF with a fiber forming agent, poly(ethylene oxide) (PEO) from 1:4 to 2:3 ratios to improve electrospinnability of silk solutions and to avoid the adverse effects of using strongly polar organic solvents such as hexafluoroacetone [86], hexafluoroisopropanol [87] and formic acid [88] on biocompatibility. A post-electrospinning treatment on SF fibers with methanol was then performed to induce a structurally conformational transition to the original β-sheet to render water insolubility in subsequent uses of the scaffold. Acidic protein poly(L-aspartate)(poly-Asp)

as a molecular recognition motif was first introduced into the electrospun SF fibers to enable subsequent nucleation and crystal growth of apatite on the fiber surface during mineralization. This approach is an alternative route for preparing composite nanofibers to avoid the electrospinnability problem encountered in the electrospinning of those HAp containing solutions which eventually leads to the formation of apatite-coated fibroin composite fibers, which is somewhat different from that obtained in the components hybridizing method [89, 90] and the nanostructure of hierarchical bone [91-93] in terms of distribution and morphology of the HAp nanocrystals in the composite fibers. Li et al. have found superior bioactive and biocompatibility properties of 3D porous scaffold developed from *Antheraea pernyi* as compared to *B. mori* scaffold [94]. Pal et al. revealed the superior potential of eri SF as compared to *B. mori* for tissue regeneration and calcium deposition [95].

Chen et al.showed that surface modification of *B. mori* scaffold with RGD has improved the cell adhesion property of MSCs and osteoblasts [96]. Sukigara et al. produced continuous electrospun nanofibers from *B. mori* through optimization of concentration, voltage and tip-collector distance [97]. Zhu et al. have demonstrated that reduction of concentration and pH of SF would transform the belt shaped nanofiber to cylindrical shape [98]. Fang et al. have verified the superiority of *Antheraea pernyi* SF over the SF derived from *B. mori* in preparation of the scaffold. Meinel et al. have fabricated beadless aqueous SF fiber by decreasing humidity in air [99]. Additionally, there are several other wild sources of silk varieties with difference in structure, amino acid composition such as muga and the crosslinked types. In general, the difference in content of hydrophilic amino acid sequence and presence of repeating units like RGD determine the superiority of one variety over the other. Structurally, SFs from these species are characterized as natural block copolymers composed of hydrophobic blocks with highly preserved repetitive sequence consisting of short side-chain amino acids such as glycine and alanine. Moreover, it contains hydrophilic blocks with more complex sequences that consists of larger side-chain amino acids as well as charged amino acids [80]. The hydrophobic blocks from β-sheets or crystals through hydrogen bonding and hydrophobic interactions, provide tensile strength of SF fibers [100]. Thus, the elasticity and toughness of silk is a function of ordered hydrophobic blocks in combination with less ordered hydrophilic blocks of SF [78]. The concentrated SF aqueous solution is a non-Newtonian liquid crystalline state, where SFs are lubricated and

stabilized by water and form micelle-like structures through phase separation due to SF's intrinsic hydrophilic-hydrophobic block structure [74].

Natural silk fibers are insoluble in polar solvents such as water, ethanol, dilute acids and bases, unless highly concentrated sulfuric acid, formic acid, hexafluoro isopropanol (HFIP), calcium nitrate or LiBr solutions are used [101]. Sirisuwan et al. have shown that eri silk is insoluble in most of the salt solutions having higher molecular weight which poses difficulty in preparation of regenerated SF solution [102]. SF combined with CaP based materials such as HAp, β-TCP or wollastonite would be able to produce composite scaffolds. In contrast, they fail to mimic the collagen-apatite composite which is naturally found in bone due to the lack of cell binding ligand RGD in its polymeric backbone. Jin et al. and Min et al. have reported that non-woven SF nanofibrous mats/nets support attachment, spreading and proliferation of human bone marrow stromal cells, keratinocytes and fibroblasts in vitro [85,103]. Moreover, random non-woven nanofibrous mats having diameter 150-300 nm fabricated by electrospinning also promote cell attachment, spreading, proliferation and differentiation of MC3T3-E1 osteoblast-like cells [104,105]. The above mats also have the potential for guided regeneration of bones at non-weight bearing sites [106-108]. Kang et al. have improved bone tissue formation and mineralization through fibrin and hyaluronic acid surface coating which regulate the controlled release of BMP-2 [109]. These outcomes were in agreement with similar findings by Liu et.al. They have observed 14% and 25% improvement in bone tissue regeneration owing to surface coating of hyaluronic acid and BMP-2 over porous silicate glass [110]. Following this success, Li et al. recently developed silk-based composite nanofibers with the incorporation of HAp nanoparticles (approx. 5% w/v) and BMP-2 (3 μg/mg of silk fibroin) growth factor to realize enhanced bone formation outcomes from culturing human bone marrow-derived MSCs. They found that the inclusion of BMP-2 and HAp nanoparticles within electrospun SF fibers resulted in highest calcium deposition and upregulation of BMP-2 transcript levels, compared to other electrospun silk-based scaffolds including silk/PEO, silk/PEO extracted, silk/PEO/BMP-2 and silk/PEO/HA [89]. In another method, the inorganic apatite component was selectively grown on and associated with the electrospun fibrous SF matrix by subsequent mineralization after soaking in SBF [90]. Wei et al. have revealed the superiority of SF/nHAp nanocomposite prepared by direct mineralization in bone tissue engineering [94].

Thus the chemical composition (material properties) of the scaffold material and its structural characteristics are prime factors that can affect cellular behavior and ultimately determine the performance of a tissue engineered construct [111]. The ideal standard for the purpose of human tissue regeneration is deemed to be the biopolymer or composite polymers that are endowed with a set of essential characteristics such as suitable surface chemistry, biocompatibility, gas permeability, biodegradability, mechanical strength, immunogenicity, foreign body response and so on [112]. It is further evident that a single biomaterial does not possess all the desired properties and thus there is need for the development of a polymer blend and/or composite material in appropriate composition from a variety of biopolymers and other biomaterials [113]. Failure of macroporous features of scaffolds to mimic the dimension scale of ECM rules out the reorganized cell microenvironment for proper proliferation, differentiation and neo tissue formation [114]. In this context, artificial ECM made from polymeric nanofibers because of its resemblance to body tissues has been considered as the most favorable feature for tissue regeneration [115]. Furthermore, among the biomaterials used for producing nanofibers, natural SF protein seems to be an attractive option [116]. These SFs are derived from both wild and domestic silkworms and spiders [117]. SF contains repetitive amino acid sequence of poly(alanine) or poly(gly-ala) type arranged in antiparallel β-sheet structure [118]. SF derived from these silks has robust mechanical strength, provides adequate stability in vitro and in-vivo, biocompatibility (sericine free) comparable to collagen I, less immunogenic and can be electrospun into pure SF nanofibers or blended with other biomaterials [118]. However, major drawback of the widely used SF derived from *B. mori* is low hydrophilicity and lack of natural cell binding domain RGD leading to poor cell attachment [119]. However, tasar and eri silks are more hydrophilic and possess the natural cell binding ligand RGD enthralling their attention in biomedical application. SF can sustain high temperature before degradation as evident from their thermal analysis study. Moreover, several literatures have reported the same way of sterilization and so we have used this method. There is very negligible effect of sterilization on degradation of scaffold with the release of few particles. Therefore we have performed consecutively two ways of sterilization i.e. autoclave followed by ethanol washing [120].

CHAPTER 3

Scope and Objective

In recent years, bone tissue engineering has emerged as a new but most promising technique for bone tissue regeneration. The major challenge of bone tissue engineering is the development of a biomimetic 3D scaffold from an ideal biopolymer or its composites. Among the several factors, material properties and structural features of a scaffold are the most important. In search of potential biopolymers, SF obtained from silk cocoon is found to have potential in bone tissue engineering because of its robust mechanical strength, desired biological and surface chemistry favoring bone tissue engineering applications of SF scaffolds. Furthermore, electrospinning has been considered as one of the most appropriate technique for the fabrication of a 3D scaffold. Therefore, the present research focuses on the development of a novel biomaterial or its composite and its fabrication of a 3D scaffold for bone tissue regeneration by electrospinning.

The objectives of this thesis work are as follows:

i. To prepare electrospun nanofibrous silk fibroin scaffolds for bone tissue engineering.
ii. To improve the desired property of the scaffold by surface modification with a suitable bioactive molecule.
iii. To study physicochemical, mechanical and biological properties of the scaffolds.
iv. To investigate cell-scaffold interaction and osteogenic differentiation of hMSCs over SF scaffolds.

Scope of work:

It is evident that millions of people worldwide are facing acute problems of bone tissue diseases and defects arising out of accident, injury, degeneration and aging. The situation has increasingly become alarming due to shortage of donors. Though scaffold-based bone tissue engineering is a possible future clinical method to regenerate bone tissue, recovering disease or defect bone tissue functionality still faces many challenges. In this context, the main challenge is the design and fabrication of a 3D functional scaffold as artificial ECM from a suitable biopolymer or polymer composites by an appropriate method. Therefore, the main objective of this present work is the preparation of a novel silk based scaffold by electrospinning method.

Various scope of the research work is enumerated as follows:

i. Development of a spinnable SF blend solution

SFs derived from *B. mori* have been used as a potential biopolymer for the development of scaffold. However, they have lower hydrophilicity that limits their usage as cell supportive artificial ECM. In this project, efforts are given to explore the other silk varieties grown in India such as eri and tasar that have superior scaffold properties than *B. mori*. SF will be extracted from both the silks and a spinnable polymer solution will be developed by selecting a suitable solvent system.

ii. Development of electrospun SF blend nanofibrous scaffold

Among the types of scaffold, 3D nanostructured scaffold is the most essential feature regulating the vital cellular functions such as adhesion, proliferation and differentiation. In this context, electrospinning, a simple and straightforward method, will be used to fabricate electrospun nanofibrous scaffold from the spinnable eri-tasar SF blend.

iii. Characterization of scaffold

It is utmost important to appraise surface, mechanical and biological properties of the scaffold to find its suitability in bone tissue engineering. Properties of the scaffold such as morphology, roughness, hydrophilicity, porosity, tensile strength will be characterized. Cell supportive property in terms of cell adhesion, cell proliferation and cell differentiation potential will be evaluated.

iv. Mechanism of biodegradation of scaffold

It is essential to control the biodegradation of scaffold in order to match the rate of neo tissue regeneration. The structural and morphological changes upon biodegradation will be determined from FT-IR, XRD, TM-DSC, SEM and AFM analysis and finally, the mechanism will be elucidated.

v. Improvement of osteogenic property of SF blend scaffold

To make the developed nanofibrous SF blend scaffold more effective towards bone tissue formation there is need to further improve its osteogenic property. In this context, the deposition of nHAp may be beneficial. Therefore, direct mineralization method will be applied to precipitate nHAp over scaffold. Thus a novel SF/nHAp scaffold with improved osteogenic property will be developed to facilitate bone tissue regeneration.

CHAPTER 4

Materials and Methods

4.1 Materials

4.1.1 Collection and processing of silk cocoons

Eri (*Phylisomia ricini*) and *B. mori* silk cocoons were collected from the local market of Mayurbhanj district and tasar (*Antheraea mylitta*) from Sundargarh district of Orissa, India. The collected eri and tasar silk cocoons were grounded into fine size and stored at -20^{0}C in a sealed plastic bottle until further use.

4.1.2 Chemicals and media

Necessary chemicals such as calcium chloride ($CaCl_2$) and sodium hydrogen phosphate (Na_2HPO_4) for the extraction of SF were obtained from Merck. Dulbecco's modified eagle medium (DMEM), Penicillin-Streptomycin solution, fetal bovine serum (Hi-FBS), Dulbecco's phosphate buffered saline (DPBS), chondrogenic basal medium and supplement, Collagenase type I and 0.25% Trypsin/EDTA solutions were obtained from Gibco (BRL, USA). Phalloidin-Alexa Fluor 488 conjugate and calcein green AM were purchased from Invitrogen, USA. Ficoll Hypaque solution (Hi sep LSM 1073), osteogenic differentiation media, Giemsa 10x stain, Triton X-100, formaldehyde, MTT assay reagent, Commassie blue G-250 are from HiMedia labs, India. Growth factors EGF and bFGF, BD FACS lysis buffer, Propidium Iodide (PI), CD34-PE, CD29, CD44-FITC, CD45-PerCP/cy5.5, CD73-PE/APC, CD90-APC, CD105-PE and HLA-DR-PerCP/cy5.5 were purchased from Becton Dickenson, San Jose, CA. Dexamethasone, staurosporine, α-MEM, L-glutamine, L-ascorbate, β-glycerophosphate, protease XIV, bovine serum albumin (BSA), Oil red O, Alizarin red S, Safranin O, tris buffer were from Sigma-Aldrich (St Louis, MO, USA). All the tissue culture plastic wares and RNAse were from BD falcon and MP Biomedicals, USA respectively.

4.2 Methods

4.2.1 Preparation of regenerated SF powder

The chopped slices of cocoon were boiled in 0.02 M aq. sodium carbonate (Na_2CO_3) solution for 30 min to remove sericin. This process is called degumming [121] and was repeated three times for tasar because of its higher sericin content. Extracted silk fibers were air dried and then dissolved in a ternary mixture of $CaCl_2/H_2O$/EtOH (1/8/2 mole ratio) for 40 min at 80^{0}C. The

solution was dialyzed in a slide-A-Lyzer dialysis cassette (Pierce, Thermo fischer, MWCO 3500) against distilled water for 3 days at room temperature to remove salts. The SF solution thus obtained was filtered and concentrated against PEG 6000 MW and PEG 10,000 MW. The concentrated SF solution was frozen for 24 h in -20^{0}C and lyophilized to obtain regenerated silk fibroin (RSF) powder. The prepared RSF powder was stored in vacuum desiccators until further use.

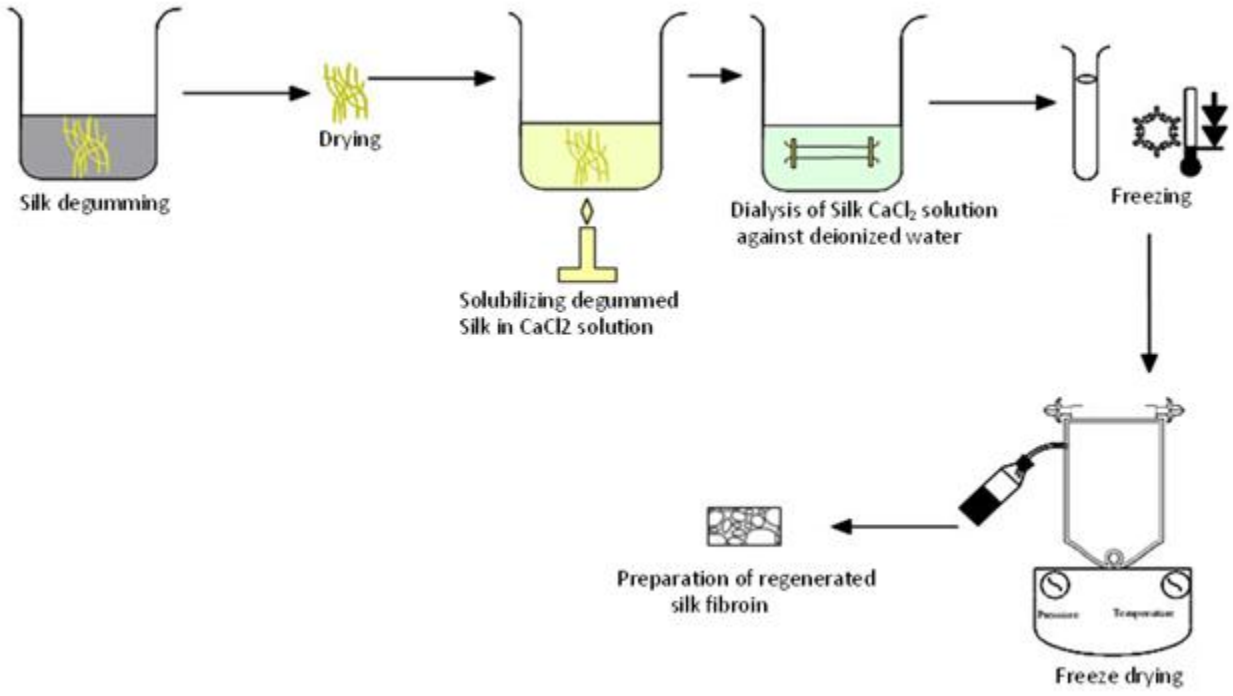

Figure 4.1: Schematic diagram of the preparation of regenerated silk fibroin powder

4.2.2 Preparation of eri-tasar SF blend

Different batches of SF blends were prepared by dissolving the freeze dried SF powder of eri and tasar in a mixture of formic acid and chloroform (60:40 v/v) at room temperature while constantly stirring until a clear solution is formed.

4.2.3 Preparation of SF blend nanofibrous scaffold by electrospinning

3D nanofibrous mat from SF blend was prepared in electrospinning machine (PICO-ESPINO-NANO, India) that consists of a 5 ml syringe with 0.55 mm needle diameter mounted on parallel plate geometry. The configuration of electrospinning machine is depicted in figure 1.1. Fiber was

formed at an applied electrostatic potential of 22 KV with a constant SF blend solution flow rate of 0.5 ml/h. Tip-collector distance was maintained at 15 cm. The fibers were collected on a grounded parallel plate collector consisting of aluminum sheet mounted over a glass plate.

4.2.4 Preparation of gelatin nanofibrous scaffold by electrospinning

Gelatin nanofibers were prepared by electrospinning following the previous literature [122]. In brief, 10% gelatin solution was prepared in formic acid while continuously stirring at room temperature for 1 h. The solution was filtered to remove insoluble fraction or impurities and then placed in a syringe (5 ml) with stainless steel syringe needle as an electrode. The syringe was connected to a syringe pump to control flow rate accurately. Electrospinning was performed at room temperature and at relative humidity about 65%. The applied electric potential was adjusted at about 20-21 kV and the distance to collector was between 12-15 cm for proper electrospinning. The produced non-woven mat of gelatin nanofibers was formed after few hours of running. Finally, it was dried overnight at 40^0C in an oven to remove moisture before measurements.

4.2.5 Preparation of SF nanofibrous scaffold from *B. mori* by electrospinning

Electrospinning of SF derived from *B. mori* was carried out with a slight modification in electrospinning procedure followed by Sukigara and Co [104]. RSF obtained by lyophilization was used for preparation of 12% w/v solution in formic acid (98-100%). The silk-formic acid solution was placed in a 3 ml syringe (18 gauze). The tip-to-collection plate (covered with aluminum foil) distance was maintained between 12-13 cm; the plate placed vertically under the needle tip with flow rate of 1 ml/hr at room temperature in 65% relative humidity. The above process was carried out for 10-12 h to collect a thin mat of SF nanofibrous mat.

4.2.6 Development of SF/HAp nanofibrous scaffold

HAp was deposited on SF blend electrospun nanofibers by precipitation following the procedure described in literature [94] to prepare SF/nHAp nanocomposite scaffold. The nanofibrous scaffold was immersed in 0.5 M of $CaCl_2$ solution in tris buffer for 12 h at pH 10.4. The scaffold was repeatedly washed with distilled water. Scaffolds were then immersed in 0.5 M of aq. Na_2HPO_4 solution in tris buffer for 12 h at pH 10.4 followed by washing with distilled water.

The alternate soaking and rinsing process were repeated for 3/5 cycles resulting in the precipitation of HAp over the nanofibers. The prepared HAp coated SF scaffold (SF/nHAp) was stored in a dessicator for further use.

4.3 Characterization of scaffold

4.3.1 Morphological characterization

Scanning electron microscope (SEM)

SEM (JEM2010, JEOL) was used to observe the morphology and fiber size of the electrospun nanofibrous scaffold. The nanofibrous scaffold were cut into small pieces and coated with 10 nm of platinum using a polaron range sputter coater before imaging. I individual fiber diameter was measured in the inbuilt imaging system and software attached to the instrument. The average diameter of fiber was determined by measuring 50 fibers selected randomly from each sample.

Atomic force microscope (AFM)

Topography or roughness of nanofiber scaffold surface was studied using a scanning probe microscope (VECCO) operated in AFM tapping mode at microscopic level (100-1 μm). In this technique, the probe tip made up of quartz is attached to a flexible micro-fabricated 225 μm long silicon cantilever with a spring constant of 3 N/m, the deflection of which is measured by optical method. The reflected light beam is focused to a particular position by moving the surface of the sample up and down and thus a constant force is maintained between the surfaces that produces topographical images.

Transmission electron microscope (TEM)

TEM images were obtained with a JEOL transmission electron microscope where the electrospun nanofibers were deposited on carbon-coated copper grids. The accelerated voltage was adjusted and the detailed shape and size of the nanofibers were examined. The study was carried out to find the shape of nanofibers, structural features of HAp crystals deposited over the nanofibers and the development of cell processes to confirm cell scaffold attachment.

4.3.2 Porosity and pore size distribution

The distribution of pore diameter, total pore volume, and porosity of the electrospun nanofibrous silk fibroin mat (approx. 0.8 mm thickness and 1x2 mm^2) were measured using a mercury intrusion porosimeter (Autopore IV porosimeter, Micromeritics Instrument Co., Norcross,GA) in mercury intrusion under an increasing pressure from 0.5-2000 psi. Prior to mercury intrusion, the instrument was degassed to approximately 30 μm of Hg to remove all air from the system.

Determination of porosity was based on the relationship between the applied pressure and the pore diameter into which mercury intrudes, according to the Washburn equation as

$$P = - 2\gamma\cos\theta/r$$

where P is the applied pressure, r is pore radius, γ is the surface tension of mercury (484 mN/m) and θ is the contact angle between mercury and the pore wall taken as 143^0 [123, 124].

4.3.3 Structural analysis by XRD and FT-IR

X-ray diffraction (XRD)

XRD curves were recorded in X-ray diffractometer (Rigaku D-Max B) with an X'celerator counter at scanning rate of 0.040^0/s with step size of 0.020^0 within a scanning region of $2\theta = 10\text{-}80^0$ and CuKα radiation (λ= 0.1542 Å). The irradiation conditions were 30 kV and 30 mA. XRD patterns were analyzed in X'pert high score, Origin Pro 8 and JCPDS (joint committee on powder diffraction studies) softwares. Crystallinity of SF nanofibers and the variation in percentage of β-crystalline content due to enzymatic degradation were determined from this study.

Fourier transform infrared spectroscopy (FT-IR)

FT-IR (Automatic IR Microscope, AIM-800, SHIMADZU) was carried out to identify organic and inorganic compounds by determining the molecular composition and functional groups in SF blend. In FT-IR, scanning range, resolution and scan numbers were 4000-400 cm^{-1}, 8 cm^{-1} and 60 respectively. Approximately 1 mg of nanofibrous silk blend scaffold mixed with about 500 mg of dry KBr powder was grounded using an agate mortar and pestle. The mixed powder was pressed into transparent disks with a diameter of 13 mm for the FT-IR work.

4.3.4 Thermal analysis by DSC, TGA and TM-DSC

Differential scanning calorimetry (DSC)

DSC determined the variation in glass transition temperature of enzymatically degraded SF scaffolds. DSC measurements were performed on a Mettler-Toledo 821 with intra cooler using STAR software. Temperature calibration and determination of the time constant of the instrument were performed by standards of In and Zn, and the heat flow calibration by In. Heating rate of 2^0C min^{-1} was applied to scan the sample using standard aluminium pan and nitrogen gas was used to remove the volatiles from the samples.

Thermogravimetric analysis (TGA)

Thermal stability of samples was analyzed with TGA (Mettler-Toledo 821). Scaffolds were scanned from 30-400^{0}C with a scanning rate 2^0C/min to check thermal stability. Mass loss of the samples was determined with respect to increase in temperature to assess the thermal degradation behavior of the sample.

Temperature modulated differential scanning calorimetry (TM-DSC)

TM-DSC measurements were performed using Perkin Elmer DSC instruments, Pyris Diamond DSC system. The instrument was equipped with a refrigerated cooling system. The samples were heated at 2 K/min with a modulation period of 60 s and temperature amplitude of 0.5 K. This analysis was performed to separate glass transitions from relaxation or re-crystallization effects, melting processes, fast chemical reactions and for accurate determination of isothermal Cp. The above study was carried out to determine the mechanism of biodegradation of SF nanofibers. The equipment was equipped with software allowing the superimposition of a sinusoidal temperature fluctuation onto an underlying heating or cooling rate [125].

4.3.5 Mechanical strength

Ultimate tensile strength of the nanofibrous silk scaffolds were tested in Universal Testing Machine (Instron 3369, Bioplus) with a 1000 Newton load cell under standard atmospheric conditions at 65% relative humidity. Scaffold samples were cut into rectangular shapes (50x12 mm) having thickness 0.30±0.01mm. The double sided glue tapes were used to stick the

scaffolds to the top and bottom clamps for positioning. The crosshead speed was 20 mm/min and the gauge length was 30 mm. The breaking strength and strain percentage of scaffolds were calculated from the stress strain plot.

4.3.6 Swelling behavior

The swelling studies of the nanofibrous scaffolds were performed in PBS and distilled water at pH 7.4 and 37^0C. The dry weight of the scaffold was noted (w_D). Scaffolds were then placed in PBS buffer at pH 7.4 for 1, 2, 3, 4, 5, 6, 7, 8, 24, 48 and 96 h. After this time period, scaffolds were removed, surface adsorbed water was removed by filter paper and the wet weight was recorded (w_T). The swelling ratio and water uptake % were determined using equations 1 and 2 [126].

$$swelling\ ratio = \frac{wT - wD}{wD} \qquad (1)$$

$$water\ uptake\% = \frac{w_T - w_D}{w_T} \times 100 \qquad (2)$$

4.3.7 Contact angle measurement

Wetting properties of the nanofibrous scaffolds were studied by dynamic contact angle measurements. Samples were fixed and a droplet of distilled water was applied to the surface. Water contact angles of the nanofibrous mat were measured by a contact angle goniometer (DSA-10, Kruss188, Germany). Images of each drop on the surfaces were recorded using a digital microscope. The contact angles were determined from the images using axisymetric drop shape analysis (ADSA-NA) methodology [127]. Mean values of the contact angles were calculated from five individual measurements taken at different locations on the substrates at 25^0C and 65% humidity.

4.3.8 Bioactivity

The SF nanofibrous scaffolds were immersed in 35 ml of SBF for 14 days at 37^0C. SBF was prepared according to the literature [128] by adding NaCl (7.995 g), KCl (0.224 g), $CaCl_2.2H_2O$ (0.368 g), $MgCl_2.6H_2O$ (0.305 g), K_2HPO_4 (0.174 g), $NaHCO_3$ (0.349 g) and $Na_2SO_4.10H_2O$ (0.161 g) to 1 L of distilled water in that order. The pH of the solution was then adjusted to 7.4 by adding Tris/HCl. After soaking for a predetermined time period, these scaffolds were taken

out, rinsed with distilled water and blotted with tissue paper to remove excess moisture and then vacuum dried at 45^0C for few hours. Morphological and elemental studies of the scaffolds were done by SEM and EDX respectively.

4.3.9 Biodegradation

SF has been reported to be degraded by several protease enzymes including protease XIV [129]. 6×6×0.03 cm^3 ethanol/propanol treated nanofibrous mats weighing 45±5 mg were incubated at 37^0C in 50 ml of PBS solution containing 0.23 U/ml protease XIV at pH 7.4. The nanofibrous mats without enzyme in PBS solution were treated as control. The retrieved samples were washed in distilled water after 0, 18 and 36 h, lyophilized and residual weight was measured. Morphological structure of the degraded SF nanofiber was observed using SEM. XRD, DSC and TM-DSC analysis of mat and their degraded products helped determine the mechanism.

4.4 In vitro cell culture study

4.4.1 Sources of MSCs

MSCs isolated from umbilical cord blood (UCB), cultured in our stem cell culture laboratory were used for cell study. In brief, UCB was collected from the local Ispat General Hospital, Rourkela, India and mononuclear cells (MNCs) were isolated from UCB following Ficoll Hypaque method described in the literature [130]. The isolated MNCs were cultured in DMEM supplemented with 10% fetal calf serum, 1% non-essential amino acid, 1% 200 mM L-glutamine, 2% 1 M HEPES, 0.150 g/liter L-ascorbic acid, 100 U/ml penicillin and 0.1 mg/ml streptomycin. Culture condition was maintained at 37^0C, 5% CO_2 and 80% relative humidity. MSCs were separated based on their adherence to the culture flask and non-adherent cells were discarded. The adherent cells were washed thoroughly with D-PBS/EDTA and then supplemented with freshly prepared expansion medium. The cells were cultured in media changed weekly twice until the 4^{th} passaging.

4.4.2 Culture of MSCs

MSCs were sorted from the cultured MNCs by a florescence activated cell sorting (FACS ARIA III; BD Biosciences) using CD90-APC, CD73-APC, CD105-APC, CD44-FITC, CD45 PerCP Cy5-5, HLA-DR PerCP Cy5-5, CD34 PE (all are BD Pharmingen, San Jose, CA make). CD44,

CD90, CD73 and CD105 were used as positive markers. The sorted MSCs were further cultured in DMEM media changed twice in a week.

4.4.3 Cell seeding and culture

Non-woven nanofibrous SF mats of radius 0.6 cm^2 were steam sterilized followed by ethanol washing [120] and then subjected to sterile PBS for ethanol removal. MSCs of passage four at the concentration of 5×10^4 cells/cm^2 were seeded into nanofibrous mats by static method. Cell seeded scaffold was incubated at 37^0C in 5% CO_2 and cultured in 2 ml of cell culture medium without growth factor following the procedure previously described [131]. The culture medium was replaced at regular intervals of 3 days. Cell suspension containing 5×10^5 cells/ml in medium without scaffold was used as control (n=2).

4.4.4 Cell morphology and cell attachment

The cultured MSCs seeded on the scaffolds were fixed with 3.7% formaldehyde (Sigma) for 20 min. The samples were diluted in blocking buffer at room temperature and permeabilized for 10 min with 0.5% Triton X-100/PBS. Cells were incubated in DPBS solution after permeabilization. Samples were blocked for 30 min with non-specific binding of antibody and the immunocomplexes were detected by ALEXA 488 conjugated phalloidin (1:200). The nuclei were stained with 0.1 μg/ml of DAPI in PBS for 1 min. Then the cell-scaffold constructs were visualized under confocal laser scanning microscope to assess cell attachment. Morphology and spreading of MSCs over the scaffolds were analyzed by SEM within the first 72 h of cell seeding.

4.4.5 Cell viability

Fluorescent Microscopy

SF nanofibrous mat of $0.5\times0.5\times0.03$ cm^3 were punched through a biopsy punch (Miltex) and sterilized by autoclave. The samples were then seeded with cells and cultured for desired period in a 96 well plate. They were then taken on a clean microscopic slide, mounted with glycerol:PBS (1:1 ratio) and observed under an upright fluorescence microscope (Carl Zeiss E_{600}, wavelength 450 nm) using a green filter (wavelength 490 nm). These constructs were observed

for visualizing the interaction between cell and scaffold, subsequently the images were captured using Carl Zeiss Axiocam camera attached to the microscope.

MTT assay

Cellular metabolic activity of MSCs seeded on scaffolds were evaluated by 3, 4, 4, HEPES [5-dimethylthi¬azol-2-y1]-2,5-diphenyl tetrazolium bromide (MTT) (Sigma, St. Louis, Mo.) staining. After 3, 5 and 7 days of culture, the cell seeded mats were incubated in MTT solution (0.5 mg/ml, 37^0C, 5% CO_2) for 2 h following the protocol in the published literature [132]. Intense pink colored formazan derivatives formed were dissolved and the absorbance was measured at 595 nm using spectrophotometric microplate reader (Perkin Elmer Model 2030 Explorer).

4.4.6 Cell proliferation

SEM

Qualitative determination of cellular proliferation was observed under SEM after 7 and 14 days of culture using the procedure described below. Prior to SEM analysis, cell-seeded scaffolds were rinsed in DPBS buffer and fixed with 2.5% glutaraldehyde in DPBS overnight at 4^0C. The constructs were dehydrated by exposure to a gradient series of alcohol (50-90% gradient of alcohol in water followed by aseptic critical point drying and coated with platinum before observing under JEOL JSM-840A SEM.

DNA content measurement

Proliferation of cord blood-derived MSCs on SF blend scaffold was determined by DNA quantification using spectrophotometric microplate reader (Model Perkin Elmer 2030 explorer) [133]. For this purpose, scaffolds (6 beads/well) were placed in triplicates in 6-well tissue culture plate containing MSCs suspended (2×10^5 cell/mL) in DMEM. The plates were incubated for 3 and 5 days in a CO_2 incubator at 37^0C and 5% CO_2. Total cellular DNA from cell-scaffold construct was isolated using alkaline lysis method. DNA content extracted was measured by spectrophotometric microplate reader at an absorbance of 260 nm for both the samples. To visualize MSCs on scaffold, the cells were seeded at 5×10^4 cells/disk (5 mm diameter) density and cultured in DMEM with 10% FBS at 37^0C for 3 days. The unattached cells were washed

away in PBS and the attached cells were fixed in 4% formaldehyde in PBS. Cells were treated with 0.2% Triton-X 100 (Sigma T9284) in PBS and blocked in 2% denatured BSA and were analyzed under inverted microscope.

Alamar blue assay

Proliferation of MSCs on the scaffolds was assessed for 7, 14, 21 and 28 days of culture using Alamar blue assay [14, 15]. This assay is based on the color change of fluorescence via oxidation-reduction reaction taken place in growth medium. After incubation, the scaffolds were placed in fresh wells in phenol red-free serum-free medium and then Alamar Blue was added followed by overnight incubation. After pipetting the media, OD was measured in a microplate reader at 570 nm.

4.4.7 Cell adhesion

4.4.7.1 Cell attachment

The nanofibrous scaffolds were seeded with 2×10^5 cells. Cell attachment was observed through phylloidin cytoskeleton staining counterstained with DAPI. This was further quantified by determining the average number of attached cells from 10 randomly chosen microscopic fields of observation at indicated time points. Data was plotted in graphs and compared with other scaffolds.

4.4.7.2 Cytoskeleton analysis

After an hour of culturing, MSCs seeded constructs (n=2 each) were rinsed in 1× PBS and prefixed in 0.5% glutaraldehyde in 0.1 M sodium cacodylate buffer [134]. The samples were added to the cell suspension in 1:1 ratio (n=2) and centrifuged. Pelleted cells were resuspended in 0.1 M sodium cacodylate buffer and added to 2% melted agar. The samples were then cooled and centrifuged at 300 g for 10 min. All samples were then rinsed in 0.1 M sodium phosphate buffer containing 1% OsO_4 and dehydrated in gradient ethanol (10-50%) followed by the addition of 100% acetone. Samples were molded in a mixture of Spurr resin and acetone, and then polymerized at room temperature until complete hardening. Ultrathin sections of 100 nm size were cut with a diamond knife and stained with methanolic uranyl acetate followed by lead citrate. Thin sections were examined in a JEM-1200 EX II transmission electron microscope

(JEOL, MA, USA) at 6.0-7.5k magnification for entire cells and cell processes were visualized at 30-33k magnification.

4.4.7.3 CD44 and integrin beta 1

Immunofluorescence measurement

The cell-seeded scaffolds were cultured for 12 h and then fixed in 10% ice-cooled paraformaldehyde. The sections were blocked in 2% BSA before incubating with mouse anti-CD44 (mouse1gG anti-rat 1:200), or mouse anti-CD29 (mouse1gG anti-rat 1:200) monoclonal primary antibodies. After incubation with primary antibodies, the sections were washed and exposed to Alexa-Fluon 488 and phycoerythrin conjugated secondary antibodies for CD44 and CD29 respectively. Fluorescent images were obtained using laser scanning confocal microscope (Leica, microsystem). DNA was visualized with Hoechst 33342 [134].

Flow cytometry analysis

The cell adhesion property of the developed scaffolds were further quantified by analyzing the expression of CD44 and CD29 surface markers using flow cytometer (Fortessa, BD Bioscience, USA) by following the procedure described [135]. Cell-seeded constructs were trypsinized and washed in PBS after 12 h of culture. The detached cell concentration was adjusted to 1×10^6 cells/ml by the addition of ice cooled PBS. Then CD44 and CD29 surface markers conjugated with FITC and PE were added to the cell suspension and analyzed for CD expressions in flow cytometry.

4.4.8 Osteogenic differentiation potential

4.4.8.1 Alkaline phosphatase assay

ALP activities of MSCs in constructs were measured to appraise the osteogenic differentiation potential as per the procedure described [136]. The constructs were cultured for 1, 7, 14 and 21 days in osteogenic differentiation media. Then they were removed from the culture media and repeatedly washed in PBS. The cells were treated with 1% Triton X-100 (Fisher Scientific) for 60 min and centrifuged at 10,000 rpm at 4^0C for 15 min. 0.5 ml of supernatant was added to dilute p-nitro phenyl phosphate (100 µl of p-NPP concentrate per 2 ml of 100 mM sodium

bicarbonate/carbonate buffer, pH 10) and incubated at 37^0C for 45 min. Reaction was stopped by adding 50 µl of 1 N NaOH and the absorbance of the mixture was measured at 405 nm.

4.4.8.2 Glycosaminoglycan (GAG) estimation

MSCs seeded scaffolds were grown in 96 well plates in osteogenic differentiation media for 3, 7, 14 and 21 days with media changed every 2-3 days. The amount of extracellular GAG secreted into the media was analyzed using 1,9-dimethylmethylene blue in a microplate reader [137]. Similarly, intracellular GAG was removed from the cells by digestion with papain digestion solution (125 µg/mL of papain, 5 mM L-cystein, 100 mM Na_2HPO_4, 5 mM EDTA) at pH 6.8, 60^0C for 16 h and analyzed in microplate reader. Finally, the absorbance of GAG-DMMB complexes was measured at 525 nm. In order to avoid the variation in scaffold size and cell numbers, GAG contents were normalized against total scaffold weight and cell numbers.

4.4.8.3 Biomineralization

Biomineralization study was performed following the protocol in the literature [128]. The hMSC-seeded scaffolds were washed in PBS, fixed with glutaraldehyde dehydrated by ethanol gradient (a series of ethanol water mixture (10-50% ethanol), sputter coated with platinum and attached to the sample holder through a conductive carbon tape. Energy dispersive X-ray analysis was performed to detect the presence of Ca and P, their quantity and ratio in the analyzed sample. Cells were grown over the nanofibers deposited over carbon grid and analyzed by high resolution TEM after dehydration through a series of gradient ethanol. The samples were put into the chamber for observing the formation of HAp crystals over the nanofibers.

Alizarin red assay

Mineralization of hMSCs on the nanofibrous scaffolds was observed and quantified using alizarin red assay [138]. MSCs grown on scaffolds were washed in PBS and fixed with paraformaldehyde for 15 min. Cell-seeded scaffolds were thoroughly washed in distilled water and 500 mL of 40 mM alizarin red stain (pH 4.1) was added. The samples were then incubated at room temperature for 20 min with gentle shake. Unincorporated dyes were aspirated and the wells were washed thoroughly. Plates were then kept at an angle for 5 min to remove excess water, reaspirated and then stored at -20^0C prior to dye extraction. For quantification of

mineralization, alizarin red stain was removed from the scaffold by treating with 500 μL of cetylpyridinium chloride for 1 h. Then 200 μL of the extract was taken in a microtiter plate and the absorbance was recorded in a microplate spectrophotometer (Biotek PowerWave XS) at 550 nm. Scaffolds without hMSCs treated following the same protocol were used as control.

4.4.8.4 RUNX2 expression

The osteogenic differentiation capacity of MSCs seeded constructs were also assessed by evaluating the expression of RUNX2 by immune cytochemistry using fluorescence microscope [139]. As per the procedure described above, MSCs seeded scaffolds were incubated. The constructs were then fixed and permeabilized with 100% precooled methanol for 10 min. FBS were added for non-specific blocking of the reaction. The constructs were treated with primary antibody, RUNX2 (1:1500 in PBS) and incubated overnight at 4^0C. After washing with FBS, the samples were treated with FITC conjugated 20 antibody (1:1500 in PBS) and incubated for 1 h. The cell samples were then subjected to counter staining with HOEST for 2 min after PBS washing and then confocal microscopy images were taken.

4.4.8.5 Osteocalcin expression

After 14 days of culture in osteogenic media as described above, the cell-scaffold constructs were extracted and fixed using 70% ethanol in 1×PBS for 15 min at room temperature. The fixed cells were washed twice in 1×wash buffer (1×PBS containing 0.05% Tween-20). To induce the permeability of the cells, 0.1% Triton X-100 in 1×PBS solution was added for 5 min and then washed twice with a wash buffer. Afterwards, the samples were incubated for 1 h at room temperature in 5% BSA/1× PBS followed by the addition of anti-osteocalcin (anti-OCN) antibody (1:1000, Abcam Biotechnology) and incubated overnight at 4^0C. Following incubation, the cells were washed 3 times for 5 min with a 1×wash buffer. Goat anti-rabbit IgG-TRITC (1:500, Santa Cruz Biotechnology) and FITC-conjugated phalloidin (1:40, Invitrogen) in 1×PBS were added for double staining and cells were then incubated again for 1 h at room temperature [16]. The cells were washed with 1×wash buffer for 5 min for three consecutive times. The samples were stained by DAPI (1:1000, Chemicon) for nucleus staining and then inverted onto cover slips, mounted, visualized and photographed by a fluorescence microscope.

4.4.8.6 Osteocalcin activity

A quantitative estimation of osteocalcin activity was done by enzyme linked immunoassay kit (Biomedical Technologies) following manufacturer's protocol. The assay is a sandwich immunoassay employing two monoclonal antibodies directed toward the amino and carboxy terminal regions of osteocalcin. Briefly, 25 µl of medium from the cell-scaffold constructs was added to the strip plates coated with primary antibodies followed by the addition of 100 µl of secondary antibody with incubation for 2.5 h. The samples were then aspirated and washed thoroughly with a buffer. 100 µl of streptavidin horse radish peroxidase was added to the plates and incubated again for 30 min. Finally 100 µl of substrate was added after washing the plates in buffer and allowed to develop color in dark for 10 min. 100 µl of stop solution was added and absorbance was read at 450 nm. The amount of osteocalcin was calculated from the absorbance using a standard curve.

4.4.8.7 Morphological study of differentiated MSCs

The electrospun SF nanofibers were collected on a round glass slip of 15 mm diameter and nHAp was deposited on the surface by alternate soaking in $CaCl_2$ and sodium phosphate solution. The mineralized fibers were sterilized under UV light for 3 h and washed thrice in PBS for 15 min to remove any residual solvent present. Thereafter, fiber coated glass slides were immersed in complete medium (DMEM F12 medium/10%FBS 1%antibiotics) overnight before cell seeding. The passage 4 MSCs were then seeded on scaffolds with a cell density of 10^4 cells/well. After 48 h of cell incubation, the cell scaffold constructs were cultured in osteogenic media and after 2 weeks of growth, the cover slips were visualized under inverted microscope to observe cell morphology.

4.4.9 Statistical Analysis

Statistical significances were determined for all types of scaffold samples for a number of triplicates and p values were generated by ANOVA using Benferronies test for multiple comparisons to one control ($p_{0.05}$>3 assay). This assay method relies on assumption of normality and homogeneity of variation of distribution.

CHAPTER 5

Results and Discussion

PART I

Development of spinnable SF blend from eri and tasar silk

SF derived from silk worm cocoon has been considered as a potential biomaterial for developing tissue engineered scaffolds because of its robust mechanical strength, desired biocompatibility and suitable biodegradability properties. For application in bone tissue engineering, scaffold should possess a desired set of tailored properties like high porosity, high mechanical strength, surface hydrophilicity and roughness etc. SF derived from *B. mori* silk has been widely studied by several scientists to develop scaffolds. However, *B. mori* SF has low hydrophilicity as well as roughness that limit its application in bone tissue engineering. Keeping this in view, an attempt has been made to explore different silk worm cocoons that are grown locally having superior properties compared to the most widely used silk *B. mori*. Among various types of silk worm cocoons, tasar silk has been reported to have better surface properties due to the presence of cell binding epitope RGD and high content of hydrophilic amino acids in tasar silk as compared to other silks [79]. In addition, tasar silk also possess anti-inflammatory, cytocompatibility and cell adhesive properties. Though all these properties make tasar an excellent candidate as scaffold material, it is not readily spinnable because of the presence of bulky group of amino acid chains. On the other hand, eri silk contains amino acids with positive charge that enhances cell attachment in addition to having lowest inflammatory activity among all varieties of silk available in India [140]. Moreover, eri silk is highly crystalline than any other non-mulberry silks and has excellent blending possibilities with other fibers like wool, cotton and polyester [141]. It is thus hypothesized that the combination of the properties of these two varieties of silks may be useful to develop a novel biomaterial that can be used for scaffold development for possible bone tissue engineering application. So in this part of research work, an effort has been given to develop SF blends from eri and tasar silk by finding a suitable solvent system for successful spinning of this blend to prepare electrospun nanofiber.

5.1.1 Selection of solvent for the preparation of spinnable SF blend

The selection of suitable solvent or solvent system to make a particular polymer spinnable is a fundamental requirement [142,143]. It is critical to find a desirable solvent system when a new polymer is explored for making electrospun fibers as in the present case of eri and tasar SF. So a number of widely used solvents were examined for their suitability to prepare spinnable solution of eri and tasar SF and the results are described here.

Effect of single solvent system

Widely used solvents namely formic acid [88], choloroform [126,144,145], trifluro-acetic acid [126], hexa-fluro-iso-propanol [87] and water [84] for the preparation of spinnable SF solution from conventional *B. mori* were investigated in this study to make SF solution. The solubility and electrospinnability of SF solution in different solvents are tabulated in Table 5.1 and 5.2. The concentration of SF solution was 9% w/v for all the cases, selected based on the literature [144]. Table 5.1 shows that SFs derived from eri and tasar are soluble in all solvents except chloroform in which these are sparingly soluble. However, SF solutions are not spinnable.

Table 5.1: Solubility and spinnability of eri and tasar SFs in different solvents

Solvent	**Eri silk fibroin**		**Tasar silk fibroin**	
	Solubility	**Spinnability**	**Solubility**	**Spinnability**
Chloroform	Sparingly	Spray	Sparingly	Spray
Formic acid	Fully	Spray	Fully	Spray
HFIP (Hexafluro isopropanol)	Fully	Transition-spin	Fully	Transition-spin
TFA (Trifluro acetic acid)	Fully	Spray	Fully	Spray
Water	Fully	Spray transition	Fully	Spray transition

The possible reason for the limitation of spinnability of SF solution is the increase in geometrical bulkiness of the amino acid chains. It has been reported that easily fitted amino acid chain can crystallize effortlessly facilitating electrospinning while bulky group of amino acid chains fits the fiber lattice improperly reducing the fiber forming ability. The ratio of bulky to non-bulky amino acid in case of *B. mori* is 0.18, whereas the values are 0.24 and 0.33 for eri and tasar silk respectively [147]. Therefore, an attempt has been made to formulate a binary solvent system to make eri and tasar SF spinnable. In this context, several reports have indicated that chloroform can improve the electrospinnability of different polymers when used as a co-solvent [148]. In another study, Shenoy et al. have reported the effect of solvent suggesting that mixing solvents of lower solubility with higher solubility can produce electrospinnable solutions at lower critical concentration of polymer by promoting phase separation [149]. It is further reported that binary solvent system may be beneficial and appropriate for dissolving a particular solute or polymer

blend to allow electrospinnability. Keeping this in view, the binary solvent system using chloroform as co-solvent was explored for making SF solution or its blend.

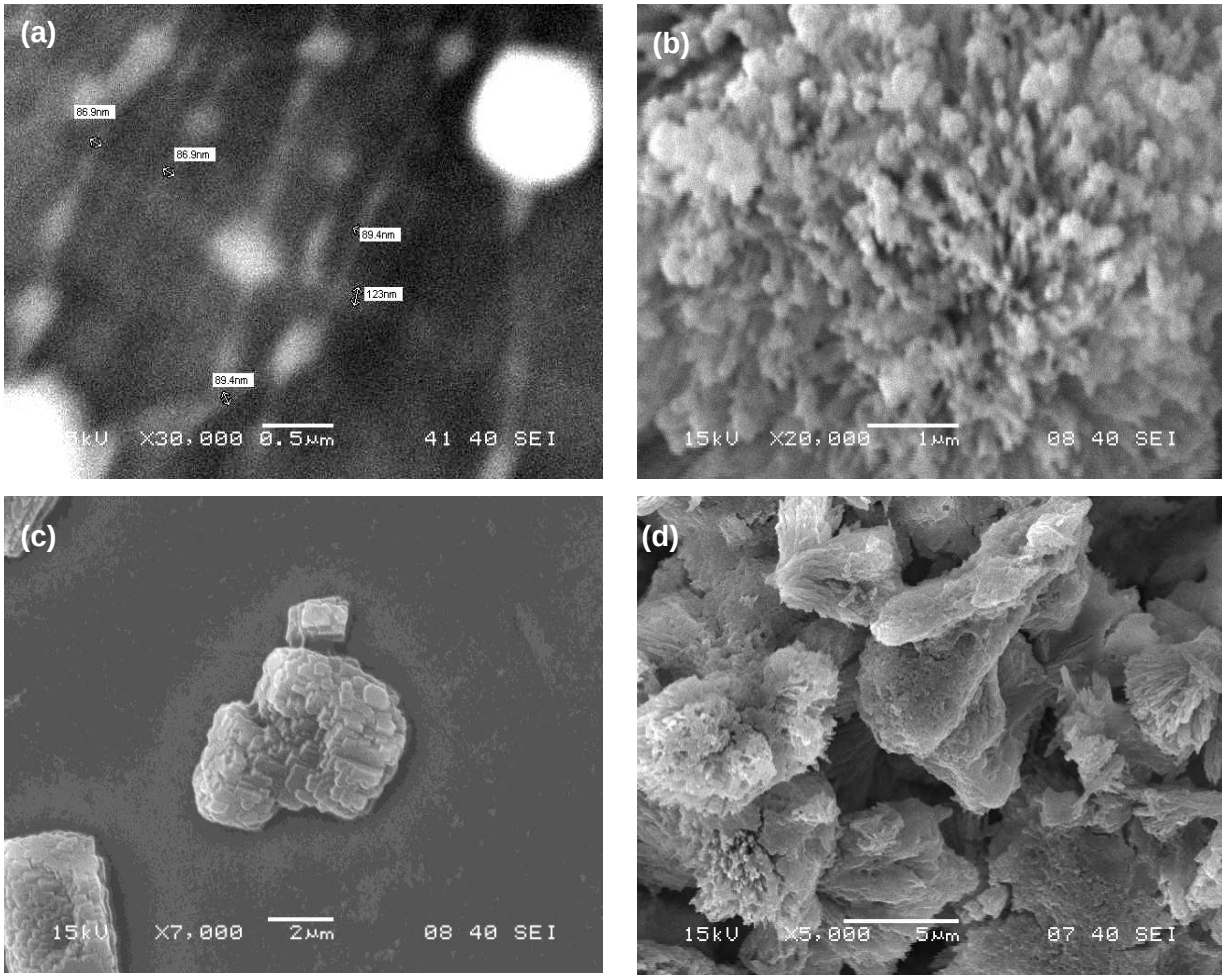

Figure 5.1: Electrospinnability of (a) eri and (b) tasar SFs with formic acid as solvent (c) eri and (d) tasar SFs with TFA as solvent

Among other solvents, fiber produced from *B. mori* SF using HFIP was reported to be highly brittle due to its high volatility and also very expensive. On the other hand, SF is highly soluble in water and is very difficult to make spinnable at low concentration. Furthermore, though fiber is formed at very high concentration (>30% w/v), the fiber diameter obtained is in micrometer range rather than nanometer that is most desirable for tissue engineering. The unsuitability of TFA as a solvent for eri and tasar SFs is revealed from SEM images as shown in Figure 5.1 (c) and (d). No fiber formation is observed with tasar using both TFA and formic acid. Further, fiber-like morphology is found in case of eri silk using formic acid whereas TFA fails. Based on

the above fact, formic acid was chosen as a possible solvent to make a binary solvent system with chloroform.

Effect of binary solvent system

As it is justified above, formic acid and chloroform in combination were chosen as a possible binary solvent to develop spinnable solution from eri and tasar SFs. Different batches of binary solvent systems was prepared in varying ratios of formic acid and chloroform. The prepared solvent mixtures were evaluated for their suitability for making SF solution spinnable by testing in the electrospinning machine and the optimum ratio of solvents mixture was established. The experimental results are shown in Table 5.2.

Table 5.2: Spinnability of eri and tasar SFs in different ratios of formic acid and chloroform

Formic acid % v/v	**Chloroform % v/v**	**Spinnability of eri**	**Spinnability of tasar**
90	10	No Fig (b)	No Fig (a)
80	20	No Fig (g)	No Fig (d)
70	30	Spinnable Fig (i)	No Fig (e)
60	40	Spinnable Fig (j)	No Fig (f)
50	50	No Fig (c)	No Fig (h)

It is noticed that not a single binary solvent system is able to make electrospun fibers from tasar. Furthermore, among the solvent systems used under study, the one prepared with 70:30 and 60:40 formic acid:choloroform ratios were found to be effective for fiber formation from eri SF. This is further evident from SEM images as depicted in Figure 5.2.

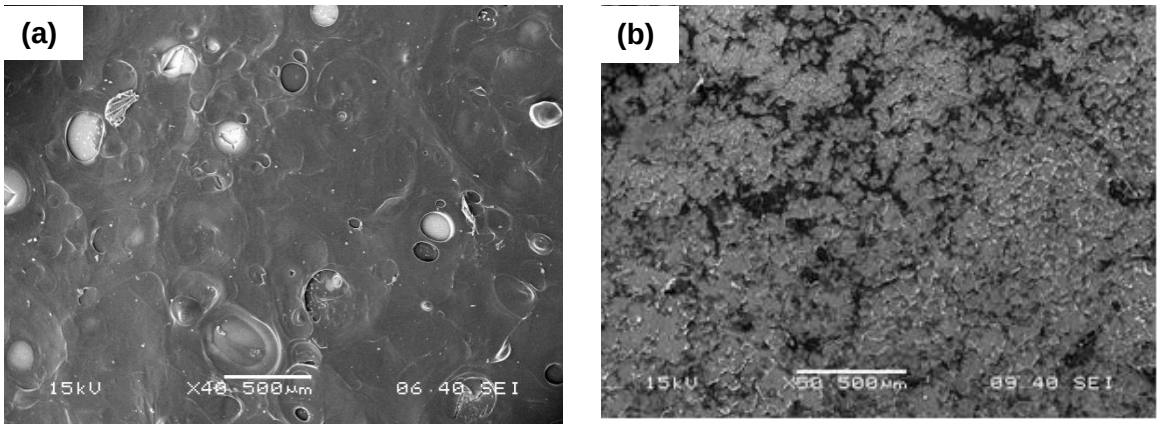

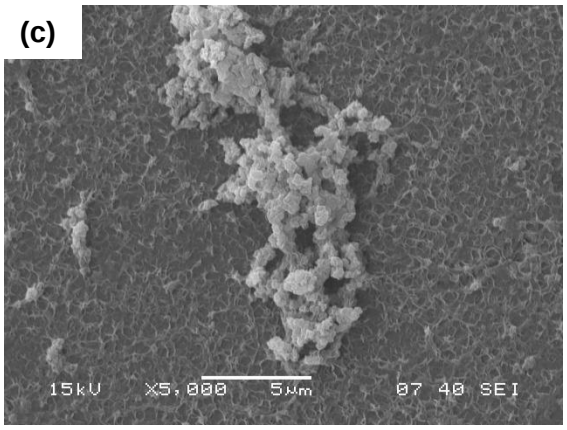
(c)
15kV X5,000 5µm 07 40 SEI

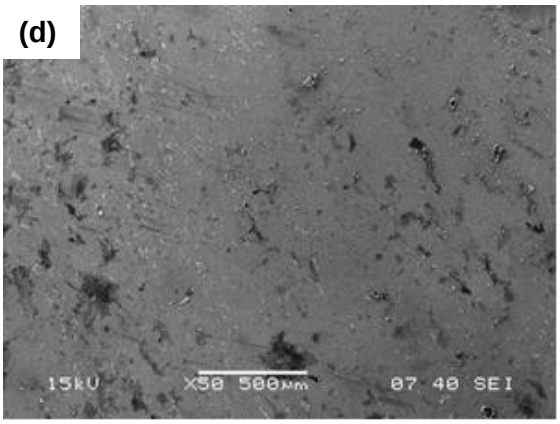
(d)
15kV X50 500µm 07 40 SEI

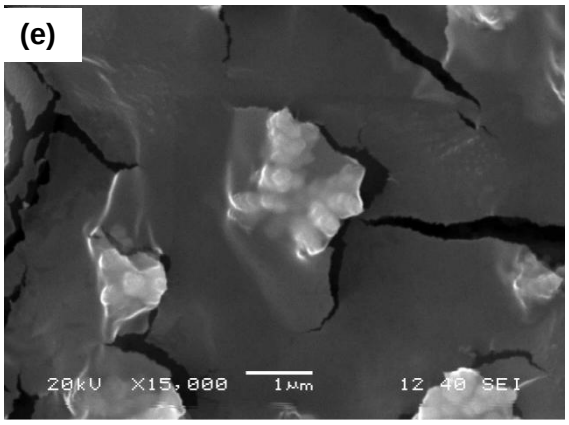
(e)
20kV X15,000 1µm 12 40 SEI

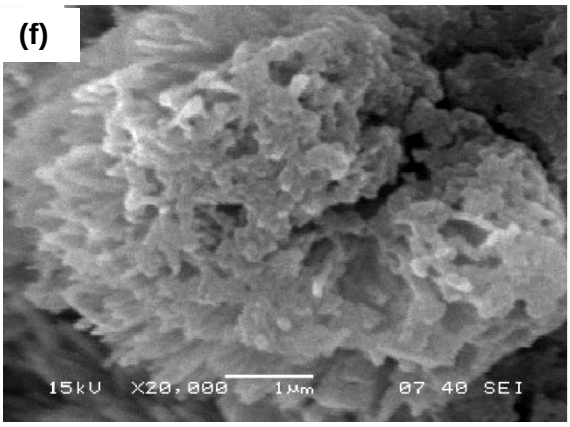
(f)
15kV X20,000 1µm 07 40 SEI

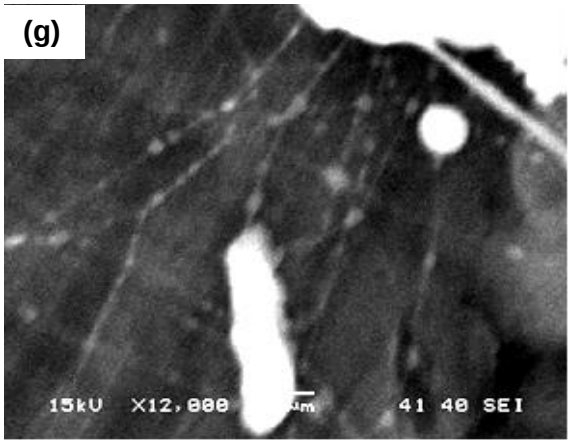
(g)
15kV X12,000 41 40 SEI

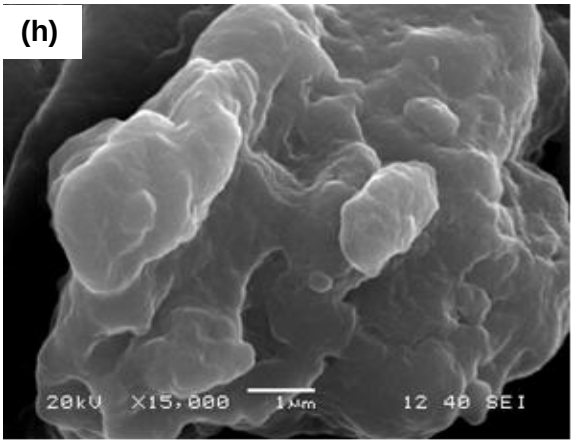
(h)
20kV X15,000 1µm 12 40 SEI

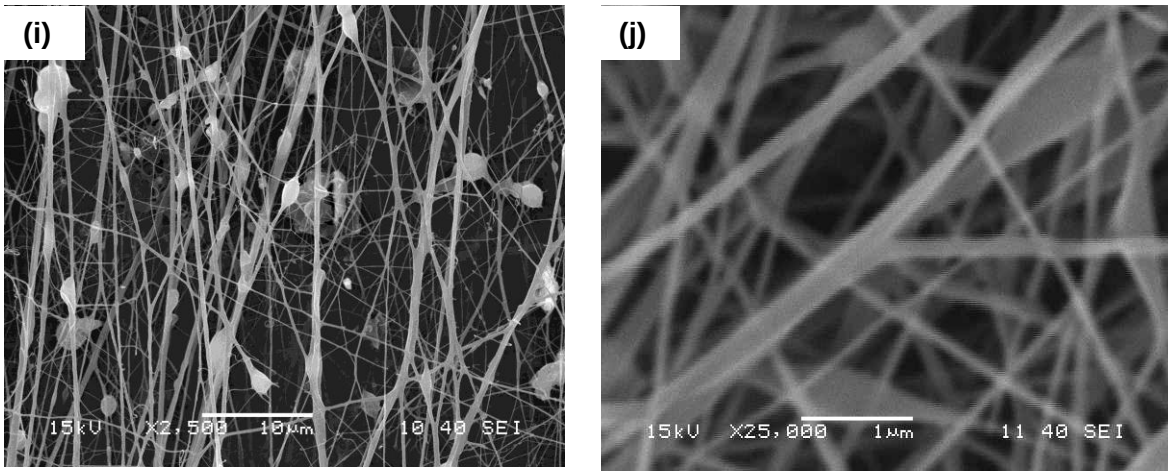

Figure 5.2: SEM images showing spinnability of eri and tasar SFs in different ratios of formic acid and chloroform (a) no spinnability of tasar (b) no spinnability of eri (c) no spinnability of eri (d) no spinnability of tasar (e) no spinnability of tasar (f) no spinnability of tasar (e) no spinnability of eri (f) no spinnability of tasar (g) no spinnability of eri (h) no spinnability of tasar (i) spinnability of eri (j) spinnability of eri

5.1.2 Selection of optimum SF blend composition

As it is seen in previous section that SF derived from tasar is not spinnable. However, it is evident from literature that it is an attractive biopolymer with superior cell supportive properties than other type of SF including eri. Therefore, an attempt has been made to make SF derived from tasar electrospinnable by blending with spinnable eri SF using the selected solvent composition. Different batches of SF blends with varying compositions were prepared and the blends were subjected to electrospinning to produce SF fibers. The electrospinning result is shown in Table 5.3 and SEM images in Figure 5.3.

Table 5.3: Effect of SF blend composition and solvent ratio on fiber formation

Formic acid: chloroform	**eri:tasar**			
	90:10	**80:20**	**70:30**	**60:40**
70:30	Irregular fiber Figure (c)	Beaded fiber Figure (b)	Beaded fiber Figure (e)	No fiber figure (f)
60:40	Fiber Figure (g)	Fiber figure (h)	Fiber Figure (d)	Micron sized powder figure (a)

From Table 5.3 and SEM images (Figure 5.3), it was observed that both solvent ratio and blend ratio have great influence on fiber formation. Fiber formation was found to be more favorable using 60:40 solvent ratio than with 70:30 irrespective of the polymer blend composition. In case of latter, fiber formation was observed to be either irregular or beaded which may be attributed to the increase in concentration of chloroform that decreases the dielectric constant and increases volatility of the solvent mixture [150,151]. Thus it is demonstrated that 60:40 is the optimal formic acid:chloroform solvent ratio.

Furthermore, so far as SF blend composition is concerned, fiber was found to be formed with all SF blend ratios except SF blend with 60:40 ratio of eri:tasar. The progressively better fiber formation in terms of fiber diameter as measured from SEM images was achieved with blend containing higher content of SF derived from eri. Comparable though slightly higher fiber diameter was obtained using SF blend with higher amount of tasar up to 30%. Keeping in view of utilizing the maximum amount of tasar as desirable, blend with 70:30 eri:tasar was selected as the optimum SF blend for further studies.

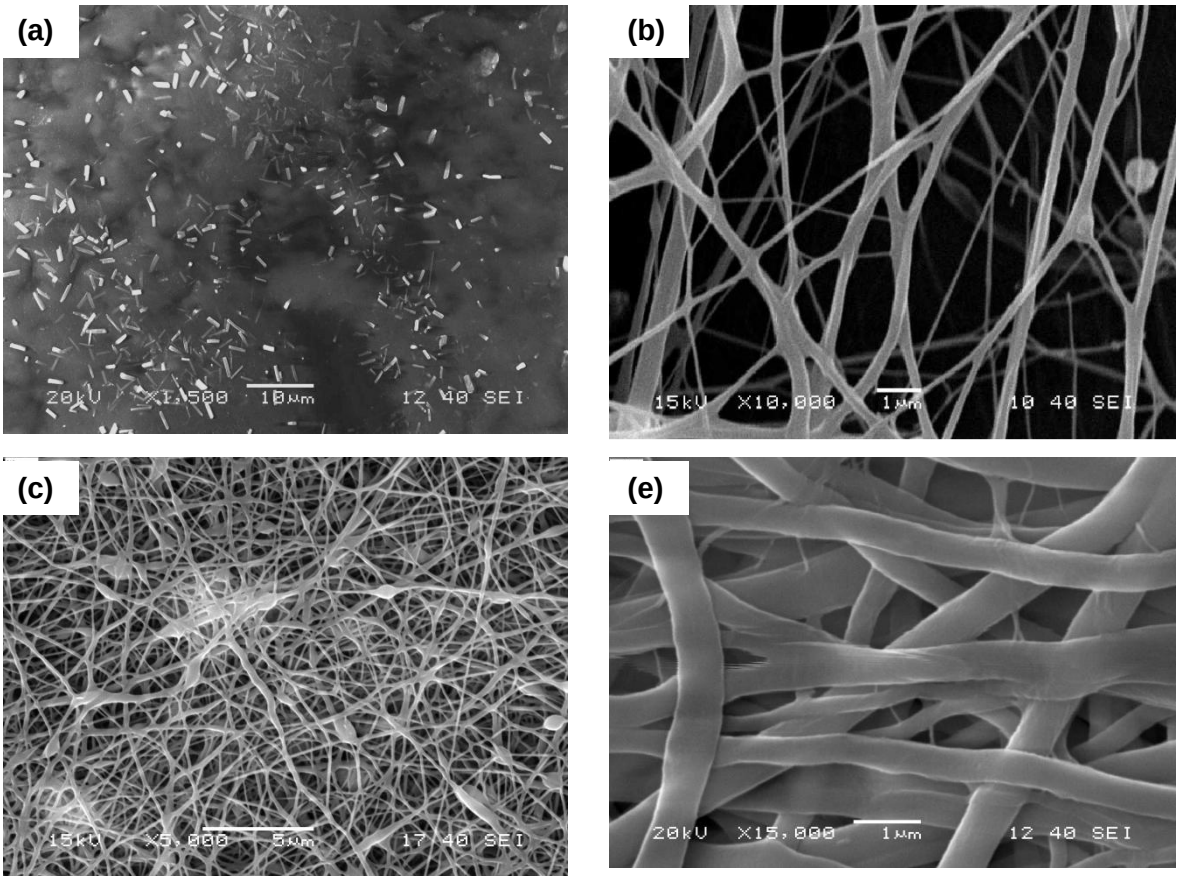

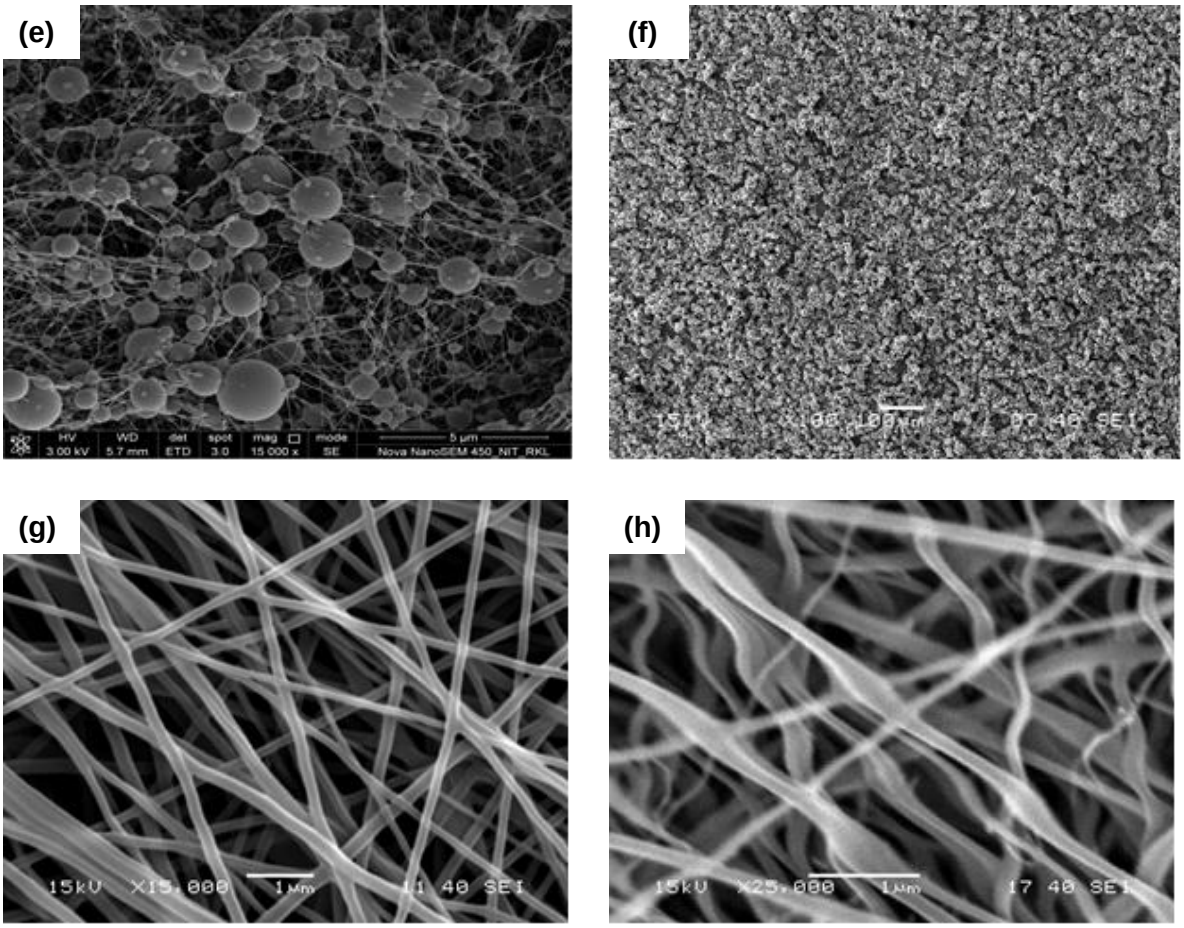

Figure 5.3: SEM images of different SF blend composition at solvent ratios of formic acid and chloroform (70:30 and 60:40) (a) Micron sized powder (b) beaded fiber (c) irregular fiber (d) fiber (e) beaded fiber (f) no fiber (g) fiber (h) fiber

5.1.3 Effect of SF blend concentration on fiber formation

Previous study has suggested that polymer solution concentration is one of the most influential factors that significantly affect electrospinnability of solution and morphology of electrospun nanofiber. It has been reported that the value of critical minimum concentration is dependent on the molecular chain length, chemical nature of polymer and type of solvent system for a selected polymer [152,153]. Therefore, the effect of polymer solution in varying concentration in the range 6-9% w/v was investigated on the spinnability and morphology of fiber formation from SF blend to obtain the optimal concentration. The electrospinning condition is performed with an applied voltage varying between 18 kV, tip-collector distance 15 cm and flow rate 0.8 ml/hr

throughout the experiment. The first two parameters were adjusted to maintain a continuous fiber formation. The experimental result is shown Figure 5.4.

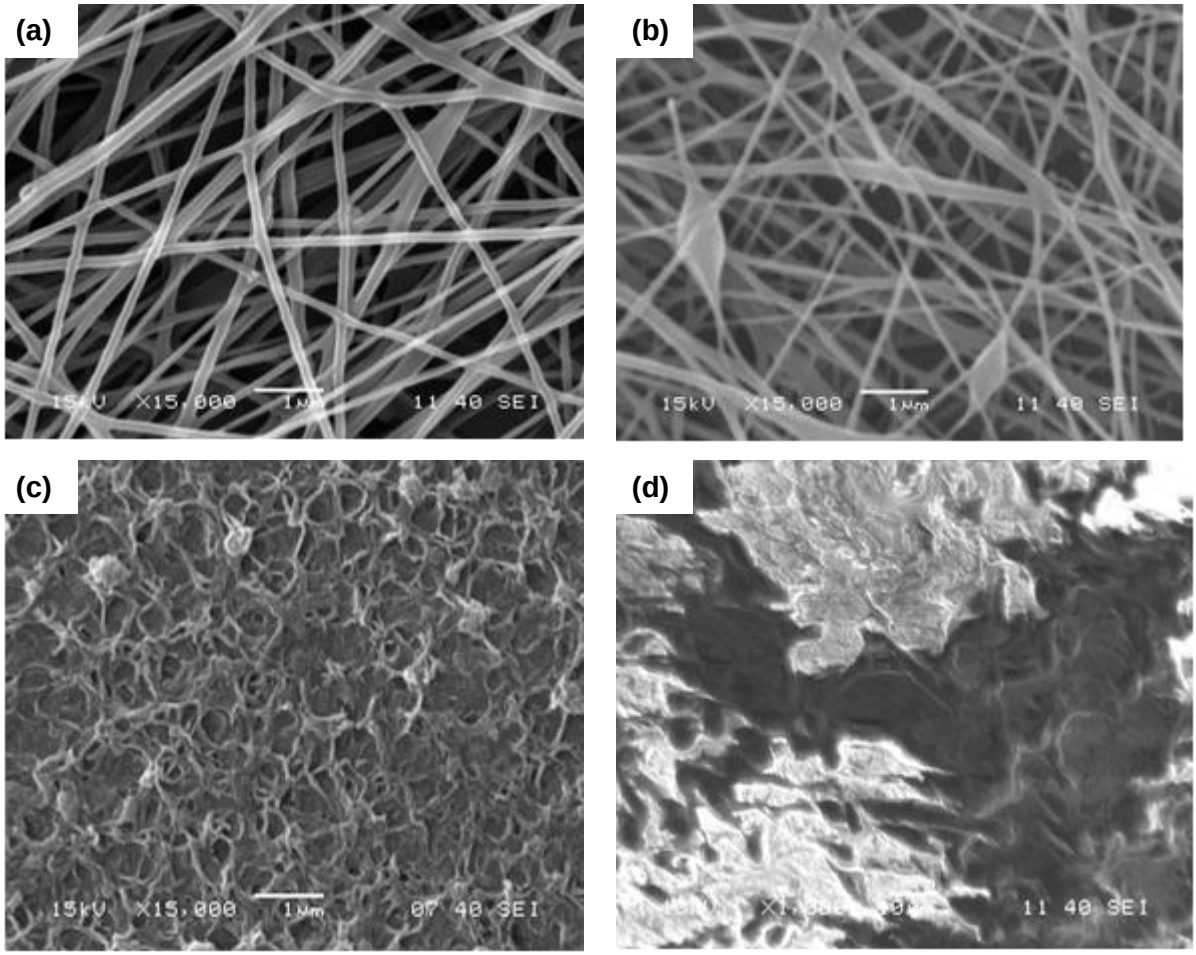

Figure 5.4: Effect of SF concentration on nanofiber formation (a) 9% (b) 8% (c) 7% (d) 6% SF blend concentration

It is observed from SEM images that fiber formation is highly dependent on the concentration of polymer blend. The minimum blend concentration for fiber formation is 8% w/v below which no fiber is formed. Furthermore, though clear fiber formation was obtained using higher concentration of blend (9%), 8% is considered as the most favorable for producing less fiber diameter which is desirable for tissue engineering scaffold development.

5.1.4 Properties of SF blend solution

Specific viscosity and surface tension

Viscosity and surface tension have strong influence on fiber formation from polymer. The viscosity of a polymer solution is directly proportional to fiber diameter whereas surface tension helps in the formation of stable pendant droplet (formation of Taylor cone at the needle tip) thereby, facilitating fiber formation. From Table 5.4 it has been observed that with the decrease in SF concentration, specific viscosity of the solution decreases while surface tension does not vary significantly. Hence, a direct relationship between the concentration of blend solution and specific viscosity has been suggested.

Table 5.4: Effect of total concentration of SF blend on viscosity of solution

Concentration	**Silk composition (eri:tasar)**	**Solvent composition\ (FA:Chloroform)**	**Specific viscosity**	**Surface tension (mN/m)**
9%	70:30	60:40	70.5	26.85
8%	70:30	60:40	64.8	26.02
7%	70:30	60:40	53.1	25.67
6%	70:30	60:40	48.6	25.32

Stability of SF blend solution

Storage time has a great influence on the shear viscosity that ultimately affects the spinnability of a polymer solution. Therefore, it is important to check the stability of SF blend solution over time. Figure 5.5 represents the change in shear viscosity of SF blend as a function of time. After a slight decrease in shear viscosity (within 1st few hours) at the initial stage, viscosity increased up to 2-3 h and thereafter, a decline in trend in shear viscosity was observed. This phenomenon may be explained as during the initial phase some transition in form might have occurred which is followed by the formation of aggregate resulting in an increase in viscosity; the decrease in viscosity is probably due to decomposition of polymer. As it is seen from Figure 5.5, SF blend solution is stable up to 4 days with desired spinnability characteristics.

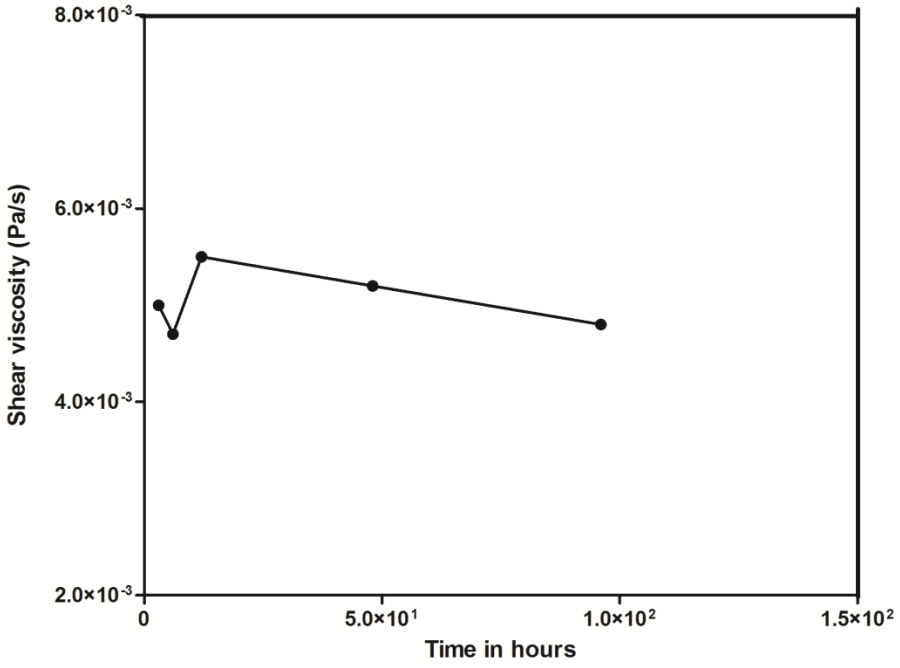

Figure 5.5 Change in shear viscosity of SF blend as a function of time

5.1.5 Conclusion

The main aim of the present work was to develop a spinnable SF blend solution from eri and tasar silk by selecting a suitable solvent system. Spinnable SF blend was prepared successfully by selecting a binary solvent mixture consisting of 60:40 v/v formic acid and chloroform. 8% w/v is established as the optimum concentration of SF blend solution for nanofiber formation. Furthermore, the stability of the SF blend solution was found to be 96 h for nanofiber formation.

PART II

Development of electrospun nanofibrous SF blend scaffold

As it has already been mentioned that the design and fabrication of a 3D scaffold from suitable biocompatible and biodegradable polymeric materials is one of the key challenges in bone tissue engineering. In scaffold designing, architecture and molecular composition are reported to be most critical. It is important to understand whether the developed scaffold serves as a mere passive substrate or rather actively affects cellular and synthetic processes involved in ECM formation. Biomaterials derived from natural biopolymers e.g. SF are potential candidates to meet the requirement of the latter because of their intrinsic bioactive properties whereas the development of a 3D nanostructured scaffold is an essential feature that can regulate vital cellular functions such as adhesion, proliferation, migration and differentiation.

Keeping above issues in view, in previous chapter, a novel scaffold material was developed from SF blend derived from eri and tasar silk and further non-woven electrospun nanofibers were made from the blend successfully by electrospinning. In this phase of thesis work, research has been further extended to fabricate 3D nanostructure from the developed nanofibers by electrospinning. These scaffolds were further characterized for surface, mechanical and biological properties. The results and discussion are described in this chapter.

5.2.1 Fabrication of electrospun 3D nanofibrous SF blend mat

To achieve continuous nanofiber deposition on the collector, the three important electrospinning parameters voltage, tip-collector distance and flow rate were adjusted to compensate the decrease in conductivity of collector plate as observed during electrospinning. The corresponding range of these parameters were varied with applied voltage between 18-22 kV, flow rate 0.5-0.8 ml/h and tip collector distance 15-12 cm. The entire process was carried out at 65% relative humidity at room temperature. Finally, a 3D mat of thickness 300±10 μm was prepared by layer-by-layer deposition of SF nanofibers generated by electrospinning. It was observed that the electric field varied within 1.2-1.8 kV/cm range during the entire process.

5.2.2 Characterization of scaffold

The prepared 3D nanofibrous scaffolds were characterized for morphological, mechanical, structural, thermal and biological characterization to find its suitability in bone tissue engineering application.

5.2.2.1 Morphological studies

The morphology of the prepared nanofibrous mat was characterized by SEM, AFM and TEM. The results are described below.

SEM Analysis

SEM images (Figure 5.6 a) revealed that SF fibers are randomly aligned which is attributed to continuous deposition of nanofiber. Further, on close observation (Figure 5.6 b), it is shown that these randomly oriented nanofibers (in the selected area of analysis) lead to interconnected voids resulting in porous structure of the scaffold. The fiber diameter was found in 200-500 nm range, average being 350 nm. They were observed to be more or less uniform throughout its entire length while the deposition is non-uniform in nature which is possibly due to the change in conductivity of the collector with increase in surface deposition [154].

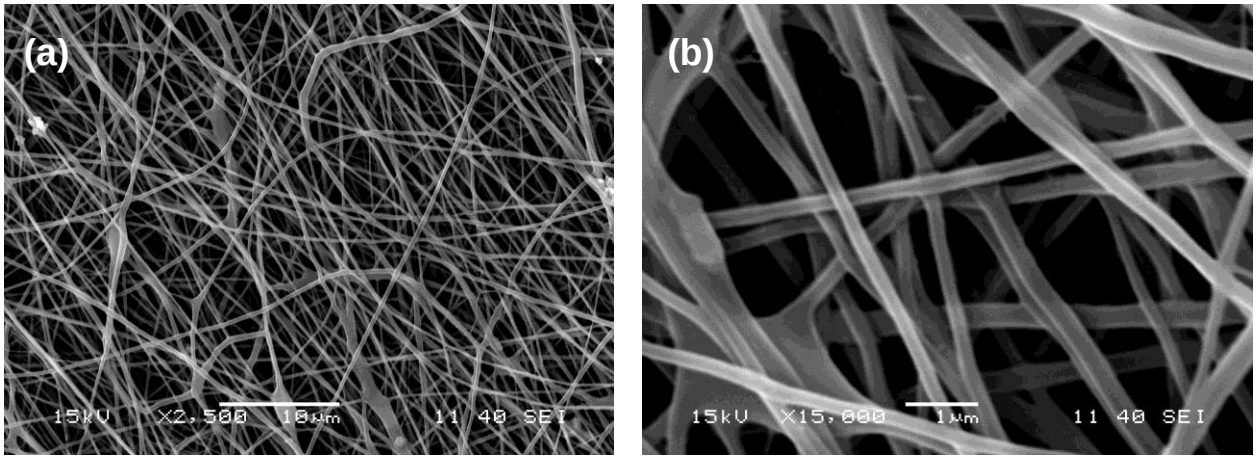

Figure 5.6: SEM images of eri-tasar SF blend nanofibrous mat. Images taken at 2500 and 15,000 magnification. Images show randomly oriented nanofibers with interconnected voids.

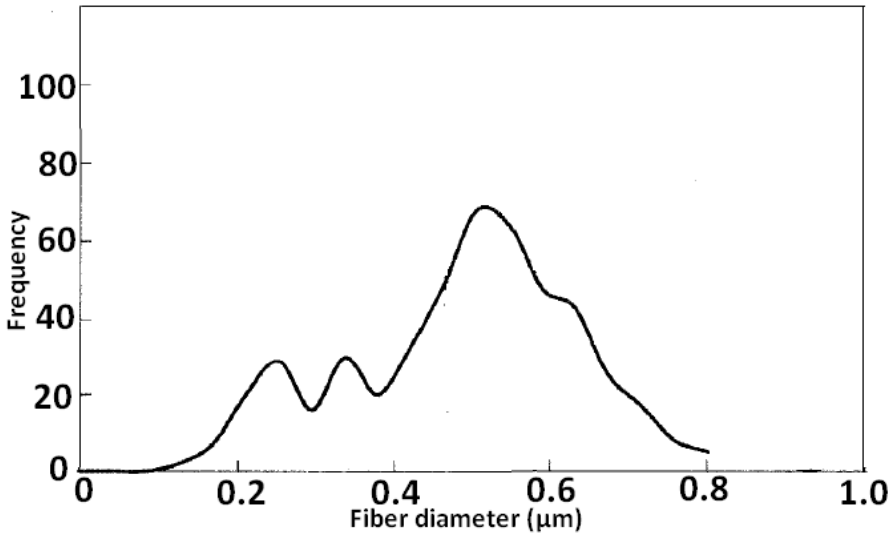

Figure 5.7: Distribution of electrospun fibers diameter with random orientation

The statistical distribution of fiber diameter was also analyzed by NIH Image J software by taking SEM images at high magnifications >2500X and 5000X. 20 different Figures have been taken for the analysis for an approximate ~500 measurements that were recorded to plot the graph (Figure 5.7). The fiber diameters thus measured were found within the range 200-750 nm with majority of fibers in 200-500 nm range. The variability in fiber diameter is similar to the variation in fiber diameter of natural ECM and thereby, speculates to mimic the natural microenvironment by providing large number of binding sites for cell attachment as reported earlier [155].

AFM analysis

Surface roughness is an important property for cellular adhesion and immuno compatibility of scaffold. The surface roughness of the prepared scaffolds was measured by AFM as shown in Figure 5.8 (a-e). The average roughness of 3D nanofibrous scaffold was found to be in the range 0.387-0.4387 µm which is highly favorable for cytocompatibility and protein adsorption for successful tissue regeneration [156,157].

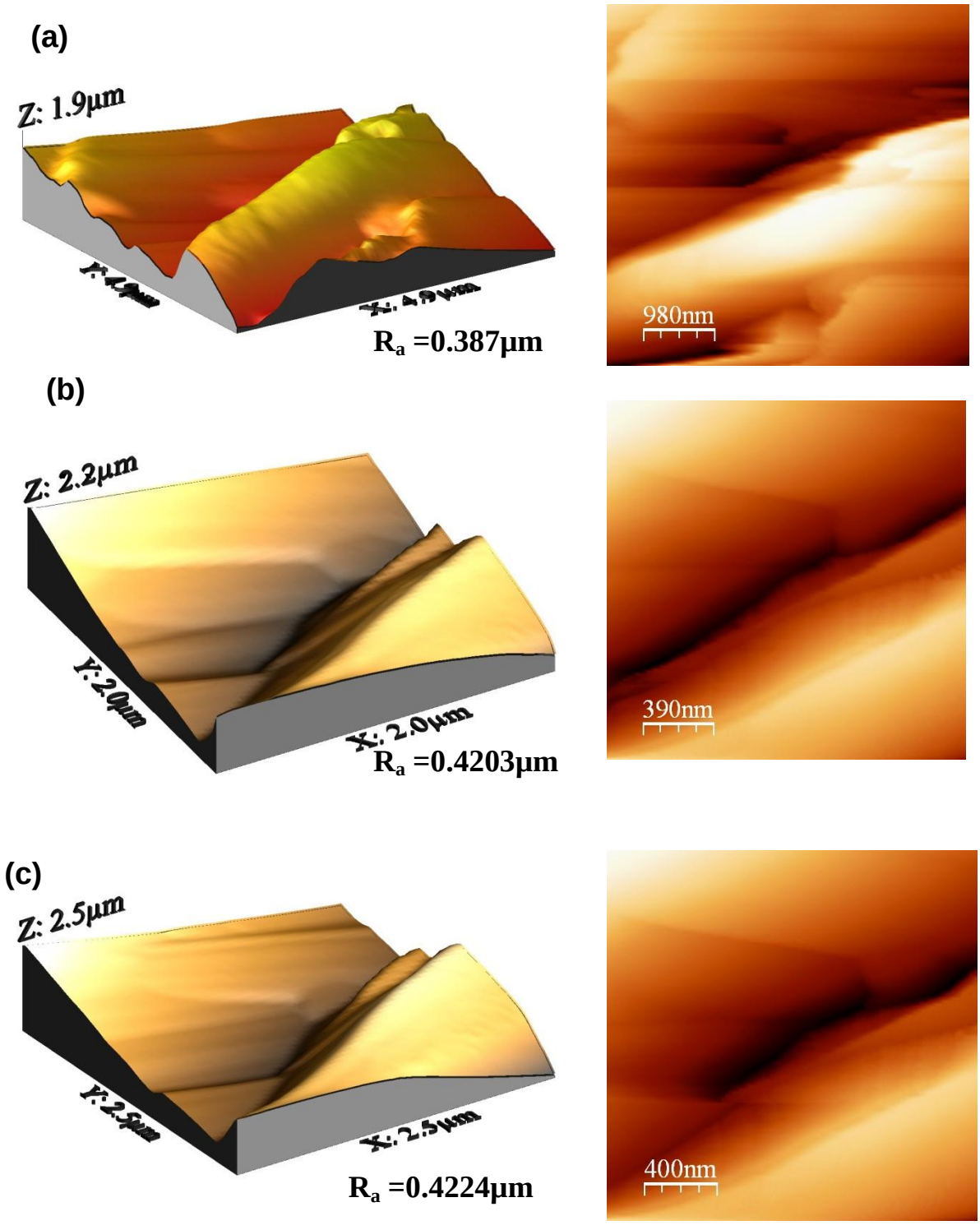
(a)
Z: 1.9µm
980nm
R_a =0.387µm
(b)
Z: 2.2µm
Y: 2.0µm
X: 2.0µm
390nm
R_a =0.4203µm
(c)
Z: 2.5µm
Y: 2.5µm
X: 2.5µm
400nm
R_a =0.4224µm

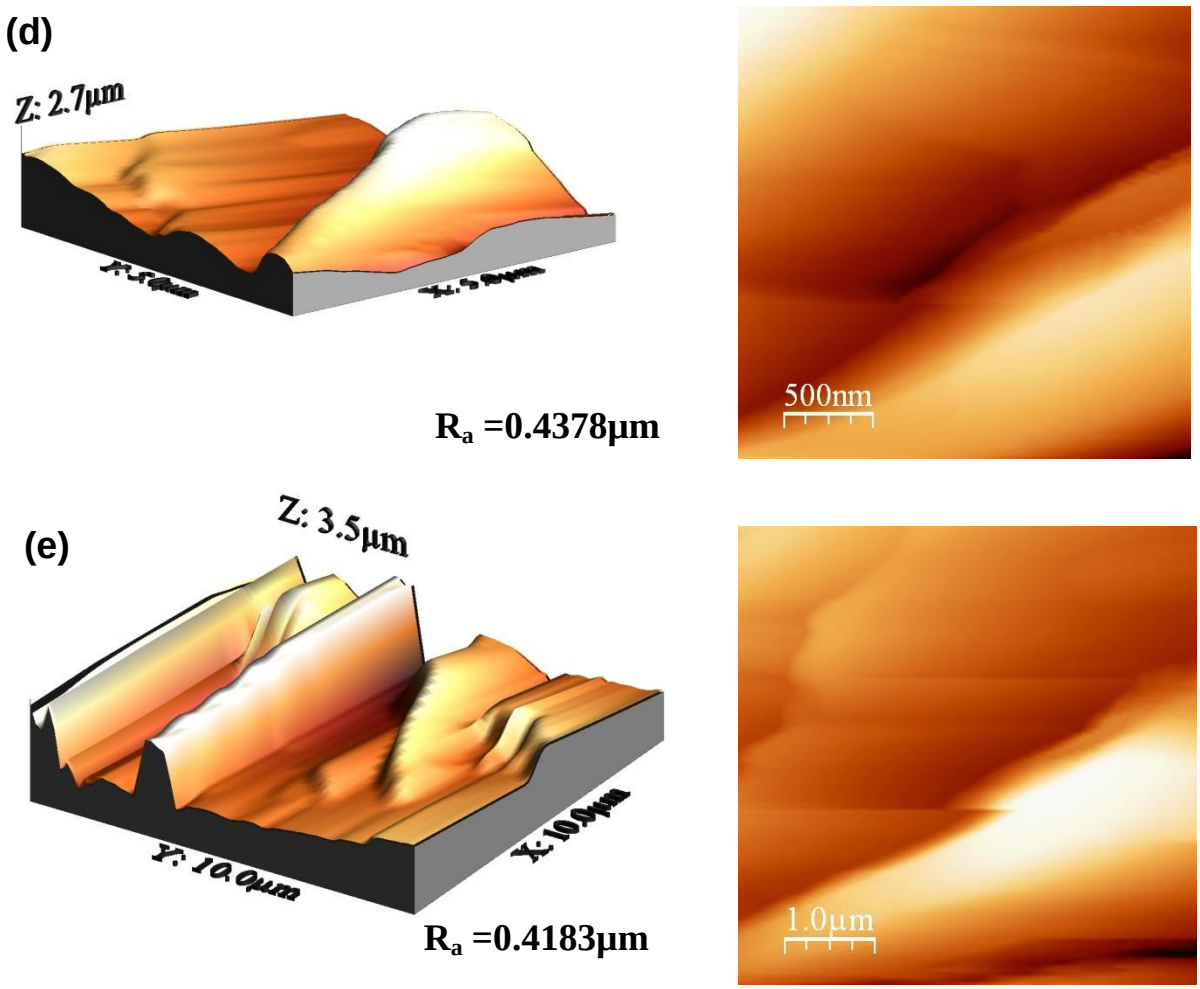

Figure 5.8: Average roughness of SF blend mat as expressed at 5 different positions TEM analysis

The shape and smoothness of nanofibers are further observed from TEM images. As observed in Figure 5.9, individual fibers were found to be flat and smooth.

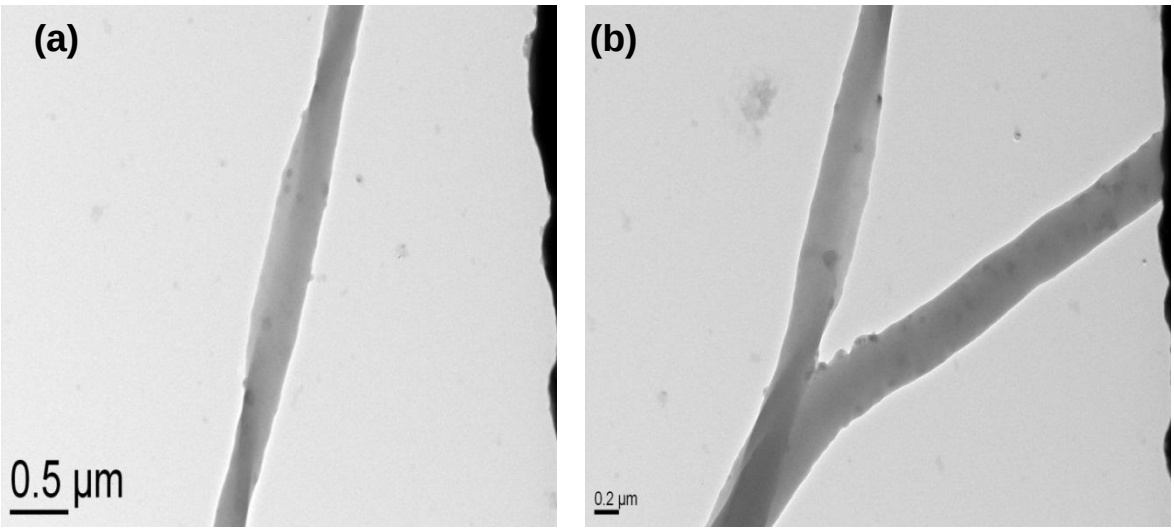

Figure 5.9: TEM images of a single nanofiber representing its shape and surface view.

5.2.2.2 Porosity and pore size distribution

Figure 5.10 shows the relationship between differential intrusion volume and pore size. Majority of pore sizes of the 3D mat (scaffold) was measured to be within 2500-5000 nm range and the ratio of pore diameter to fiber diameter was 3:4.

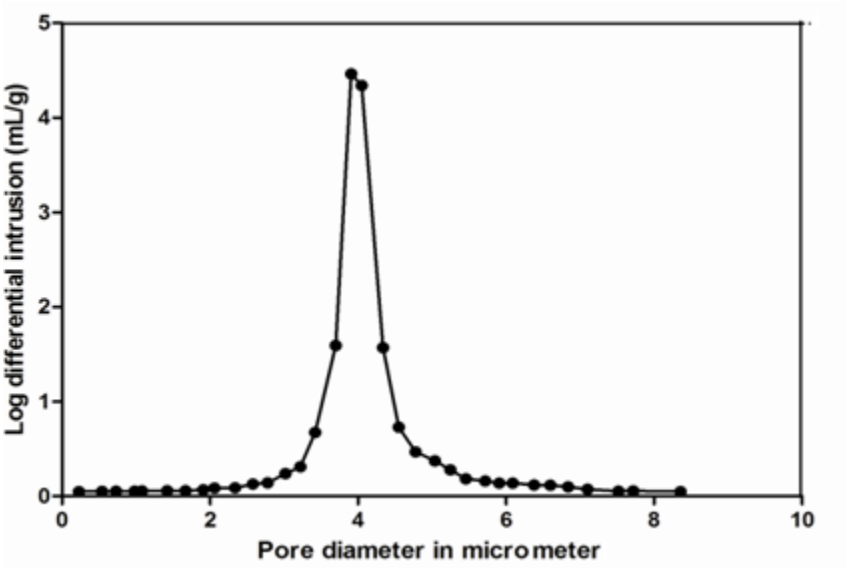

Figure 5.10: Plot of differential intrusion volume vs. pore diameter of electrospun SF blend nanofiber

The average porosity of the scaffold was measured as 79±5%. This porosity range is favorable for effective transfer of nutrients, oxygen and disposal of metabolic byproducts essential for survivability of any tissue engineered construct [158]. Pore shape plays a significant role in cellular proliferation and especially on differentiation of MSCs [159].

The volume of intrusion was observed to be less than that of measured volume as evident from Figure 5.11. This may be due to trapping of some mercury at depressurization step within void space that was unable to extruded [124]. This incomplete removal of mercury causes hysteresis loss for electrospun nanofibrous mat. This is supposed to be a result of existence of ink-bottle type of pores with a small throat to cavity ratio. It is to be noted that in case of cylindrical pores the hysteresis loss is minimum ~0. The adhesion, growths and proliferation of cells over scaffold require proper exchange of nutrients, growth factors, gases (O_2 and CO_2) and waste products. Presence of ink bottle type of pores speculates that the above transport will follow non-Higuchi's equation i.e. release is regulated by physical and elastic property of nanofiber in addition to diffusion [160].

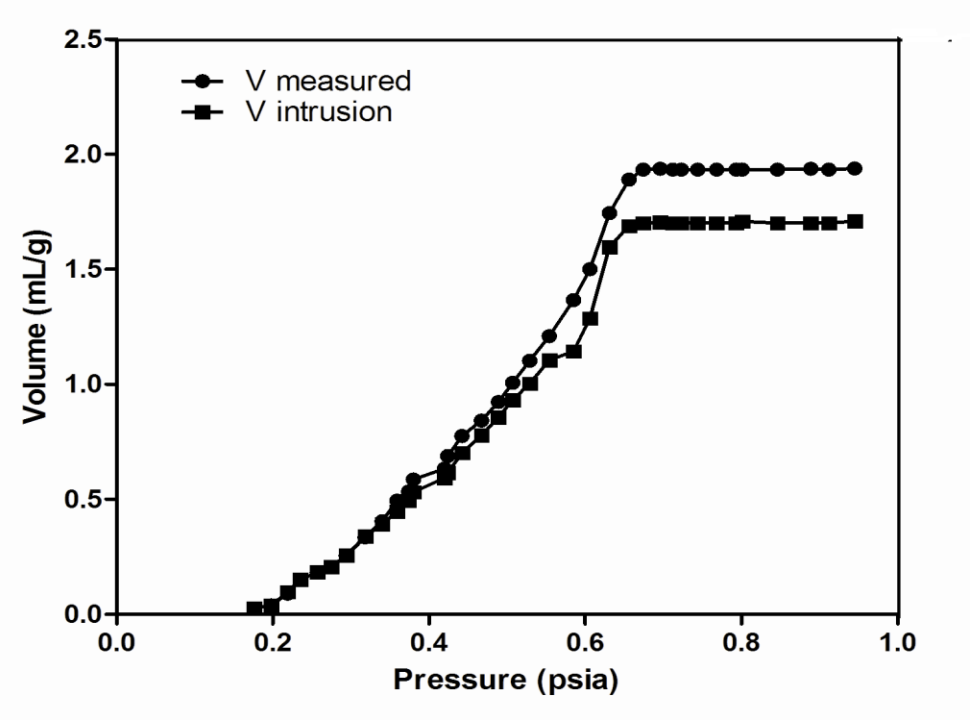

Figure 5.11: Plot of measured and corrected intruded volume vs. pressure for electrospun samples with fiber diameters 0.3-0.6 µm

5.2.2.3 Structural analysis

XRD diffractogram (Figure 5.12) shows the diffraction pattern for SF blend nanofibrous scaffold at 20.55 (2θ) and corresponding space d=4.387 Å for α-helix structure and it is diffraction for β-structure 29.54 (2θ) and space = 3.123 Å [93,159] indicating the presence of α and β structure in the nanofibrous mat.

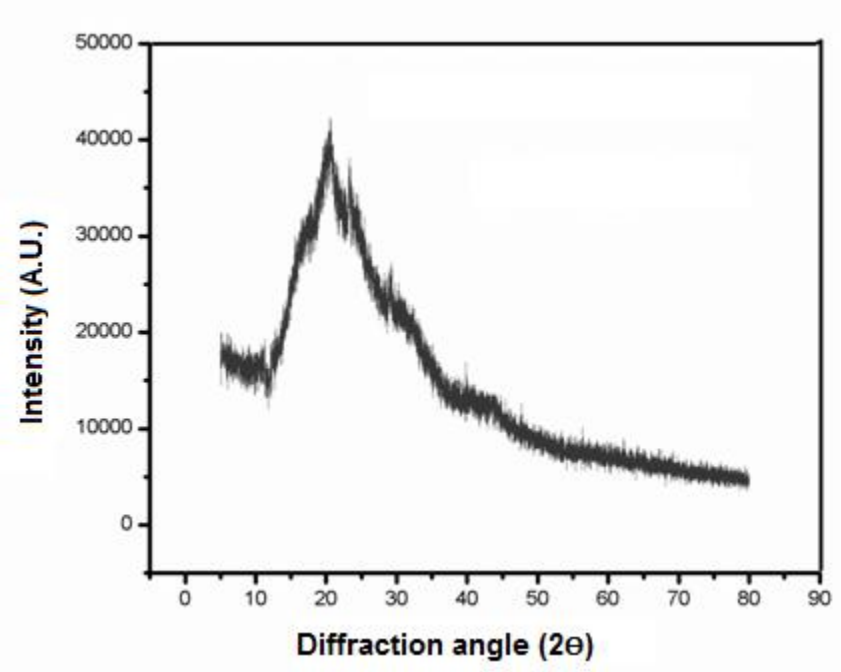

Figure 5.12: XRD analysis of SF blend nanofibers

FT-IR spectrum was carried out for eri-tasar SF scaffold to confirm the presence of functional groups in the SF blend scaffold. From Figure 5.13, it was observed that the C=O stretch vibration of amide I band absorbed at 1658 cm^{-1} and N-H bending of amide II band absorbed at 1530 cm^{-1} for both SF blends as observed from the presence of two prominent peaks [94].

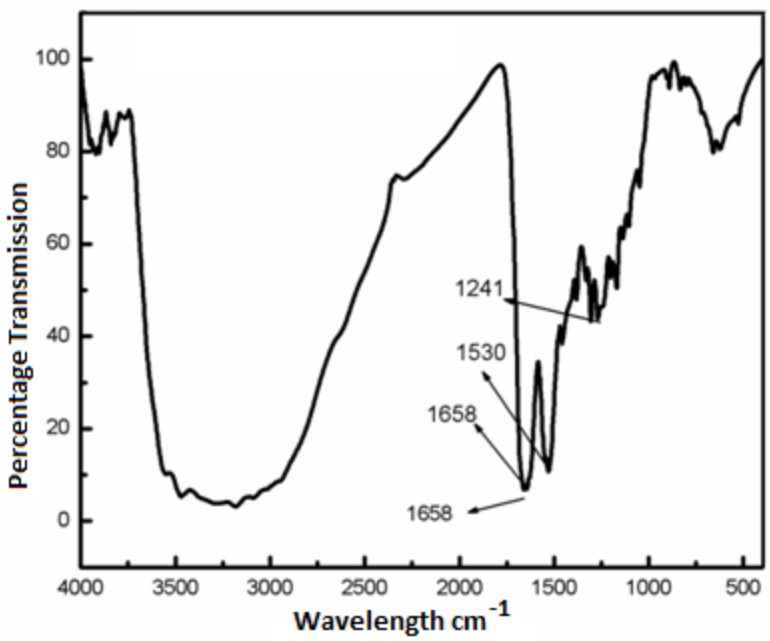

Figure 5.13: FT-IR analysis of SF blend nanofibers showing functional groups of SF

5.2.2.4 Thermal analysis

From Figure 5.14 of TGA, the weight loss occurred about 7-8% at 100^{0}C due to water evaporation from SF blend scaffold which is insignificant. The blended SF scaffold started to decompose around 250-300^{0}C and its residual weight loss was about 20%. Further increase in temperature of the scaffold produced severe decomposition at 350^{0}C and weight loss around 45-50% due to the peptide bond breaking into amino acid as reported earlier [162].

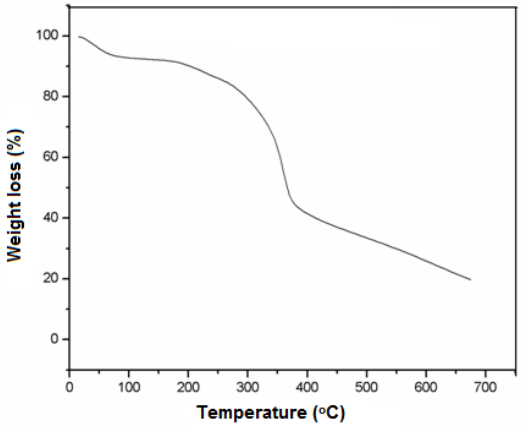

Figure 5.14: TGA of eri-tasar SF nanofibrous scaffold

5.2.2.5 Mechanical properties

The tissue engineered scaffold must have high tensile strength which is an essential factor to withstand in vitro cell growth and neo tissue organization. Moreover, scaffold must have desired elastic modulus to facilitate osteogenic differentiation of cells. Therefore, the tensile strength and % elongation of the prepared scaffold were measured by a mechanical tester. Figure 5.15 (a-b) shows a load-extension graph of eri-tasar and BM silk fibroin nanofibrous scaffolds indicating ultimate tensile strength at maximum load. It is observed that SF blend (ET) nanofibrous scaffold show a higher UTS (1.83 Mpa) and percentage of extension (7.256%) as compared to widely used scaffold derived from BM (UTS 1.378) and (5.917%). The higher UTS and % extension represent higher ductile nature of SF blend scaffold as compared to BM scaffold. The mechanical properties of cancellous bone tissue is a function of anatomic location and the wide range of tensile strength values have been reported by different researchers, for example, proximal tibia (0.2 to 6.7 MPa [163], proximal femure (0.2 to 14.82 MPa) [164] and vertebral bodies (0.3-7 MPa) [163]. Thus it has been demonstrated that the developed nanofibrous scaffold posses desired mechanical property suitable for various non-load bearing bone tissue engineering application. Furthermore, the ET scaffold is superior in mechanical property than the most widely used *Bombyx mori* scaffold.

(a)

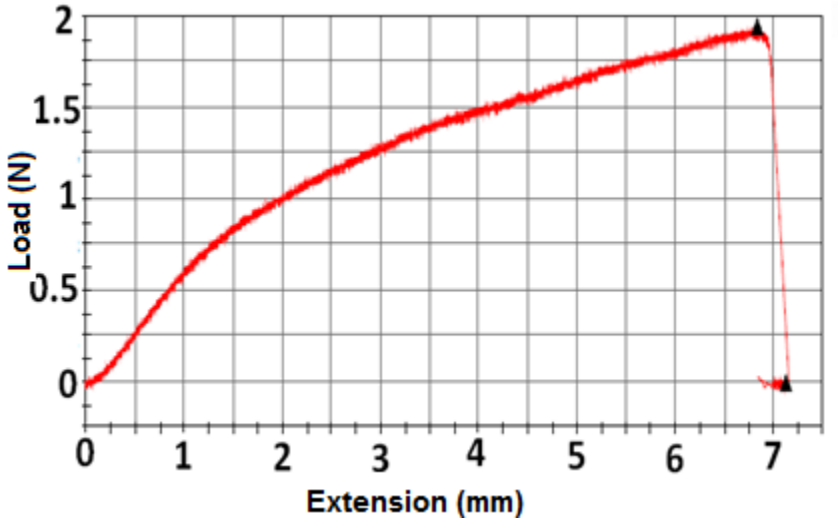

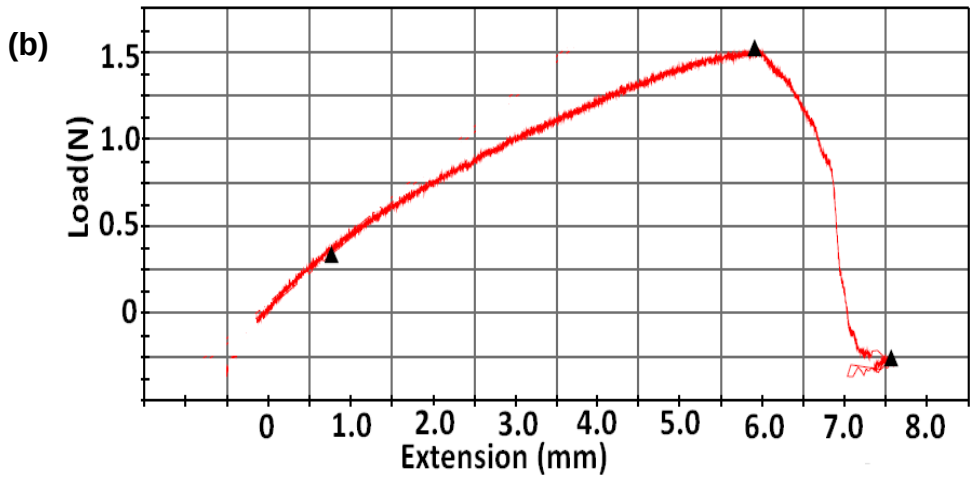

Figure 5.15: Typical load vs. extension curve of (a) SF blend (eri-tasar) and (b) B. mori nanofibrous scaffold.

5.2.2.6 Water uptake capacity and contact angle measurement

The hydrophilic of scaffolds is determined by swelling property and contact angle measurement. The measured properties were also compared with *B. mori* nanofibrous scaffold. Figure 5.16 shows the swelling index of SF blend and *B. mori* scaffold for a 96 h to determine the equilibrium swelling ratio and onset of material degradation. Figure 5.16 indicates that there is a gradual increase in water uptake capacity of the scaffold with time and maximum at about 30 h. Afterwards there is no further change in water uptake representing the attainment of equilibrium. The maximum % water uptake and corresponding swelling ratio of SF blend is 43% and 0.73 respectively. The values are also found to be higher than the water uptake (37%) and swelling ratio (0.64) observed with *B. mori* scaffold that represent superior surface property (hydrophilicity) of SF blend (eri-tasar) scaffold than the widely used *B. mori* scaffold. Furthermore, the water uptake capacity and corresponding swelling ratios measured based on distilled water and PBS are nearly same.

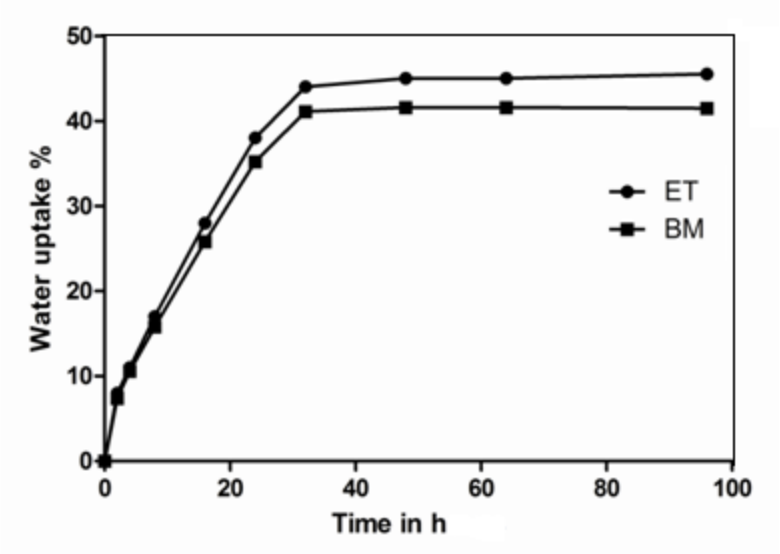

Figure 5.16: Water uptake capacity of SF blend and BM scaffolds for 96 h of treatment in SBF

The high hydrophilic property of SF blend can be explained owing to the presence of higher hydrophilic amino acid [80] content compared to *B. mori* scaffold. Higher hydrophilicity of SF blend scaffold facilitates better transport of nutrients, growth factors and gas exchange that favors cell attachment and immunocompatibity [165]. The nanofibrous mats were further found to be visibly fragmented after 96 h of treatment and hence further experiment was not appropriate for data analysis. However, the measured contact angle of SF blend (eri-tasar) and *B. mori* nanofibrous mat in water were found to be 54.7±1.80 and 62±2.30 respectively. This further supports the high hydrophilicity of SF blend nanofibrous mat and thereby, its superior surface property.

5.2.2.7 Bioactivity of the scaffold

Bioactivity of 3D nanofibrous scaffold to form bone like apatite reflects its bone binding potential [166,167]. This property improves healing through accelerated regeneration of bone tissue and deposition of HA. Therefore, the bioactive potential of the developed scaffold was assessed by SEM and EDX analysis. It was observed from Figure 5.17 that the white color globular particles deposited on the surface were apparently similar to apatite. This was confirmed by EDX analysis that revealed the ratio of Ca:P as 1.64 and 1.57 for (a) eri-tasar and (b) *B. mori*

nanofibrous mat respectively [168]. The result is in good agreement with the reported value of the ratio of Ca : P in human bone which varies between 1.5-1.7 [169].

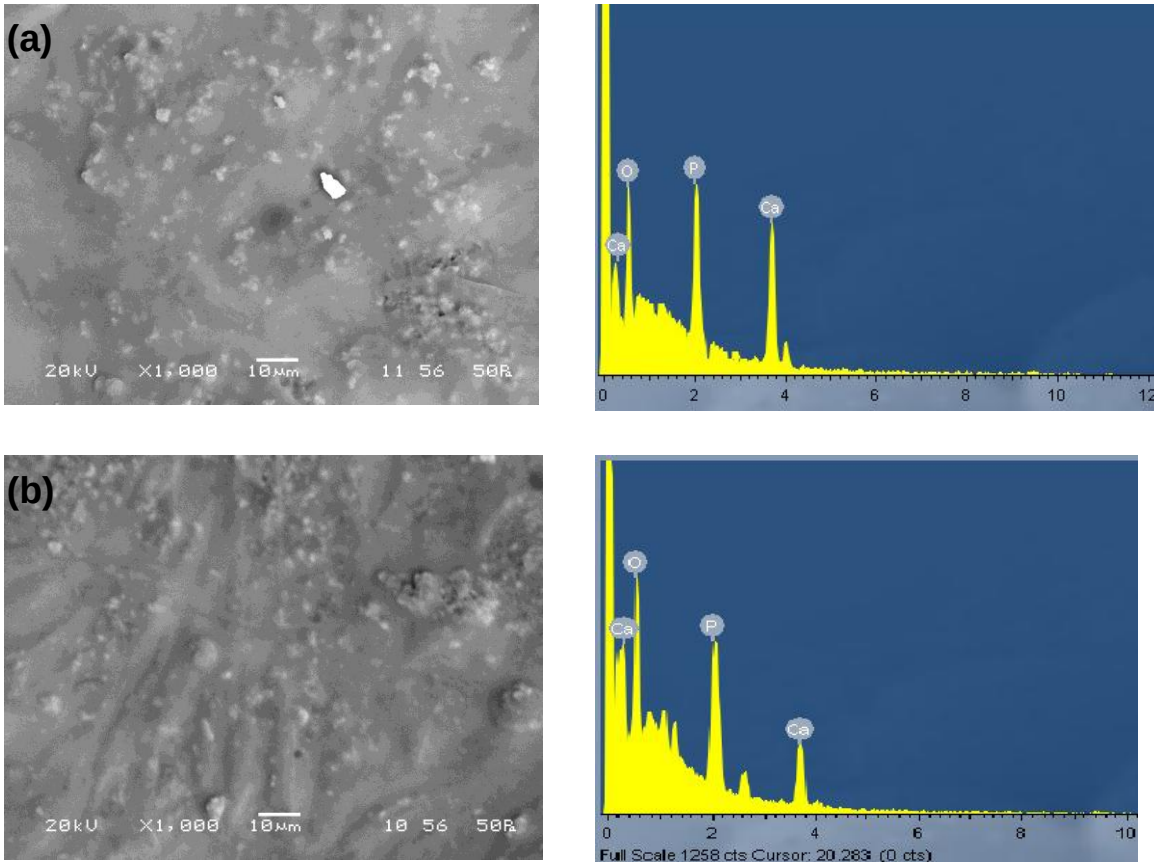

Figure 5.17: SEM images shows deposition of HAp over (a) SF blend and (b) B. mori scaffolds and corresponding EDX figures after soaking in SBF for 14 days

Furthermore, on close observation of images, it was demonstrated that the particles are 0.5-3 µm diameter. The formation of HAp further depicts the growth of HAp crystals over eri-tasar and *B. mori* are comparable. Thus it proves that the scaffold has possessed desired bioactive properties suitable for bone tissue regeneration.

5.2.3 Mechanism of biodegradation

The self-repairing ability of various tissues such as bone, tendon, ligament and vessel are different implying that scaffold should have corresponding degradation rates to facilitate new tissue synthesis. Hence, the degradation control of different scaffold is still the major goal of tissue engineering research. The degradation is a serious issue for silk based material application

in tissue engineering [170]. It is utmost important that the substitute artificial ECM should retain adequate mechanical strength during these period for tissue regeneration in spite of degradation. Additionally, the physicochemical property should not change drastically so that the requirement for complete tissue healing is hindered [171]. Furthermore, literature study suggests that β sheet content play a critical role in degradation of SF nanofibers. During the fabrication processes, silk I which is more amorphous in nature having α sheet configuration transformed into silk II i.e. β sheet configuration possessing more crystallinity. In this present study, the degradation mechanism of SF nanofibrous mat obtained through electrospinning has been established for understanding the correlation between structure, processing and degradability. The study of degradation mechanism would produce a more controlled degradability of SF nanofibrous structure. This will result in regeneration of various tissue structures as per requirement.

5.2.3.1 Biodegradation of silk nanofibrous scaffold

The weight loss due to protease XIV treatment of nanofibrous scaffold at 37^0C and 24 h is shown in Figure 5.18. The figure shows the percentage of degradation increases with time. After 24 h, 24% and 27% weight loss were observed in treated *B. mori* and eri-tasar nanofibrous mat respectively. In contrast, very little weight loss is observed for these nanofibrous mat after 2 weeks in PBS without enzyme. The increased weight loss percentage with eri-tasar scaffold is due to the high content of hydrophilic amino acid with bulky side chain which facilitates water permeation and creates imperfection during fiber formation [172].

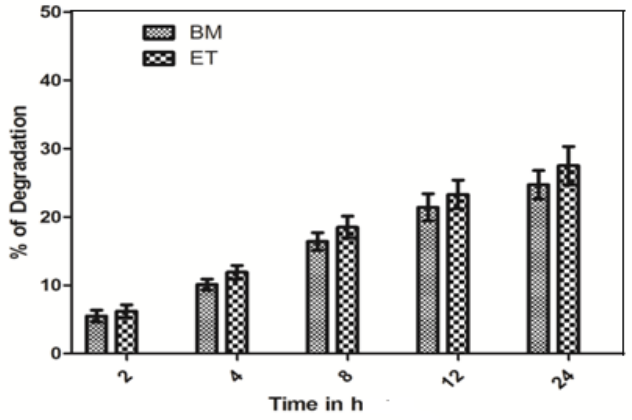

Figure 5.18: Percentage degradation of blended SF blend and B. mori scaffolds in Protease K in SBF (n=5).

Since the eri and tasar silks are different in composition of amino acid and its repeating pattern, a little increase in rate of degradation (3%) has been observed after 24 h of treatment. Further analytical study has been performed to find out the degradation mechanism of eri-tasar nanofibrous sheet.

5.2.3.2 Tensile strength of SF blend nanofibrous mat due to enzyme treatment

The effect of biodegradation by enzyme treatment on tensile strength of scaffold was investigated as shown in Figure 5.19. The result indicates that the enzymatic degradation has an adverse effect on the tensile strength of both eri-tasar and *B. mori* scaffolds. Further, the loss of tensile strength for ET is higher than the loss observed with *B. mori* nanofibrous scaffold.

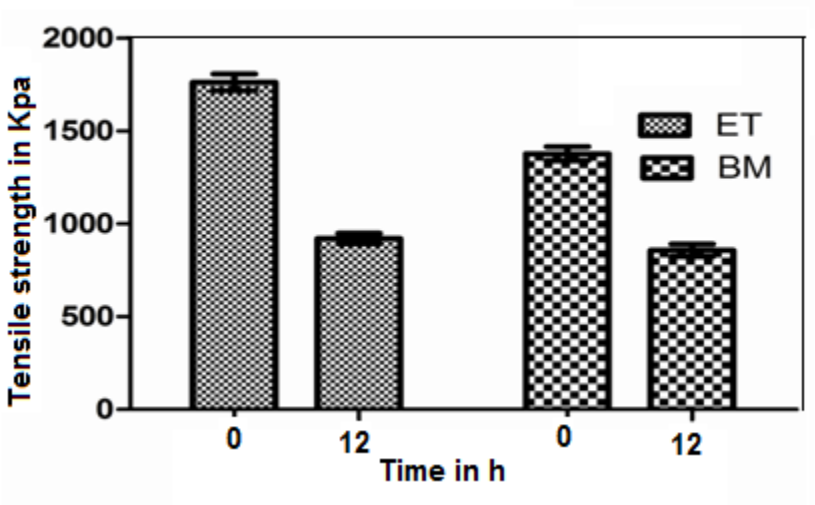

Figure 5.19: Tensile strength of nanofibrous SF blend scaffolds and B. mori before and after enzyme treatment for 12 h

5.2.3.3 Structural changes in SF nanofibrous scaffold upon enzyme treatment

FT-IR

It is important to examine whether degradation has any influence on the conformational changes of scaffolds. FT-IR analysis was performed with 32 scans with a resolution of 4 cm^{-1}, with wave number scanning range from 1200-1800 cm^{-1}. This study has been carried out for identification of functional groups and their conformations. SF consists of 2 types of crystalline structure silk I and silk II [173]. Figure 5.20 (a) represents the IR spectra of SF nanofiber while (b) and (c) represent its enzymatically degraded product after 12 and 24 h respectively implying certain

structural changes. The spectral regions 1700-1500 cm^{-1} are owing to the absorption by peptide backbone and hence used for the analysis of secondary structure with amide I 1700-1600 cm^{-1} and amide II 1600-1500 cm^{-1}. The peaks 1610-1630, 1695-1703 and 1510-1525 cm^{-1} are characteristics of silk II secondary structure and 1648-1654 and 1535-1542 cm^{-1} for silk I conformation [174].

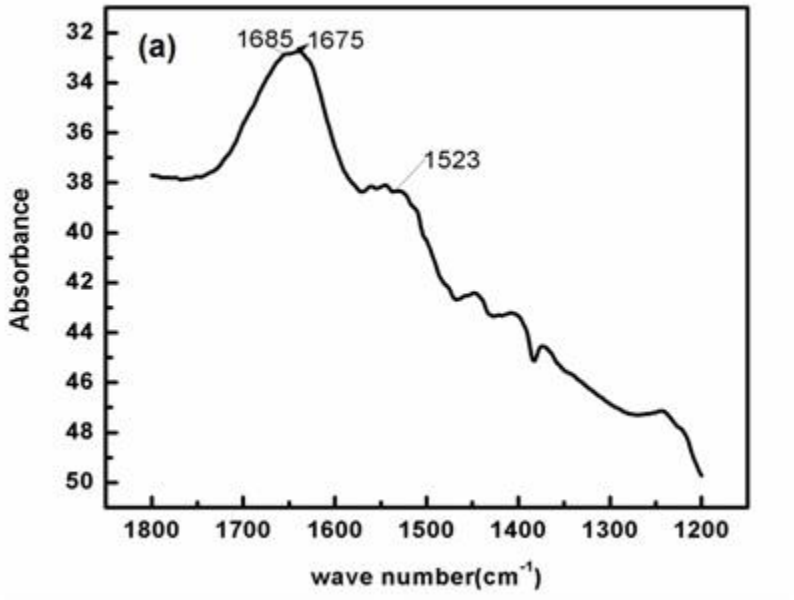

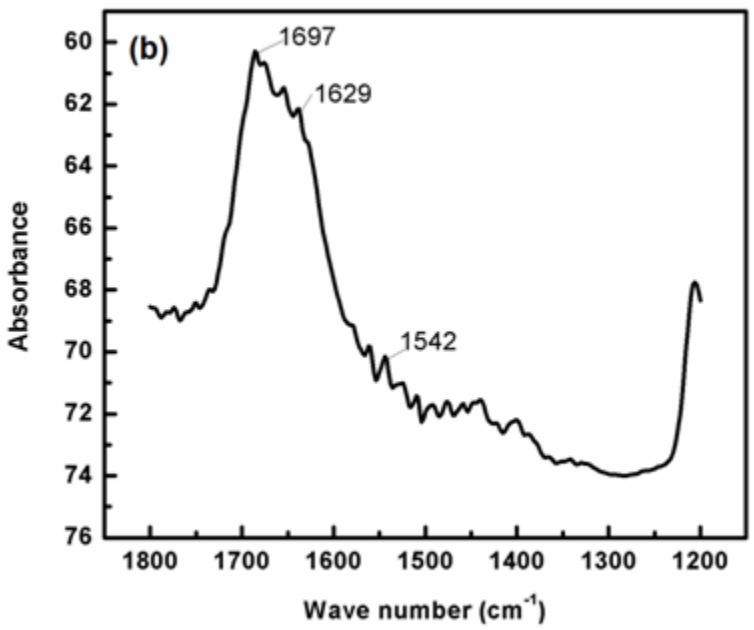

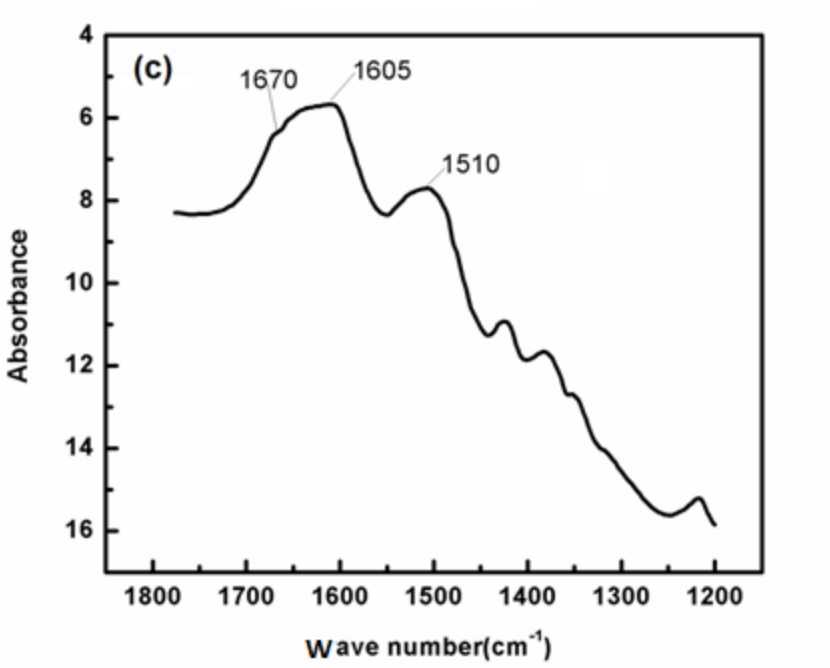

Figure 5.20: FT-IR analysis of degraded SF blend nanofibrous mat that was cultivated in protease XIV solution for (a) 0 (b) 12 and (c) 24 h

It was observed three strong peaks at 1685, 1675 and 1523 cm^{-1} for SF nanofibrous mat in Figure 5.15 (a). The peak 1523 cm^{-1} corresponds to silk II secondary structure while peaks 1685 and 1675 cm^{-1} show the presence of helical turns in SF chain inside the nanofiber [175]. In Figure 5.20 (b), two strong peaks are observed at 1629 and 1697 cm^{-1} corresponding to β-sheet conformation of nanofiber while another weak low intense peak at 1542 cm^{-1} corresponds to silk I conformation. This demonstrates high rate of silk I degradation and low rate of silk II degradation initially. In Figure 5.20 (c), it is observed three peaks (after 24 h of treatment) such as 1670, 1605 and 1510 cm^{-1}. The peak at 1605 cm^{-1} (Figure 5.15) corresponds to accumulation of fragments with high tyrosine content and other bulky amino acids and 1670 cm^{-1} indicating small turns in degraded fragments [176]. The peak at 1510 cm^{-1} corresponds to the presence of silk II secondary structure. This depicts the initial degradation of non-crystalline silk I and amorphous portions of SF nanofiber. The silk II crystalline fragments are observed even after 24 h of enzymatic degradation, however their intensity is less. Similar finding have been reported by Kaplan et.al in silk film of *B. mori* [125].

From the study, it can be observed that during the initial period, β crystalline fragments are separated due to enzymatic degradation of amorphous content. Accumulation of fragments containing bulky side chain occurs after initial period of digestion. The solubility of crystalline fragments occur which may decrease the rate of degradation of crystalline content after fragment separation.

XRD

XRD was performed to further assess any conformational or phase change occurred in SF scaffolds during enzyme degradation. XRD (Figure 5.21) indicates the change in degree of crystallinity and also the change of α and β fragments after enzymatic action for certain time period i.e. 0, 12 and 24 h. Figure 5.21 shows a prominent peak at 20.55^0, d = 4.387 Å which corresponds to α helix that gets reduced after 12 h of treatment. A prominent peak at $2\theta = 29.54^0$, d = 3.123 Å is observed after 12 h of study which is also present in the rudimentary form.

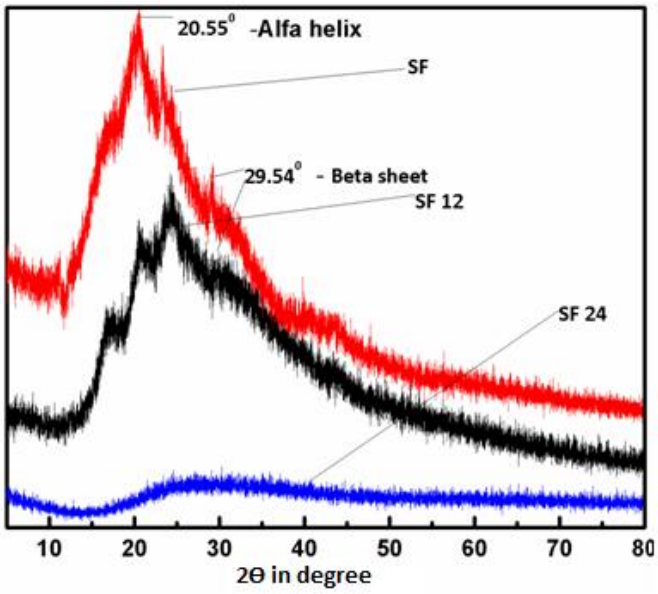

Figure 5.21: XRD analysis of degraded SF blend nanofibrous mat that was cultivated in protease XIV solution for (a) 0 (b) 12 and (c) 24 h.

This indicates increase in β sheet content after 12 h because of the digestion of α fragments and amorphous materials. The crystallinity of nanofibrous structure increases because of the dissolution of amorphous content of polymer, thus increasing the percentage of crystallinity. It is possible that this dissolution of amorphous content provide energy for recrystallization of certain

fragments. The 3rd curve (blue curve) in Figure 5.21 (c) indicates the decrease in crystalline and amorphous fragments at the same rate and no peaks are observed after 24 h of treatment except a broad hump demonstrating irregular crystalline fragments of SF nanofibers. The above phenomenon further supports that initial enzymatic degradation occur at α coils and amorphous structure.

DSC

DSC was performed to understand the interaction between bound water and hydrophilic amino acid present in the SF nanofibers. The endothermic peak of Figure 5.22 indicates Tg (1) (lower glass transition temperature) of SF nanofiber and its degraded product are within 50-70^{0}C range.

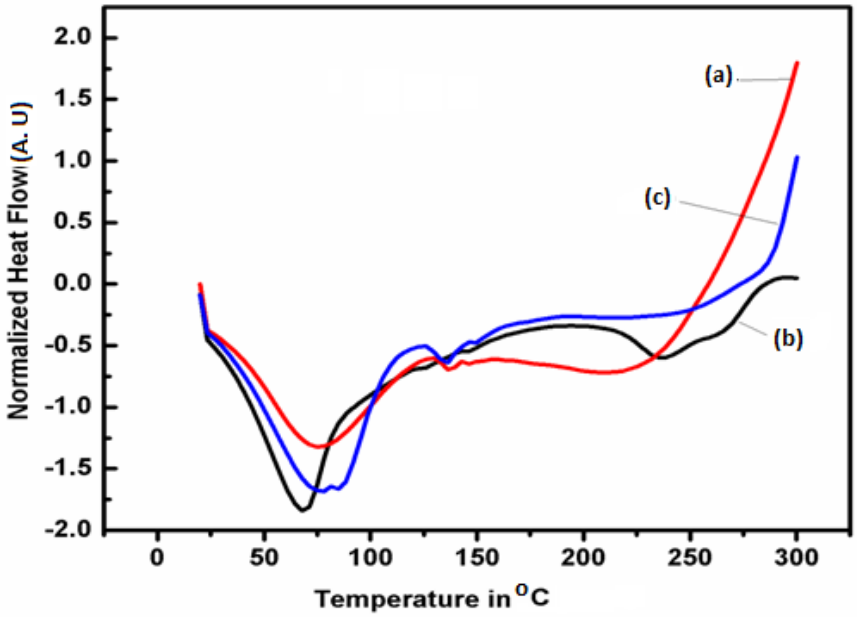

Figure 5.22: DSC analysis of degraded SF blend (eri-tasar) nanofibrous mat cultivated in protease XIV solution for (a) 0 (b) 12 and (c) 24 h

This demonstrated the presence of bound water and its interaction with hydrophilic amino acid in SF nanofiber and its degraded products [177]. This prompted its further analysis about the mechanism of degradation and factors affecting it.

TM-DSC

The glass transition temperature of nanofibrous mat after 0, 12 and 24 h of degradation are shown in Figure 5.23.

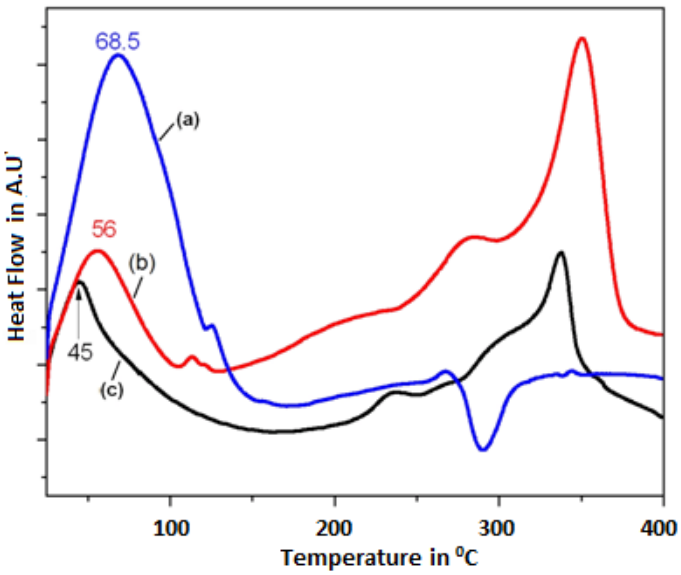

Figure 5.23: TM-DSC plot of degraded SF blend (eri-tasar) scaffold that was cultivated in protease XIV solution for (a) 0 (b) 12, and (c) 24 h

It shows that Tg (1) for nanofibrous mat and its degraded mat after 12 and 24 h are found to be 68.5^0C, 56^0C and 45^0C respectively. SF nanofiber can be considered as semicrystalline system of SF protein and water. Tg of such a protein-water system in presence of small amount of non-freezing bound water and protein with high amino acid content is markedly affected because of the breaking of intermolecular H bonding [178]. Thus a decrease in Tg value with respect to progress of enzymatic degradation reaction is noticed after 12 and 24 h. This further supports the presence of high hydrophilic amino acid content in nanofibers. In contrast, the sample whose major constituents are hydrophobic amino acid groups, Tg maintains a constant value regardless of water content due to lack of intermolecular H-bonding. The stabilization of hydrophobic groups by higher order structures is found in β sheet conformation [179]. This study suggests that hydrolysis of SF nanofiber continued throughout 24 h.

TM-DSC (Cp)

Figure 5.24 shows specific heat capacity (Cp) for SF nanofiber at Tg (1) for the sample treated with enzyme for 0, 12 and 24 h. The nanofibrous mat shows highest Cp value as compared to the rest two degraded products as expected. In contrast, the observed Cp value for sample treated

with enzyme for 12 h are lower than that of sample treated for 24 h. This ambiguity of Cp variation shows the influence of some other parameters in this degradation processes.

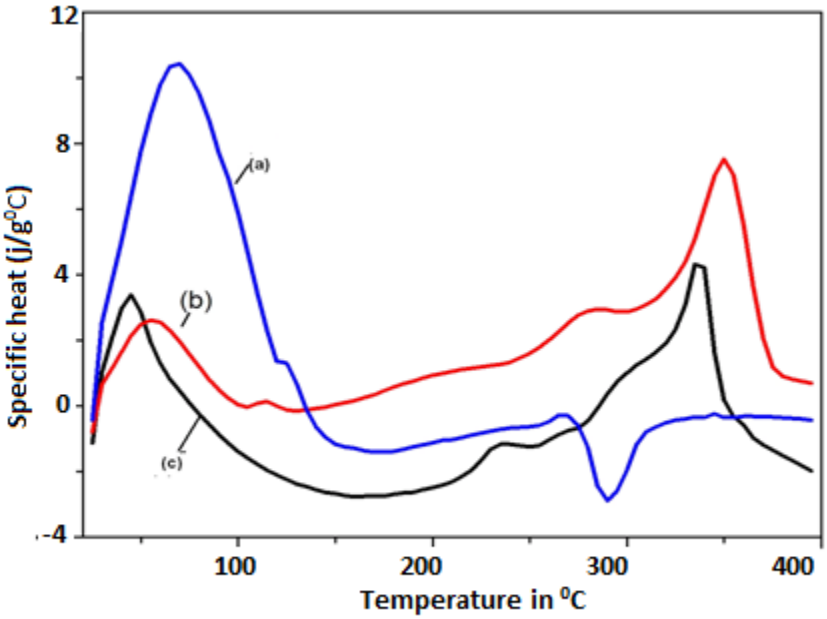

Figure 5.24: TM-DSC plot of degraded SF blend (eri-tasar) scaffold that was cultivated in protease XIV solution for (a) 0 (b) 12 and (c) 24 h.

The reduction in heat capacity of SF-bound water system is a result of hydration reaction progress which eliminates the hydrophilic amino acid content from nanofibrous sheet and its enzymatically degraded products [180]. The resulting fragments produced have high content of hydrophobic amino acid with low mobility owing to heavy hydration. The heat capacities of bound water indirectly affect the molecular mobility of polymeric chain in water under the effect of force field of fragments and dissolved solute particles. The decrease in molecular mobility of fragment in water is accompanied by a decrease in heat capacity of bound water [181] establishing a linear relationship between Cp and bound water [182] which explains the decrease in Cp value upon nanofibrous scaffold degradation. In contrary, a rise in heat capacity of SF fragment-water system is observed after 24 h of enzymatic degradation, though a fall in Tg is noticed. The reason may be because of interaction of tightly bound water to enzymatically degraded SF fragment causing decline in entropy of SF water system. But intermolecular conformational changes influence the mechanism of interaction of water molecules with silk

fibroin. Thus an unfavorable interaction with hydrophobic fragments and bound water cause denaturation of SF fragment due to destruction of ordered water cluster associated with the SF molecule inside the nanofiber which increases the heat capacity of fragments after 24 h [183].

5.2.3.4 Morphological study

Figure 5.25 shows the scanning electron micrograph of degraded nanofibrous scaffold after (a) 0 h (b) 6 h (c) 12 h (d,e) 24 h (f) 48 h respectively to see the change of morphology because of degradation. After 6 h of degradation, the core layer swollen globules with 200-800 nm in diameter which is still connected with undigested SF fragment (probably β sheet) in Figure 5.25 (b) are observed. The Figure 5.25 (c) demonstrates the deposition of heavy amount of salt and proteins in the degraded structure after 12 h. Thereafter, the α coil structure swells and degrades to form globular structures with radiating nanofilaments in Figure 5.25 (d) and (e) while β structures are immune to enzymatic degradation and visualized as radiating nanofilaments. After 48 h of enzyme treatment, irregular, swollen amorphous matrix is visible in Figure 5.25 (f).

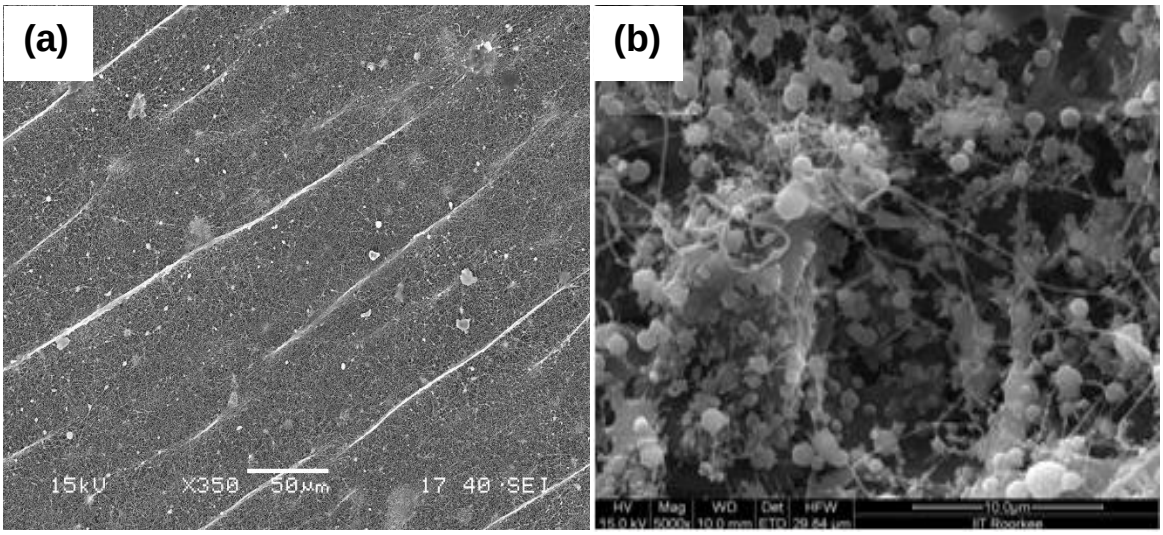

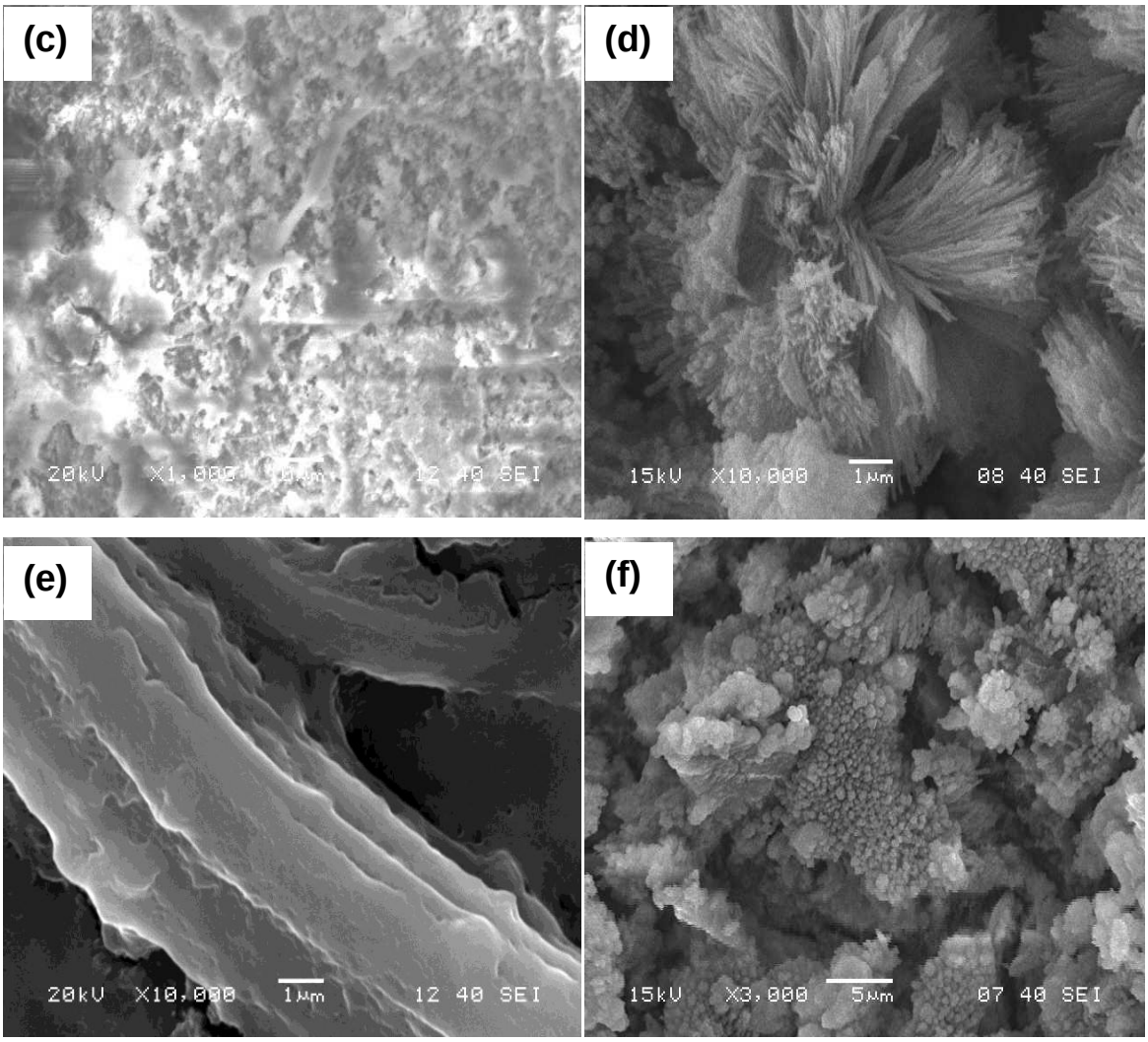

Figure 5.25: Surface and cross-sectional images of SF blend nanofiber mats after enzymatic treatment in SBF for (a) 0 h (b) 6 h (c) 12 h (d) and (e) 24 h and (f) 48 h.

Further surface morphology of nanofibrous mat were analyzed through atomic force microscope which are shown in Figure 5.26. Figure 5.26 (a) and (b) correspond to nanofibrous structure while (c) after 12 h of treatment shows deposited and fragmented particles over the scaffold surface. After 24 h of enzyme treatment, core nanofilaments were observed as seen in Figure 5.25 (d). Based on the above facts, it can be concluded the following facts. After 12 h of degradation, the nanofibrous structures are degraded with swelling and numerous globular agglomerated core structures of silk fibroin is visible. The nanofilaments are further observed with surrounded interconnecting nanofibrils after 24 h. The degraded particle agglomerate and

nanofilaments of fibers are observed through AFM. Similar observation is noticed by Kim et al. in his study [184].

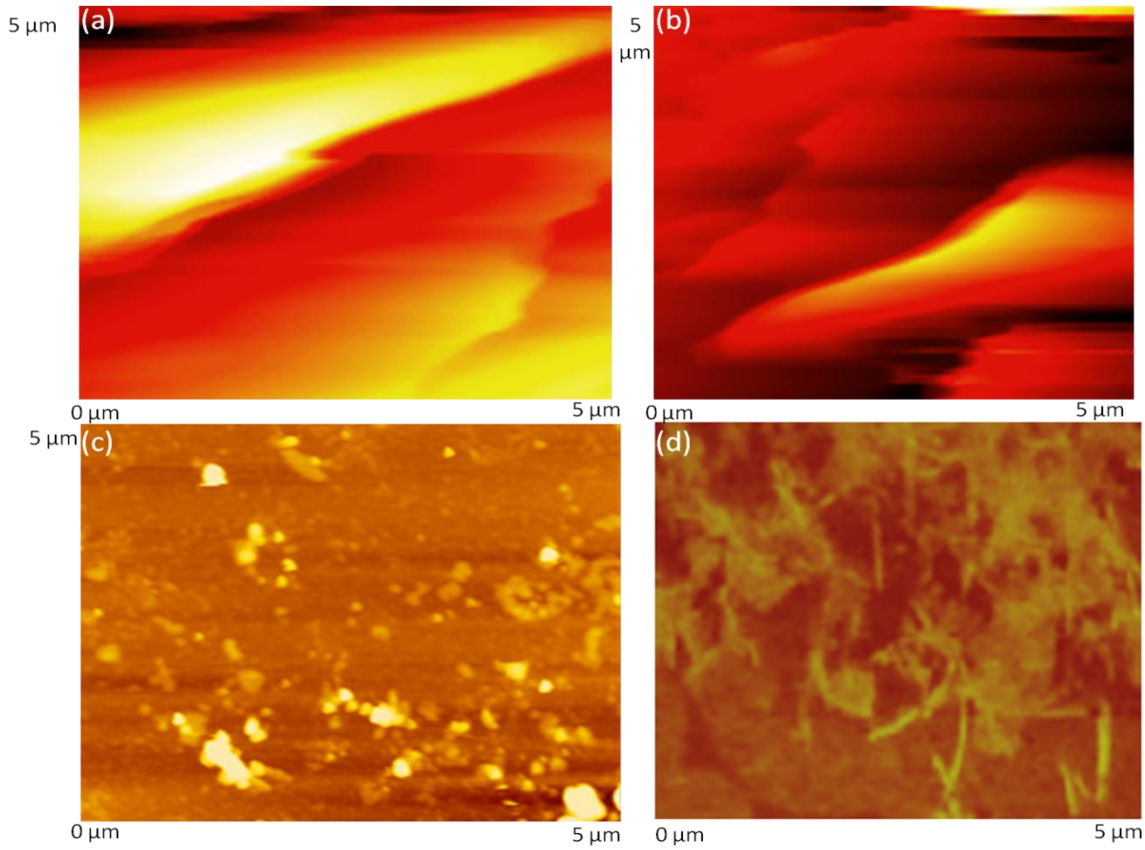

Figure 5.26: AFM images of degraded SF blend nanofibrous mat treated in protease XIV solution for (a) and (b) after 0 h (c) after 12 h and (d) after 24 h respectively.

5.2.3.5 Elucidation of mechanism

The degradation of high amount of non-crystal hydrophilic blocks make free the tiny hydrophobic crystal blocks which moves away without being degraded. Similar predictions are done in silk film biodegradation study by Kaplan et al [125] . However, the degradation may be more favorable than the SF *of B. mori* because of the presence of hydrophilic amino acid containing bulky side group providing more defects in semi-crystalline fibers. Thus the decrease in crystallinity of fiber is either by dissolution or migrations of hydrophobic nanostructure rather than degradation as these structures are immune to enzymes comparatively. Moreover, the high

porosity and surface area of the nanofibrous scaffold provides higher rate of enzyme action demonstrating faster degradation kinetics.

Our result supports the previous report that hydrophilicity accelerates SF fragmentation and biodegradation [185]. The non-crystal and silk I structure degrade more quickly to separate the silk II content after 12 h of protease treatment in solution. Thus the increase in β content/silk II conformation increases the resistance to degradation by enzyme. Thereafter, further degradation of silk I present along with β structure is accelerated because of the enhanced surface area of fragments which allows penetration of water molecules containing enzyme causing chain separation. The entry of water molecules into the fragments of SF nanofibers creates ion-dipole interaction with negative charge of SF protein and thereby decreases inter/intra molecular friction between the chains and increase their mobility and separation. This has been attributed by decrease in crystallinity of nanofibrous structure as observed in Figure 5.26 (c). This fragmentation process further shortens the silk II crystal fragments which are removed either by solubilization or by migration from the site through solvent flow. Thus a fall in concentration of silk I and silk II occurs simultaneously after 12 h resulting in decrease in both silk I and silk II content after 24 h. The solution after 24 h of degradation has been filled with nanofilaments and particles with 10-100 nm in diameters (Figure 5.26 (d)).

Our study is silent regarding the role of continuity, polydispersity of fibers and presence of bending in coils which are important factors in determining the action of enzymes on SF nanofibrous sheet. Nevertheless, these factors hold minimum significance in elucidating basic mechanism of SF blend nanofibrous degradation processes because of its major dependence on hydrophilicity, β sheet structure and crystal-non crystal content. The efficiency of proteosomal degradation in eri-tasar blend is expected to decrease after 12 h because of substrate unfolding caused by alternate repeat of glycine and alanine [186]. This has been supported by our study which showed 18-19% degradation during initial 12 h of enzyme treatment, followed by 7-8 % of degradation in next 12 h (Figure 5.26 (c and d)). On the other hand, high Asparagin content along with higher amount of Asp-Gly dipeptide sequence in eri-tasar blend is likely to promote faster hydrolysis and deamidation reaction initially to form cyclic imide intermediate with the cleavage of peptide chain accelerating biodegradation [187]. The above mechanism requires further study to determine the detailed molecular mechanism to modulate degradation behavior.

Additionally, the faster degradation of scaffold induces formation of higher osteogenic extra cellular matrix as suggested by Park et al [188].

5.2.4 In vitro cell culture study

5.2.4.1. Characterization of hMSCs

Cultured hMSCs up to 4th passage was used for cell culture study to examine the cell supportive property of the developed scaffold. The morphological characterization of hMSCs was done by phase contrast microscopy, the images of which are shown in Figure 5.27. The cells are found to be MSCs as evident from their fibroblast-like cell morphology.

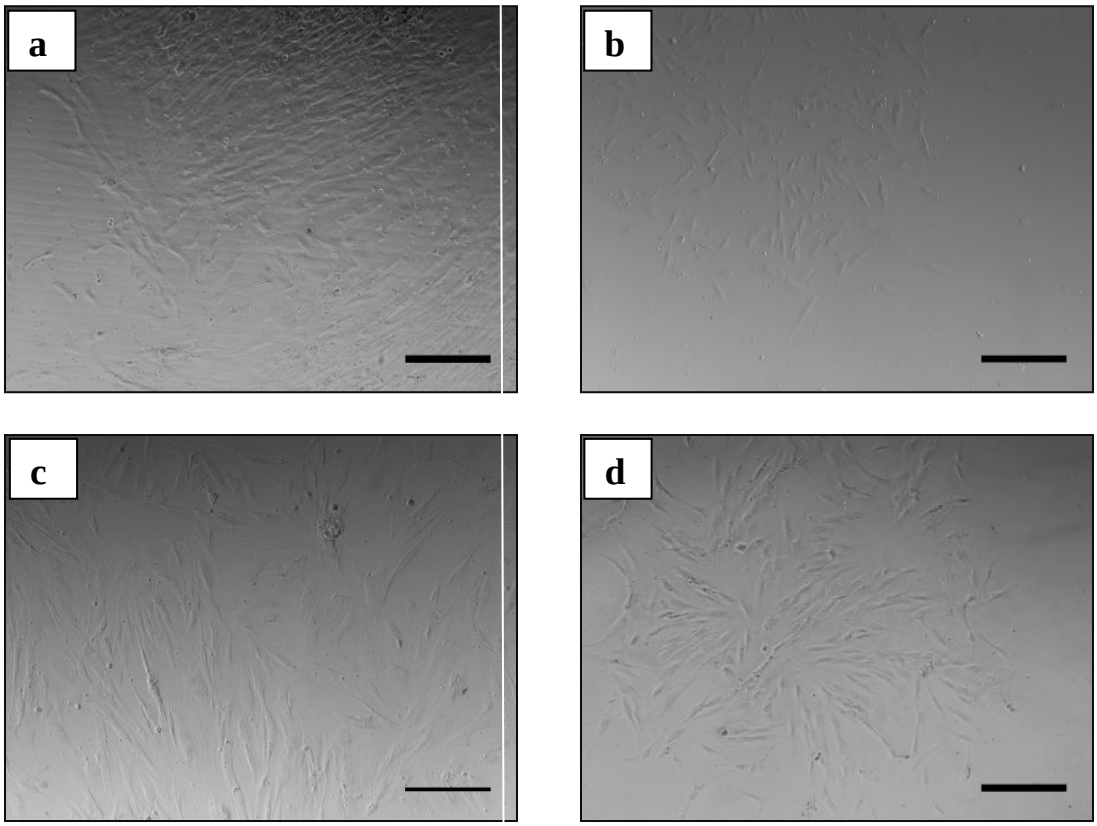

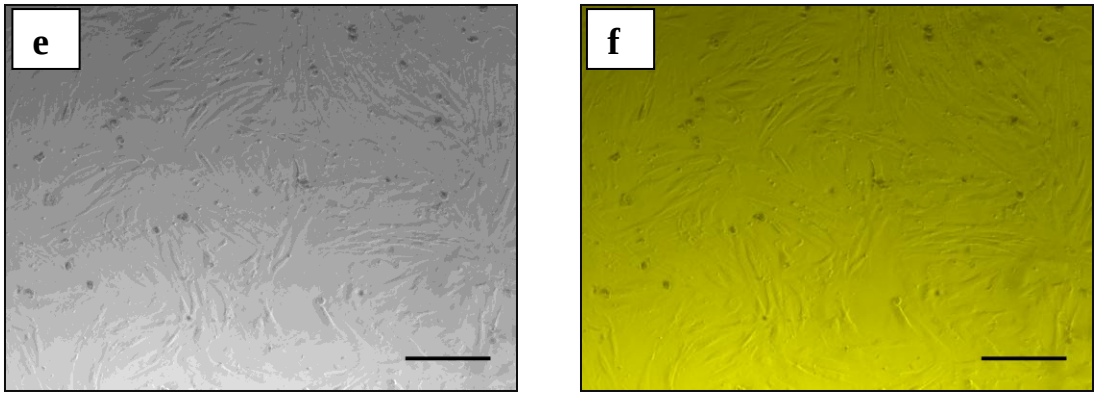

Figure 5.27: Morphological observation of hMSCs under phase contrast microscope at magnification 5X (a) day 1 (b) day 2 (c) day 3 (d) day 5 (e) day 7 (f) day 14 of 4th passage

Further, the immunophenotypic characterization of hMSCs was studied by flow cytometry analysis. The immunophenotypic characterizations are shown to be positive for CD90 (99.01%), CD73 (95.5%) and CD105 (96.5%) expression and negative for CD34 (1.0%), CD45 (0.5%), and HLA-DR (1.2%) indicating the cells are MSCs. Immnuofluorescence also found to express CD90, and CD105, but not the hematopoietic origin marker CD34 as shown in Figure 5.28.

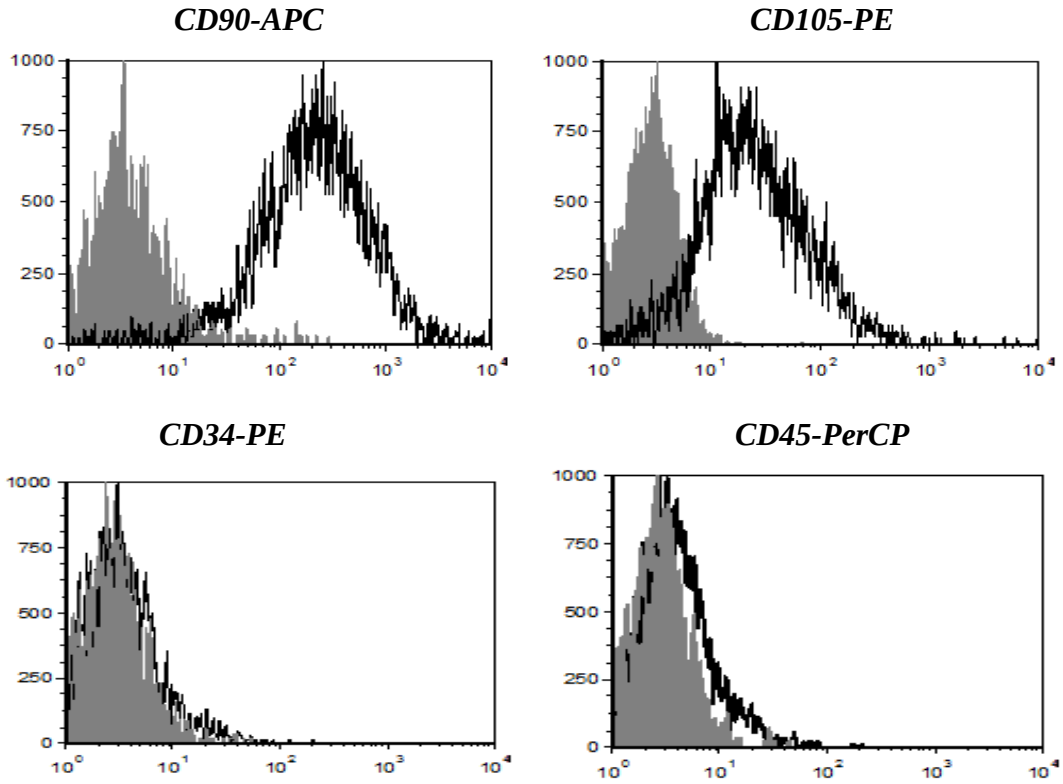

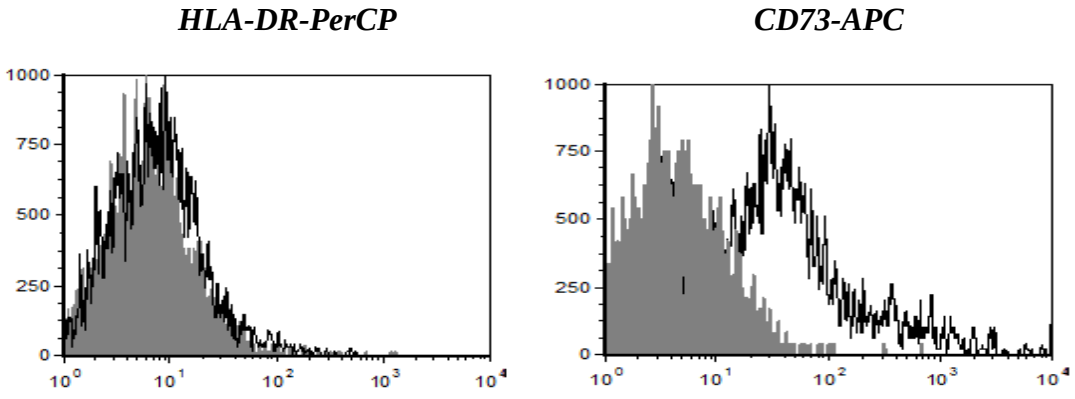

Figure 5.28: Flow cytometric analysis for the expression of MSCs markers CD90, CD105, CD73 (+ve markers) and hematopoietic CD34, HLA-DR and CD45 (-ve markers) markers

5.2.4.2 Cell morphology and spreading

After seeding the cells are rounded in shape and scattered throughout the nanofibrous mat (Figure 5.29 (a) and (b)). But after 24 h, hMSCs are elongated with spread morphology and observed in colony (Figure 5.29 (c) and (d)). The spread morphology indicates the active cell proliferative potential of MSCs over nanofibrous scaffold.

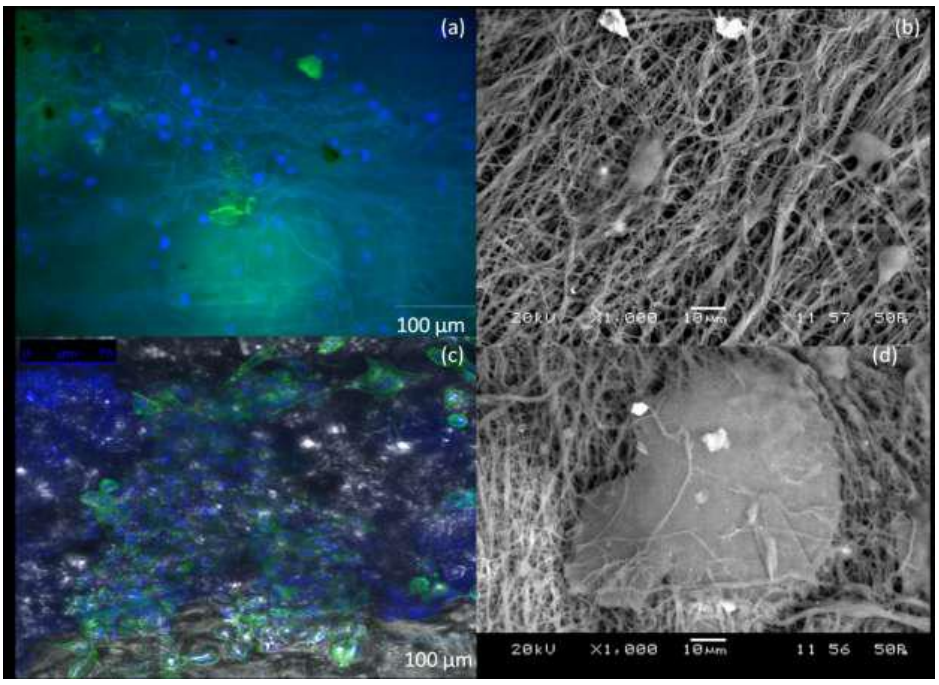

Figure 5.29: Temporal evaluation of hMSCs spreading on electrospun SF blend nanofibrous scaffolds (a) and (b) after 1 h (c) and (d) after 24 h of cell spreading by confocal and SEM analysis

5.2.4.3 Metabolic activity of MSCs

The metabolic activity of MSCs on the scaffolds were examined qualitatively by fluorescence study and further quantified by MTT assay. Figure 5.30 (a-c) demonstrates the relative cellular metabolic activity of MSCs grown over *B. mori*, gelatin and SF blend scaffold under fluorescent microscopy after 3 days of culture using CMFDA dye. This is an excellent method for morphological observation of cellular viability and cytotoxicity. The overall signal in the field of observation was measured and the fluorescence intensity per cell was determined. It was observed that the cells proliferate in an increasing order over gelatin, *B. mori* and eri-tasar scaffold. However, cells grown over *B. mori* scaffold have a lower metabolic activity as the CMFDA signal per cell appears weaker than followed by gelatin and eri-tasar scaffold. This is in good agreement with the previous observation reported by Patra et al. in case of porous tasar (*Antheraea mylitta*) SF scaffold [189].

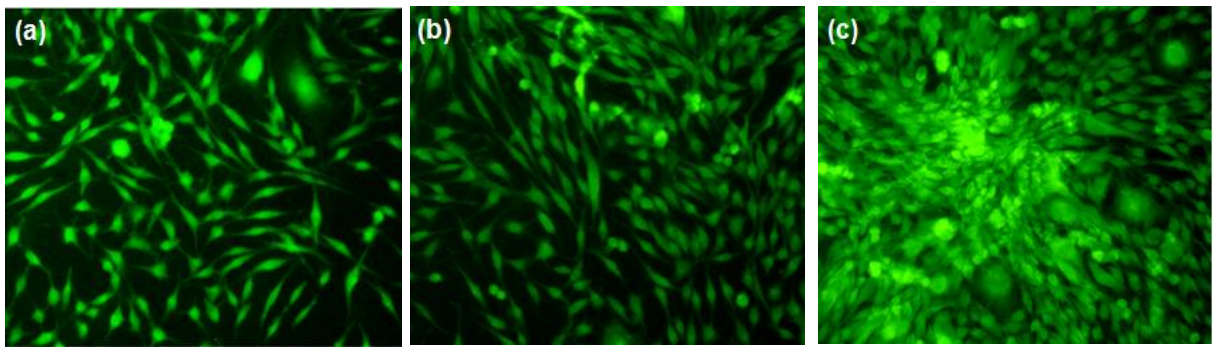

Figure 5.30: Fluorescence image using CMFDA dye showing the cell viability after 9 days on (a) B. mori (b) gelatin (c) SF blend (eri-tasar)

A quantitative analysis of the metabolic activity of MSCs was assessed by MTT assay by culturing MSCs on gelatin, *B. mori* and eri-tasar nanofibrous scaffold. Figure 5.31 shows the relative cellular metabolic activity of MSCs after 3, 6, 9 days of culture. It has been observed that cellular metabolic activity is significantly higher in case of eri-tasar followed by gelatin and then *B. mori* scaffold. Thus both qualitative and quantitative observation confirmed that the cells grown over eri-tasar scaffold are metabolically superior to that of *B. mori* and gelatin scaffolds.

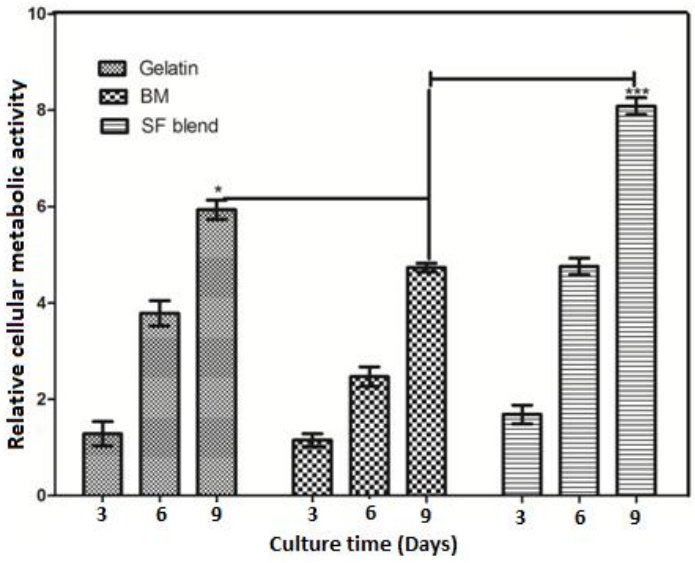

Figure 5.31: MTT assay of SF blend, gelatin and B. mori nanofibrous scaffold after 3, 6, 9 days of culture.

5.2.4.4 Cell proliferation

Cell proliferation is the increase in number of MSCs because of cell growth and cell division. It is also a sensitive indicator of cellular stress as it requires intact cell structure and function. Further, the maintenance of undifferentiated proliferated cells depict that hMSCs produce adequate growth factors and adhesion molecules for its maintenance in scaffold [190].

SEM

SEM study was performed to assess the proliferation of hMSCs on the nanofibrous *B. mori* and eri-tasar scaffolds qualitatively by culturing MSCs for 7 and 14 days. The SEM images are shown in Figure 5.32 a (BM) & b(ET) and Figure c (BM) & d(ET) for 7 and 14days of culture respectively. Both scaffolds have shown to promote cellular proliferation as it is indicated by the well spreading of the cells over the scaffolds and aggregation of spindle shaped cells. The fibers are found to remain intact and initiation of mineralization is observed after 14 days. However, higher number of proliferated cells is observed with eri-tasar representing better cell supportive property of eri-tasar.

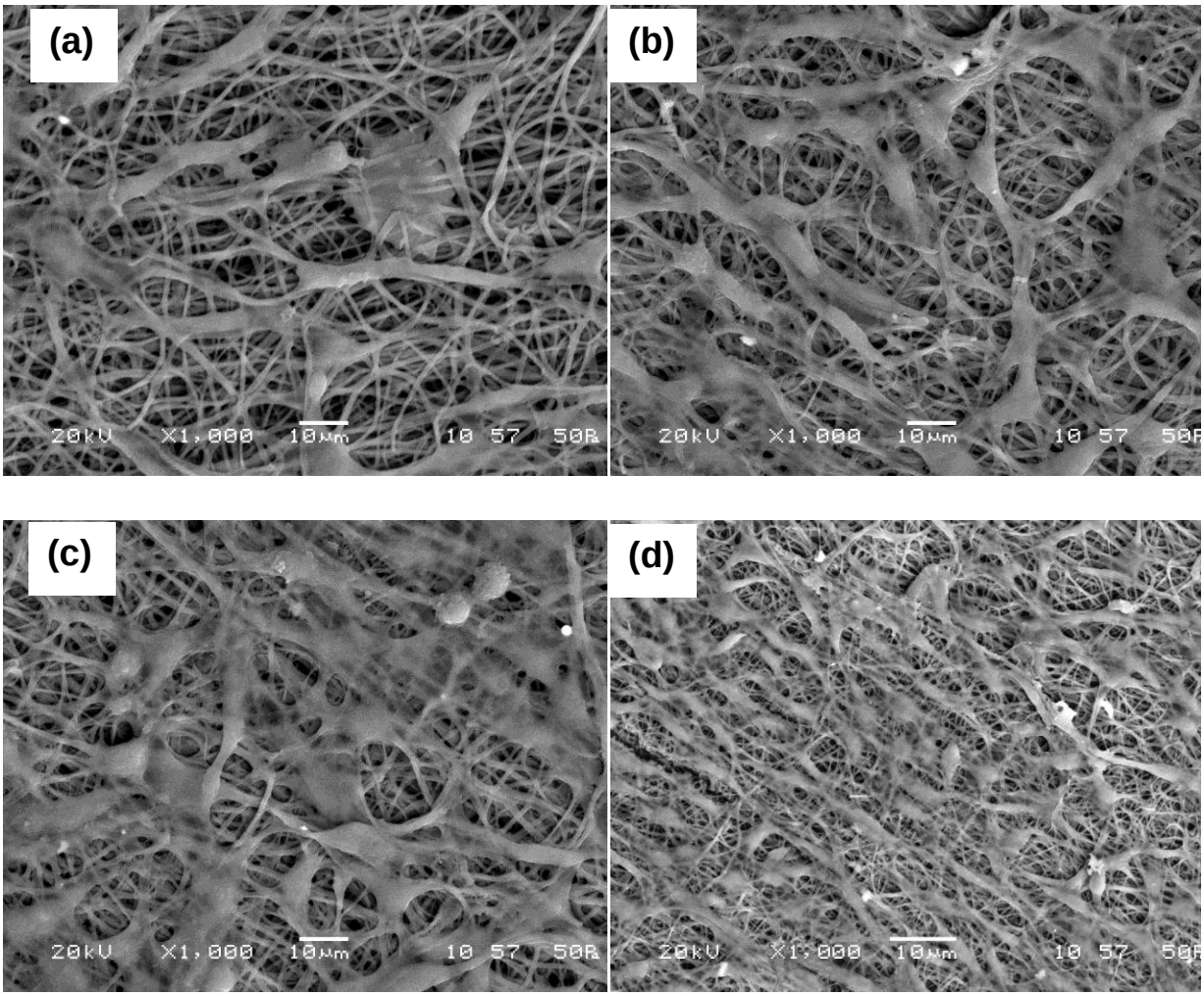

Figure 5.32: SEM images showing proliferation of MSCs after 7 and 14 days of culture over SF blend (ET) and BM scaffolds

DNA content estimation

Further, a quantitative measurement of cell proliferation on the scaffolds was done by estimation of DNA content. The DNA content in MSCs was compared with the MSCs grown over *B. mori* and gelatin (as negative control) scaffolds. The result of MSCs proliferation after 7, 14 and 21 days of cell culture is shown in Figure 5.33. It is observed that the rate of proliferation increases (increased DNA content) with time up to 21 days for all the cases. However, the rate was faster for the first 14 days representing the log phase and then a decline in rate is observed. The rate of proliferation of MSCs follows the trend eri-tasar > *B. mori* > gelatin for all the days of culture under study.

The percentage increase in rate of proliferation from day 7-21 on gelatin, *B. mori* and eri-tasar are 82%, 128% and 135% respectively whereas an increase in rate is found to be 4%, 6% and 9% from day 14-21. Furthermore, the amount of isolated DNA obtained with eri-tasar is 13% more than that of *B. mori* after 21 days. The high proliferation over eri-tasar nanofibrous scaffold than *B. mori* may be explained due to proper initiation of cell-scaffold interaction [191]. This study demonstrates that the superiority of eri-tasar over other scaffolds in terms of cell viability and proliferation ability of MSCs on the scaffolds.

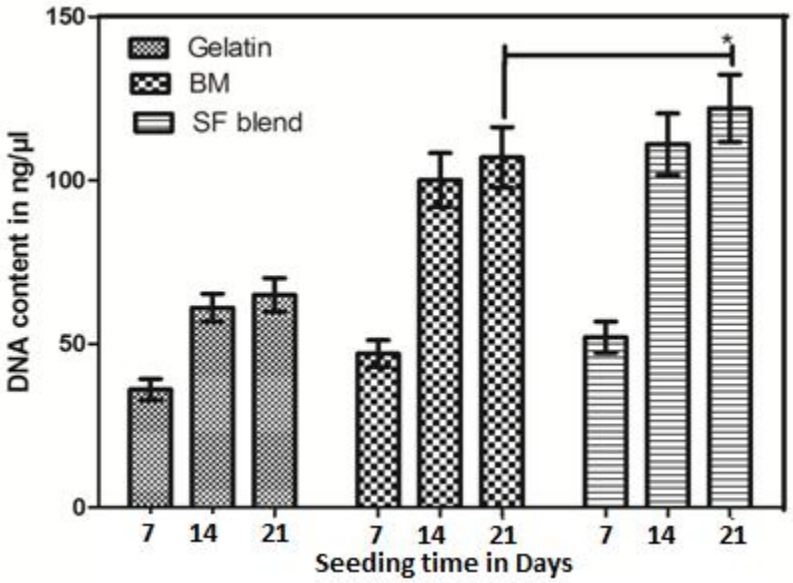

Figure 5.33: Rate of cellular proliferation in terms of DNA content estimation

5.2.4.5 Cell adhesion

Cell adhesive property is one of the most important criteria for selecting material to engineer tissue. Therefore in the present section, the cell adhesion property of eri-tasar scaffolds was assessed by confocal, TEM and flow cytometry analysis for cell attachment, expression of cell adhesive molecules (CD44 and CD29) and development of cellular outgrowth similar to lamellopodia.

Cell attachment

Nanofibrous scaffold prepared from gelatin is used as a negative control *in vitro* because of its poor adhesive property towards MSCs. The cell adhesion property was also compared with *B. mori* and gelatin scaffold. Passage 4 MSCs were allowed to attach for 12 h and 48 h on the

scaffold and then cell attachment on the scaffolds was evaluated by confocal microscopy. The cytoskeleton organization of the MSCs was demonstrated by phalloidin staining of the F-actin, counterstained with DAPI (nuclei) in Figure 5.34. Figure 5.34 (a, c, e) shows the distribution of MSCs after 12 h over gelatin, *B. mori* and eri-tasar scaffold. It was observed that the MSCs are scattered and feebly distributed over gelatin scaffold. *B. mori* shows comparatively more number of attached MSCs while maximum numbers of attached cells are observed on eri-tasar scaffold. The MSCs on gelatin scaffold has shown rounded morphology and less spreading nature even after 48 h. While that of *B. mori* and eri-tasar has elongated and well spreading in nature. They are observed to produce stress fiber like cytoskeleton after 12 h of post seeding (as observed through actin cytoskeleton orientation) and extensive cell-cell interaction and aggregation are observed after 48 h (d, f). MSCs over gelatin scaffold are without spread morphology and fail to stain strongly with phalloidin indicating lack of adequate actin polymerization even after 48 h (Figure 5.34 (b)). The few cells attached to gelatin scaffold surface were elongated and F-actin visible on its surface which indicate regional stress fibers. In contrast, after 48 h the MSCs over *B. mori* shows better polymerization of actin filament while over eri-tasar adequate and prominent polymerized actin has been observed. Thus the cell attachment property of MSCs follow the trend eri-tasar > *B. mori* > Gelatin.

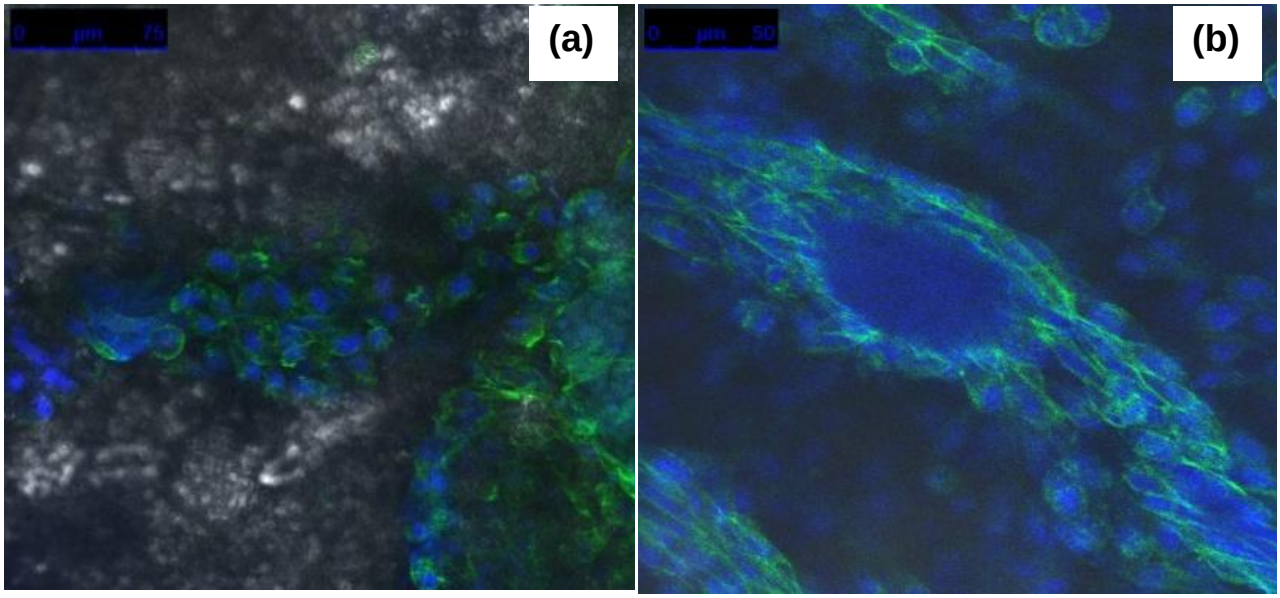

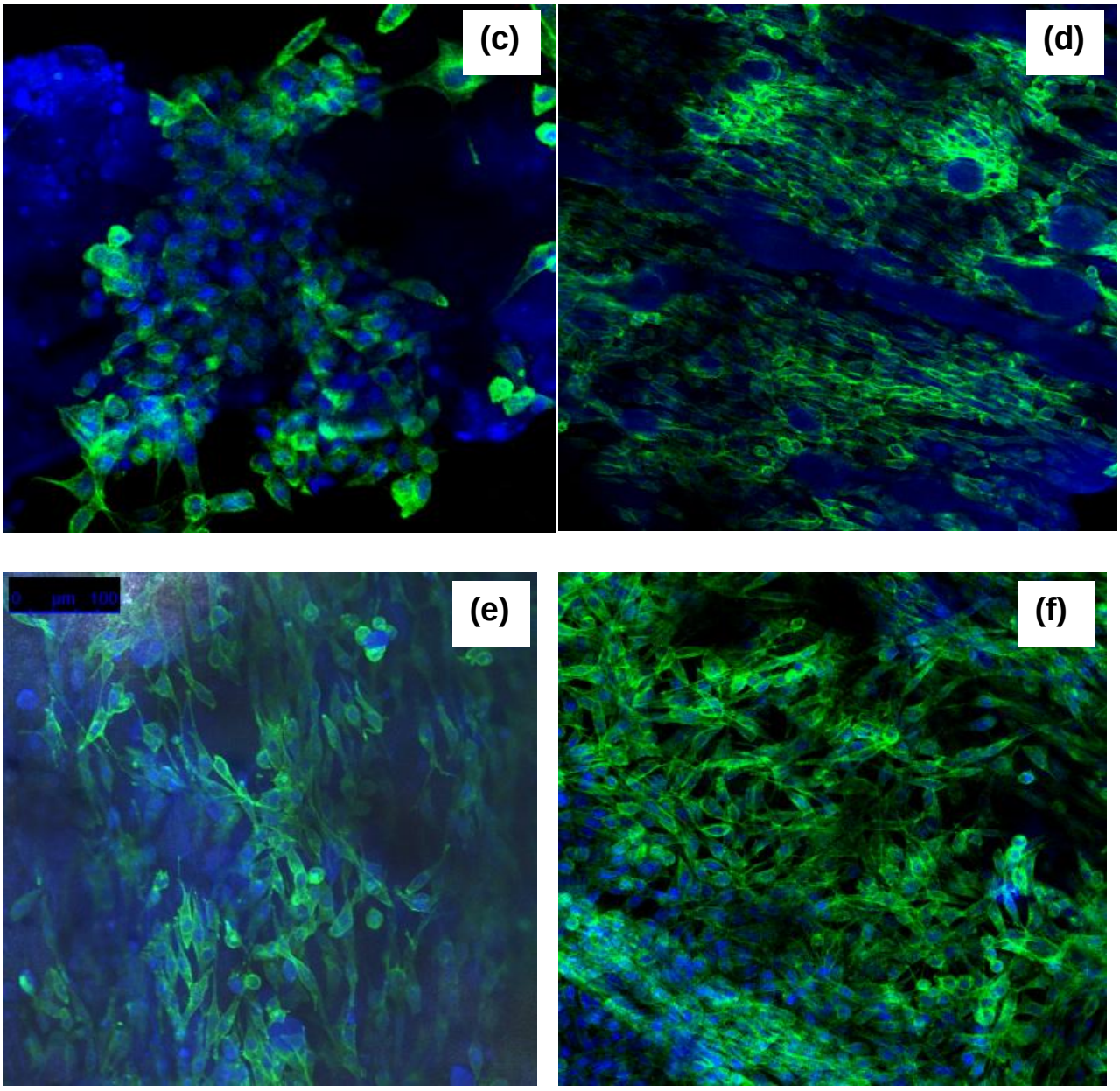

Figure 5.34: Confocal microscopic images showing the attachment of MSCs after 12 and 48 h of seeding on gelatin (a, b), B. mori (c, d) and SF blend (eri-tasar) (e, f) respectively. MSCs cultures were stained for β actin (green) and DAPI (nuclei, blue). Scale bar: 100 µm.

As indicated in Figure 5.35, the numbers of attached cells over eri-tasar are significantly higher than those of *B. mori* while gelatin shows poor cell attachment.

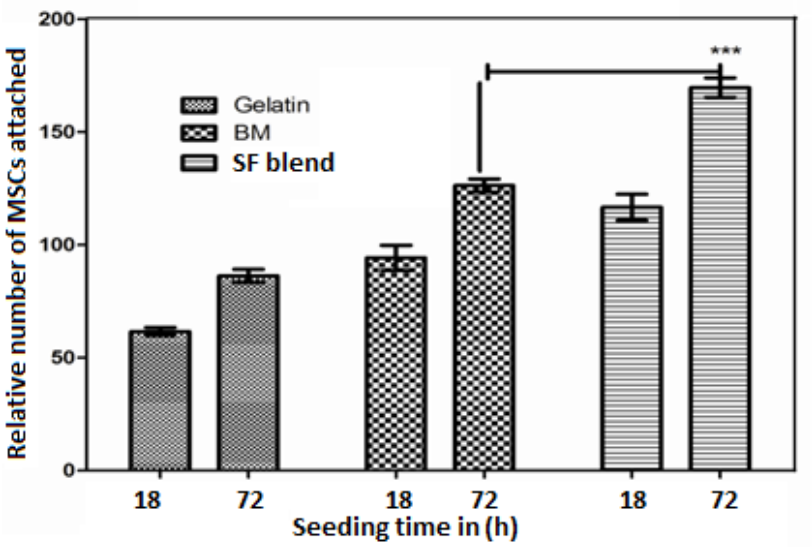

Figure 5.35: Quantitative estimation of MSCs attachment on gelatin, BM and ET scaffold.

The enhanced cell attachment over eri-tasar may be attributed to high surface irregularity, roughness (observed through TEM micrograph of nanofibrous structure (Figure 5.9)) as well as presence of RGD epitope.

Furthermore, it is a well-established fact that the adhesion of MSCs in a suitable matrix environment occurs through a network of dynamic contractile machinery which facilitates cellular motility with the formation of cell protrusions [192,193]. Figure 5.36 (a-e) showed the prominent development of outgrowths and cell processes similar to lamellopodia and figure 5.36 (f) confirms the formation of lamellopodia through immunofluorescence study in eri-tasar scaffold. These structures are reported to be essential for cell spreading, *in vitro* polarization and acknowledged to participate in an active ongoing process such as absorption, adhesion, secretion, mechanotransduction as well as adaptation of MSCs to surrounding eri-tasar scaffold [194].

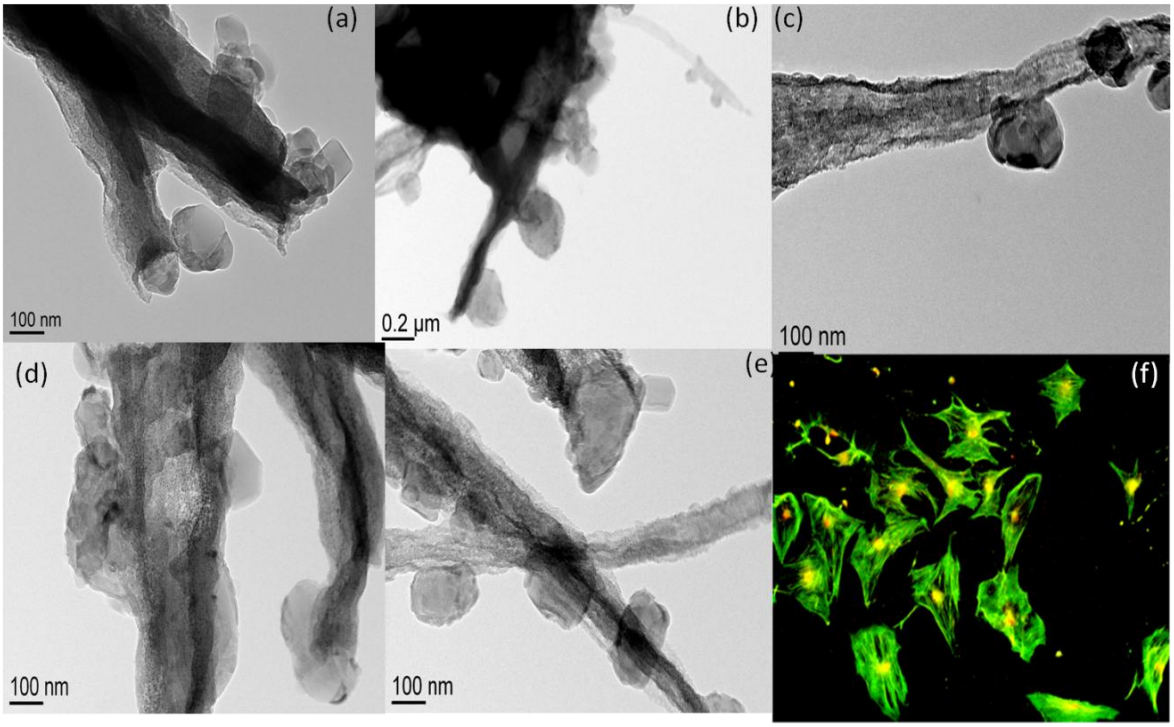

Figure 5.36: TEM images showing the development of cellular outgrowth over SF blend nanofibrous scaffold confirming cell adhesion after 12 h of cell seeding.

Expression of CD44 and Integrin beta 1

MSCs express adhesion molecules or transmembrane receptors such as hyaluronan (CD44) and Integrin beta 1 (CD29) in context to their extracellular microenvironment. They are liable for signal transduction and modulate interaction between F-actin in cytoskeleton and components of ECM [195,196]. Figure 5.37 shows the immune fluorescence analysis of expression of CD44 and integrin beta 1 on MSCs grown over SF blend nanofibrous mat. These transmembrane receptors are clearly visible over the membrane as green fluorescence. The quantitative degrees of expression of hyaluronan and integrin beta 1 were estimated through FACS as observed in Figure 5.37 (a) and (b). The study demonstrates a substantially higher amount of integrin beta 1 and CD44 expressions over MSCs cultured on eri-tasar nanofibrous mat after 24 h of cell seeding. The expression of above receptors are lower in *B. mori* while gelatin shows minimum expression (-ve control) and fibronectin shows (+ve control) maximum expression of the above markers.

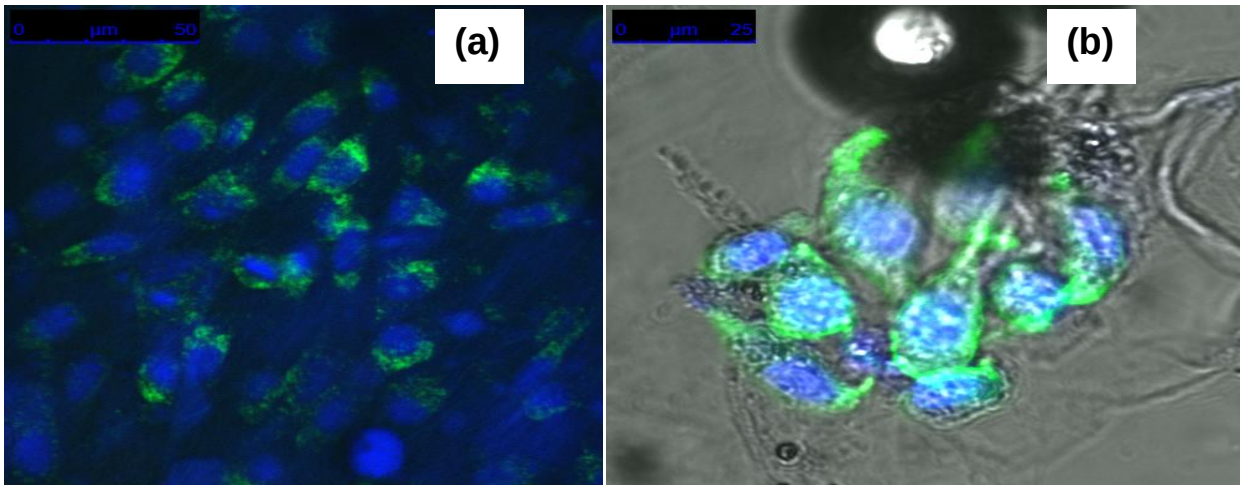

Figure 5.37: Expression of CD29 (anti-integrin beta 1 Immuno fluorescence) and CD44 (hyaluronane receptors) after 24 h of MSCs seeding onto SFnanofibrous scaffold as observed under Confocal microscope.

These receptors are also reported to act as mechanotransducers to detect change in matrix variation and polarize MSCs towards growth, proliferation, morphogenesis, integrated cellular response, wound healing and differentiation allowing aggregation of proteoglycans [38,39]. Additionally, focal adhesions which is an essential step for the structural linkage between ECM and cytoskeleton with the formation of stress fibers [197] involves beta 1 integrin engagement and recruitment of protein for stabilization of actin cytoskeleton [198]. Furthermore, CD44 promotes integrin activation as well as bind to extra-cellular hyaluronic acid that exhibits various biological functions such as cell adhesion, matrix assembly, endocytosis, and cell signaling [199].

As it is observed in figure, the higher expression of adhesion molecules such as CD44 and beta 1 integrin over SF blend eri-tasar nanofibrous scaffold (Figure 5.38) ensures enhanced adhesiveness and proliferation functionality of MSCs which implicated the survivability of tissue graft by reducing the inflammatory reaction and immune activation at the site of injury [200]. Thus it reduces the use of immunosuppressant and anti-inflammatory drugs. Proper adhesiveness of tissue graft with surrounding tissue reduces the chance of scar tissue formation (internal scar tissue are very difficult to remove) and increases the colony forming activity of MSCs so that survival rate and efficiency of natural tissue regeneration is likely to be enhanced.

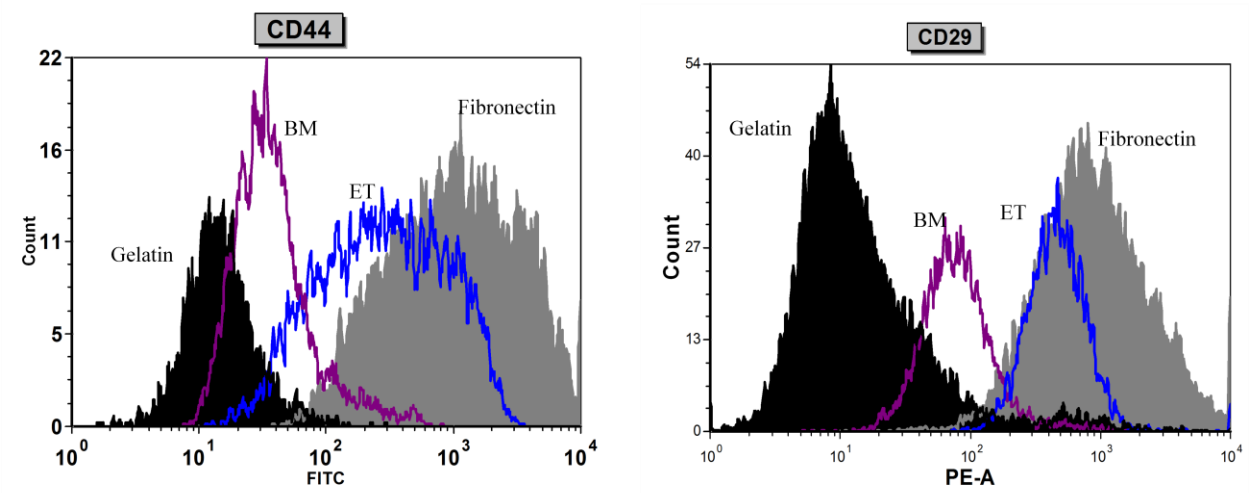

Figure 5.38: Flow cytometry analysis for quantitative expression of (a) CD44 and (b) CD29 of MSCs over nanofibrous scaffold after 24 h of seeding

5.2.3.6 Osteogenic differentiation

ALP activity of hMSCs on SF scaffolds

ALP cleaves organic phosphate ester and is a key component which has a role in the formation of apatite CaP [201]. It is an early indicator of immature osteoblast activity with a commitment to osteoblast phenotype [202]. ALP activity of hMSCs on the nanofibrous scaffolds such as gelatin, *B. mori*, and eri-tasar have been observed on 7, 14 and 21 days of culture in osteogenic media and the data are plotted in Figure 5.39. The figure indicates substantially higher amounts of ALP on eri-tasar after 14 days of MSCs culture which steadily increases towards 21 days. Elevated levels of ALP are observed during the initial phase of mineralization i.e. about 14 days of culture [203]. The ALP activity is significantly higher ($p<0.01$) on eri-tasar SF blend (ET) scaffold as compared to *B. mori* on day 7, 14, 21.

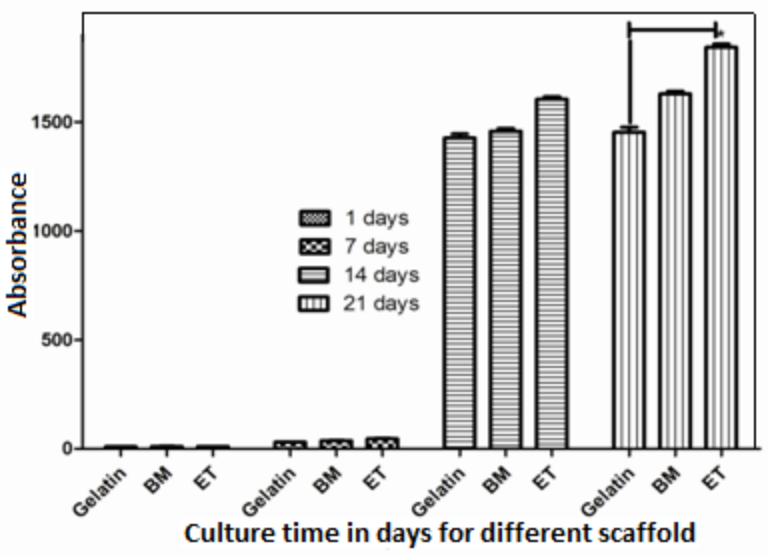

Figure 5.39: Expression of ALP with respect to culture time and type of scaffold

Glycosaminoglycan (GAG) estimation

The GAG production is an indication of differentiation towards a specific lineage. The three types of scaffolds (gelatin, *B. mori* and eri-tasar) studied show small amounts of secreted GAG into the scaffold and medium even after 28 days (Figure 5.40). The difference in GAG secretion between *B. mori* and eri-tasar scaffolds is statistically insignificant. GAG secretion is significantly low with gelatin after 28 days of culture in osteogenic media as compared to the other two. GAGs are a trivial component of organic bone ECM (less than 1%). They are thought to bind and accumulate a number of distinct proteins including growth factors and cytokines, improve and stabilize the presentation to their relevant receptors and protect them from proteolytic degradation [204, 205]. GAG deposition of 25 μg/0.6 cm^2 scaffold in MSCs seeded constructs containing osteodifferentiation media was higher than that of controls even after 28 days confirming the superior osteogenic potential of eri-tasar scaffold.

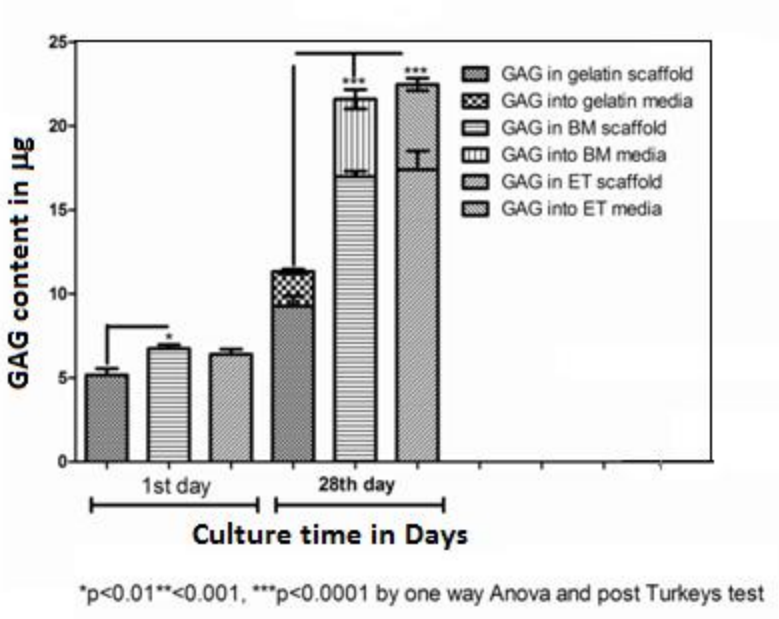

Figure 5.40: GAG assay through biochemical estimation (GAG deposited over scaffold + GAG secreted into media) on day 1 and 28 of culture in osteogenic media.

Mineralization of hMSCs on scaffolds

Figure 5.41 (a) corresponds to the image of HAp crystal attached to individual nanofiber after 28 days of osteogenic stimulation taken by HR-TEM. SEM images of the mineralized matrix upon osteogenic stimulation are shown in Figure 5.41 (b) and (c) whereas Figure 5.41 (d) provides the elemental analysis of the white crystal deposits by EDX which shows the Ca:P intensity ratio 1.6.

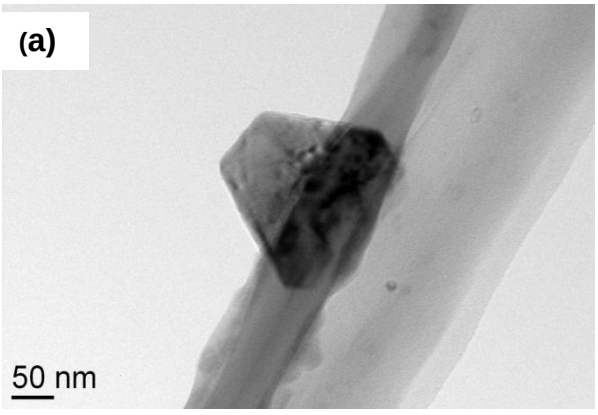

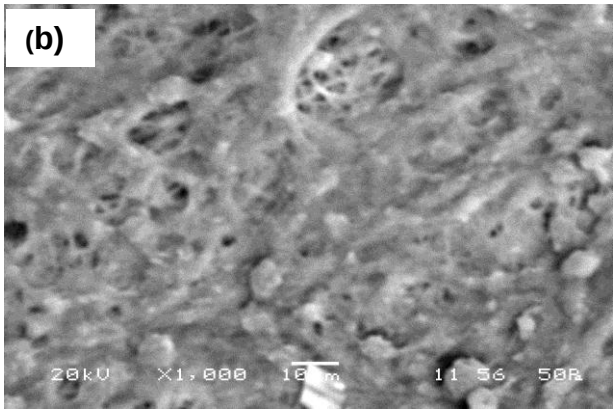

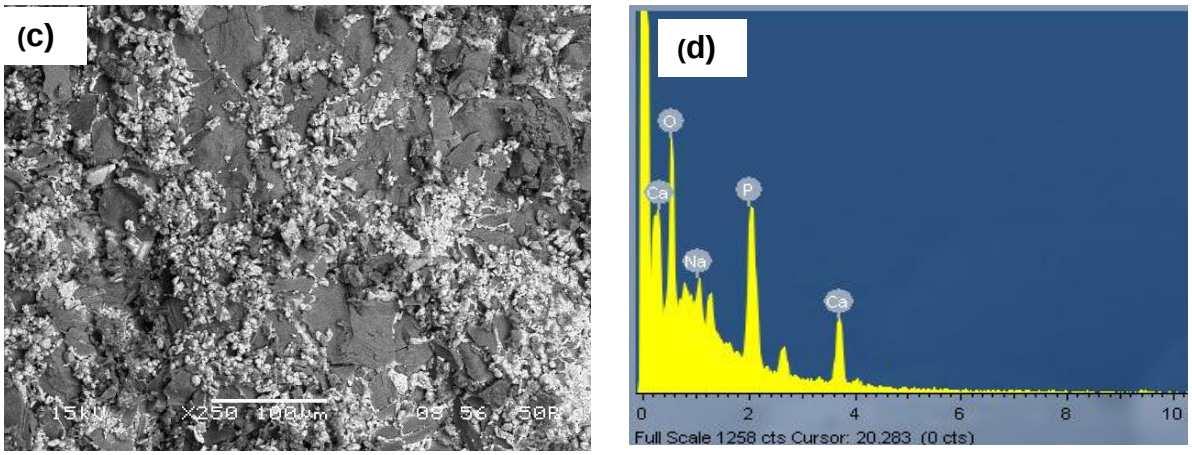

Figure 5.41: Osteogenic differentiation induced through osteogenic differentiation media and mineralization is observed at 28 days was analyzed using (a) TEM showing clearly visible mineral nanocrystals attached to nanofiber (b) and (c) Overcrowded cell matrix with white crystals of calcium phosphate in the ratio 1.6 as obtained from EDX analysis (d).

One of the common way to identify HAp is by measuring the ratio of calcium and phosphate. The Ca:P of phase pure HAp is 1.67 while that of human bone it varies between 1.5-1.7 (healthy human bone 1.63). The variations of this ratio are owing to age, anatomical location and disease condition [206]. The deposition of this precursor phase in biomineralization processes of blended SF nanofibrous scaffold explains the suitability of hMSCs towards osteospecific lineages. This shows the competence of scaffold for osteoinductive property.

The corresponding images of MSCs seeded eri-tasar scaffold constructs treated with alizarin red are shown in Figure 5.42 (c). The Figure 5.42 (a) and (b) indicate the qualitative results from alizarin red staining of cellular constructs for nanofibrous scaffold derived from gelatin and *B. mori* silk respectively. Their quantitative values are given in Figure 5.42 (d). The result indicates the superiority of eri-tasar scaffold over *B. mori* and gelatin towards osteogenic differentiation which is similar to predictions by Binulal et al [207].

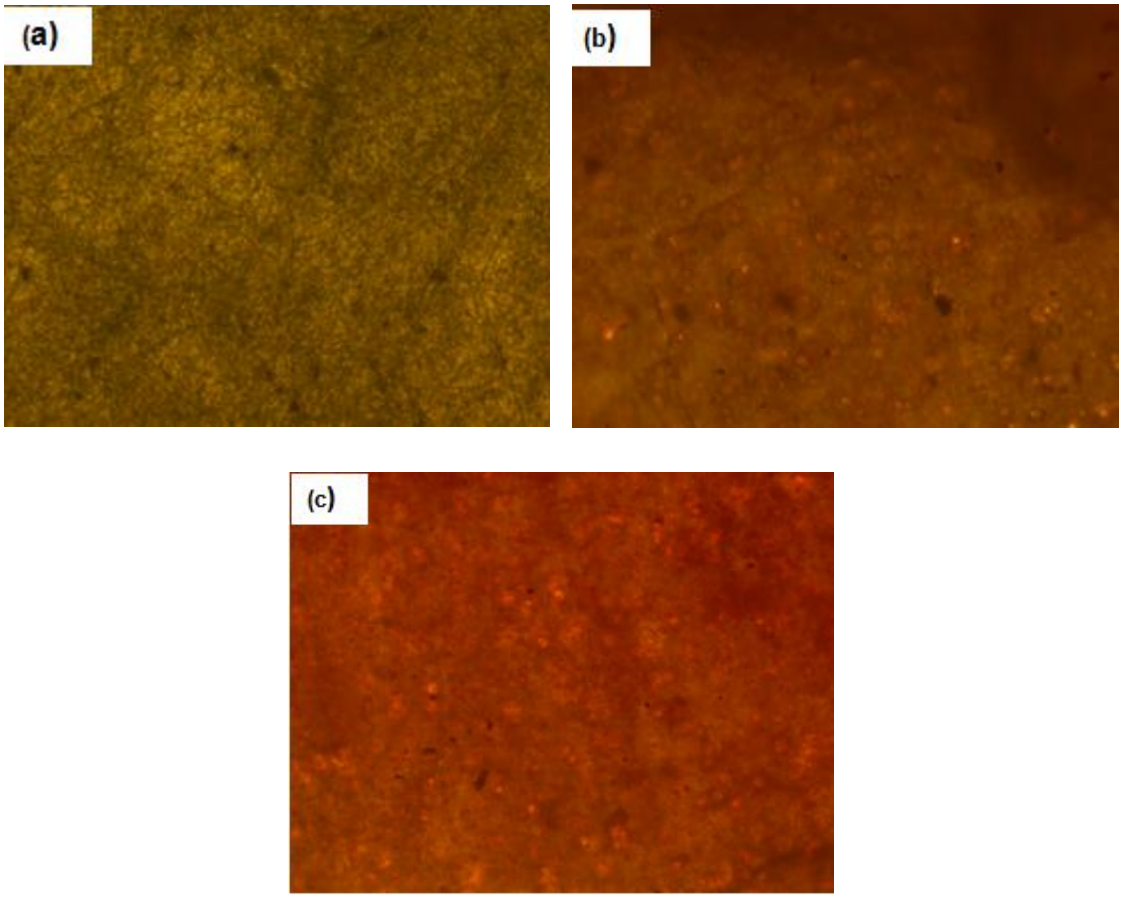

Figure 5.42: Evaluation of mineralization of hMSCs on (a) gelatin (b) BM and (c) SF blend scaffolds using alizarin red staining under fluorescence microscope. Substantially higher mineralization is observed based on high fluorescence intensity.

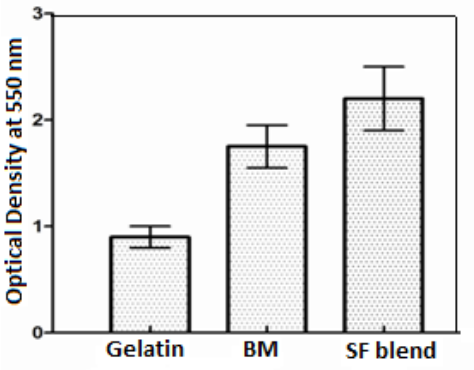

Figure 5.43: Quantitative estimation of relative amount of mineralization on gelatin, BM and ET nanofibrous scaffold.

RUNX2 expression

The osteogenic differentiations of MSCs on the scaffold were further assessed by qualitative analysis of RUNX protein (Figure 5.44). RUNX2 is an early marker of osteoblast differentiation [208]. RUNX2 protein is localized in nuclei of osteoblast [139]. Immunochemistry after 7, 14, 21 days of culture shows qualitative expression of RUNX2. After 14 days, the activity shows a declining phase towards 21 days of activity in both *B. mori* and eri-tasar scaffold. The overall signal in the field of observation was calculated and the fluorescence intensity per cell was measured. The observation demonstrated that fluorescence signal intensity per cell is stronger after 14 days as compared to the signal intensity after 21 and 7 days. On the other hand, the observed intensity per field (area of observation) in case of eri-tasar is higher than *B. mori* which may be attributed to the presence of more number of RUNX2 expressed cell as well as higher fluorescence intensity per cell present over eri-tasar.

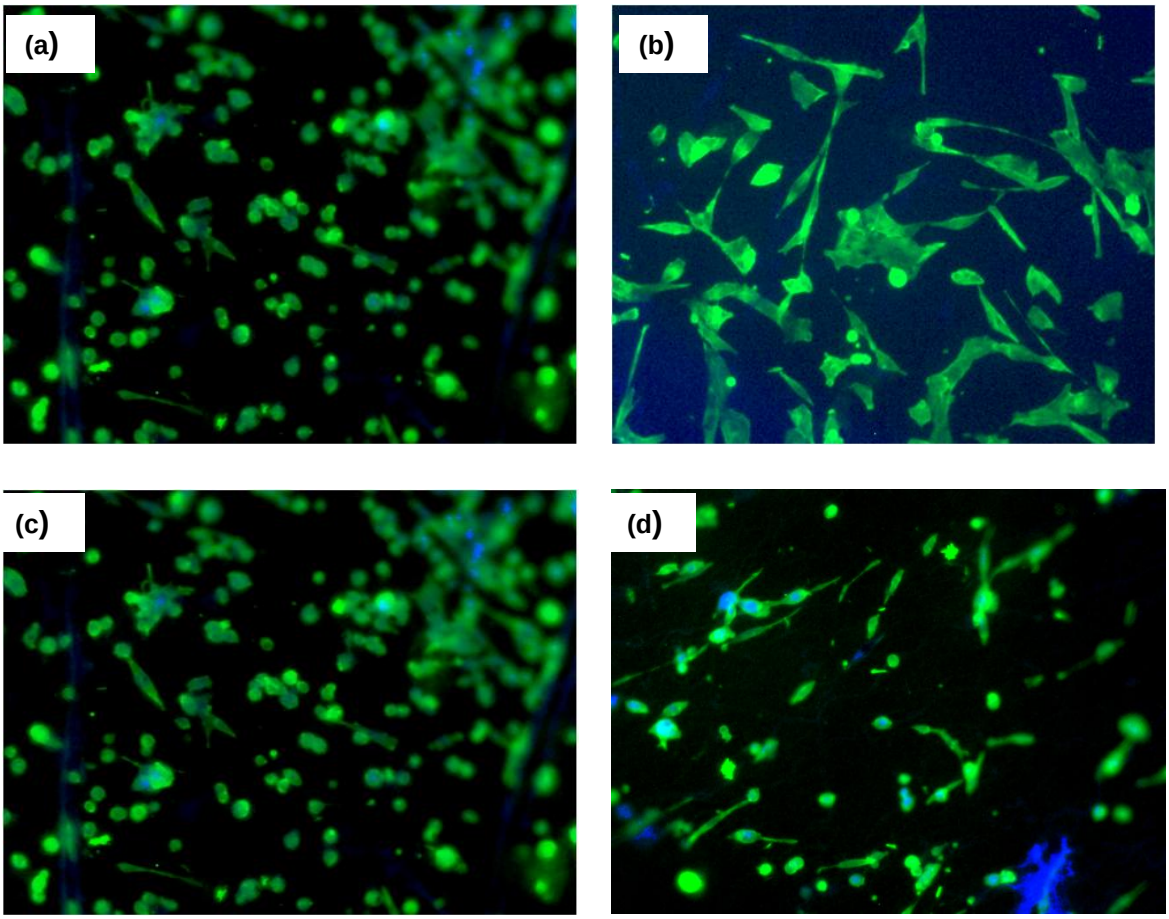

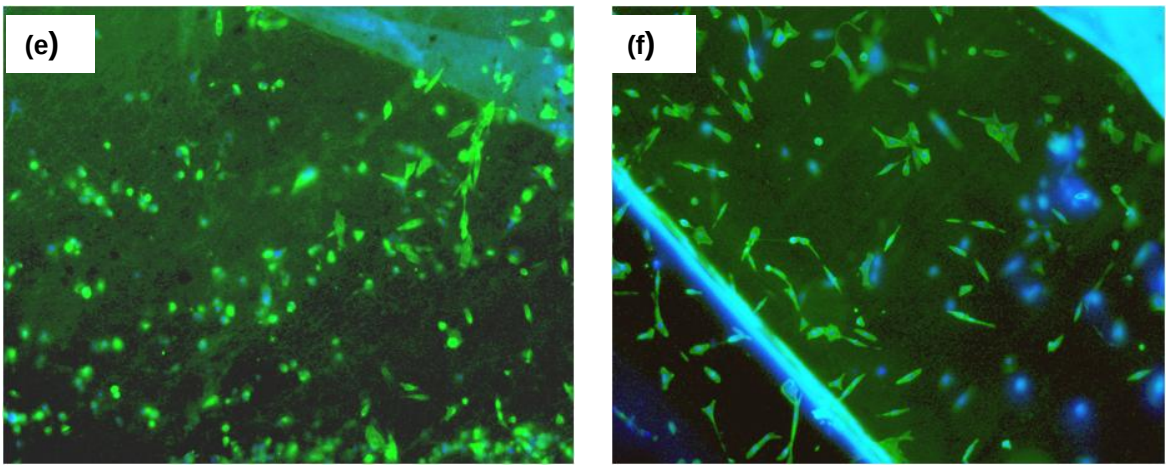

Figure 5.44: Subcellular localization of RUNX2 protein through immunofluorescence staining by FITC conjugated secondary antibody counter stained with HOEST after 7, 14 and 21 days of culture on B. mori (a-c) and SF blend (d-f).

Osteocalcein activity

Osteocalcin is a late stage marker for complete osteogenic differentiation [209]. Initially, their expressions are observed to be very low and substantial increase in expression occurs after 14 days of culture. Figure 5.45 shows the expression of osteocalcin over differentiated MSCs grown over gelatin, *B. mori* and eri-tasar after 14 and 21 days of culture. The overall fluorescence signal intensity in the field of observation was measured and per cell was determined. The observation found that expression of osteocalcin depends on time as well as type of scaffold. The overall field intensity is less in case of gelatin and *B. mori* as compared to eri-tasar after 21 days. Even after 14 days, osteocalcein expression over differentiated MSCs is better than those of gelatin and *B. mori*. Additionally, the fluorescence intensity per cell over eri-tasar found to be higher, although there is more number of cells per field in gelatin and *B. mori* scaffold.

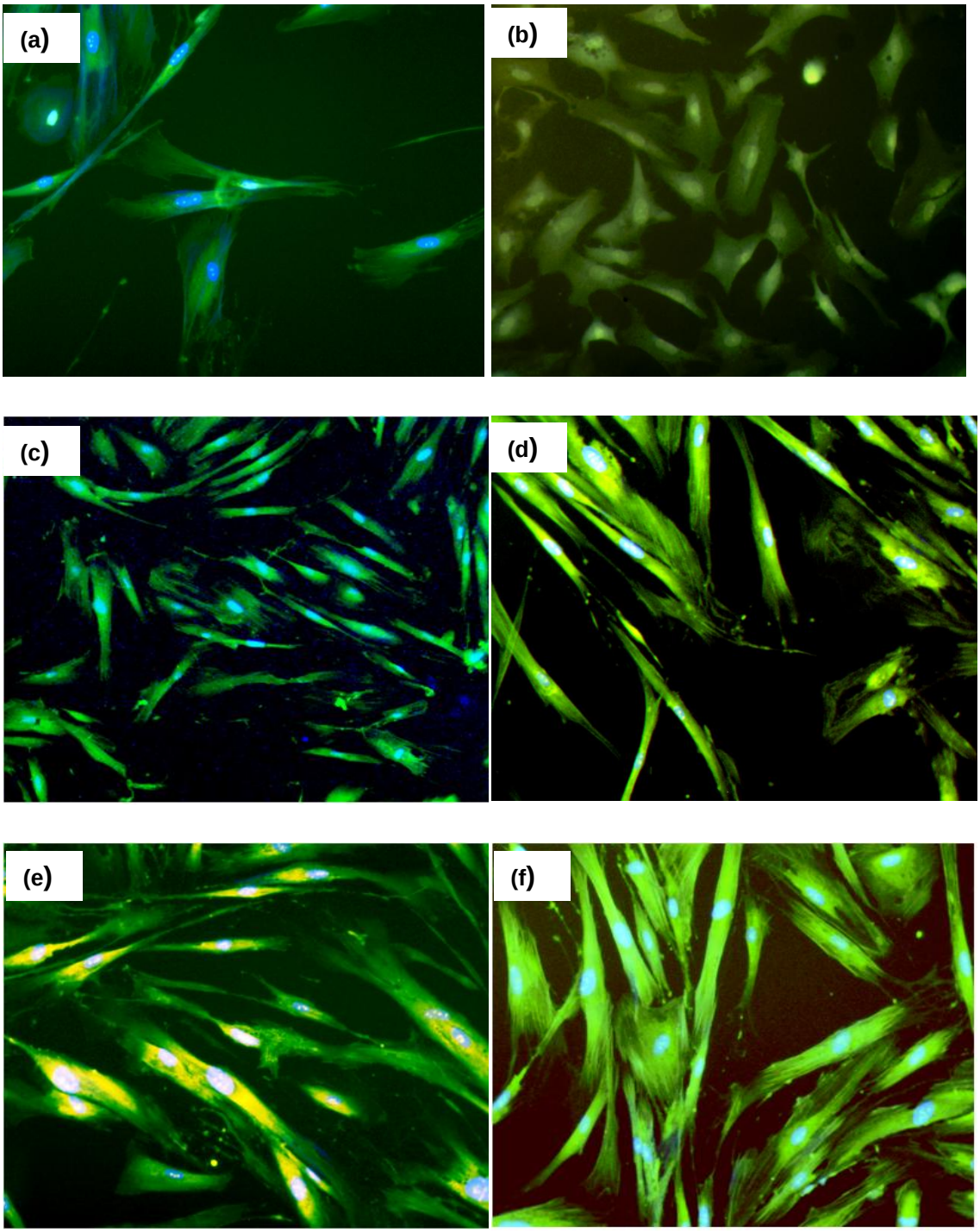

Figure 5.45: Osteocalcein staining for bone phenotype on gelatin, B. mori and SF blend nanofibrous scaffold after 14 and 21 days of culture (a) and (d) hMSCs over gelatin (b) and (e) hMSCs over B. mori (c) and (f) hMSCs over eri-tasar nanofibrous scaffold.

Further quantitative analysis of osteocalcin after 7, 14 and 21 days of culture (Figure 5.46) has supported the previous finding and stipulated its better osteogenic behavior. As indicated in figure, the osteocalcein activity is remarkably higher than the other two scaffolds after 21 days of culture with gelatin showing lowest osteocalcein activity.

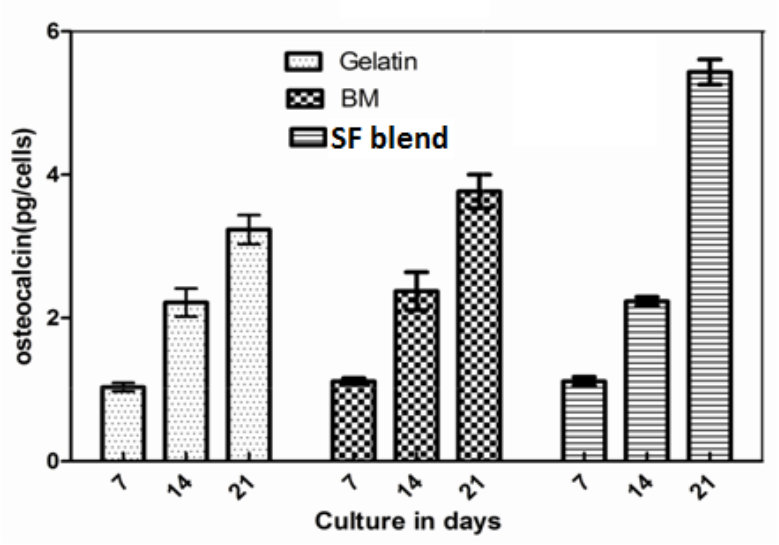

Figure 5.46: Quantitative expression of osteocalcin as measured in hMSCs cultured over gelatin, B. mori, SF blend scaffold.

Together with the hMSCs differentiation into osteogenic lineages was confirmed by ALP activity, RUNX2 expression, matrix mineralization and osteocalcin expression. Mineralization and osteocalcin expression are considered as formation of mature osteocytes and our results showed that hMSCs on nanofibrous scaffold are differentiated and mineralized the matrix upon stimulation with osteogenic media. The mineralized crystals deposited over nanofibers are in nano scale as found in natural bone and clearly visualized through HRTEM and as aggregated particles through SEM. EDX analysis demonstrated the Ca:P ratio of the mineral deposits was the same as that of hydroxyapatite [210]. ALP is expressed earlier in osteoblast cells and osteocalcin is expressed in fully differentiated osteoblasts. RUNX2 is expressed during its transition from immature osteoblast to mature osteoblasts. The above study suggests that blended eri-tasar nanofibrous scaffold provides an in vivo like in vitro environment and therefore the cells respond naturally. Differentiations of hMSCs into mature osteoblast-like cells were further confirmed by expression of osteocalcin where mature osteoblasts undergo mineralization [211]. The higher response of blended eri tasar nanofibrous scaffold compared to *B. mori* SF

nanofibrous scaffold suggests the greater osteogenic potential for this system. Overall, these studies suggest that eri-tasar composite silk nanofibrous scaffold offers significant osteogenic potential warranting further study towards bone tissue graft development.

PART III

Development of SF/nHAp composite scaffold

Several studies have suggested that the use of HAp, $Ca_{10}(PO_4)_6(OH)_2$ (Ca:P-1.67), the chief constituent of bone promote osteogenic property of scaffold material [212,213]. Therefore, a number of researchers have attempted to develop composite scaffolds using natural polymers such as SF, collagen, gelatin, chitosan and HAp. Most of these composite scaffolds with porous and fibrous structures were prepared by mechanical mixing of desired amount of HAp with natural polymers. However, the major drawback of this process is that the mineral phase does not form in situ and only simply adheres to the surface of polymer fibers that provides poor interaction between them due to the formation of agglomerates [214]. To overcome this problem an advanced method called direct mineralization involving the precipitation of mineral phase within the polymer solution has been developed as reported [215, 216]. Therefore, in the present study, research work focuses on the development of SF/nHAp composite scaffold with improved osteogenic characteristics by precipitating nHAp over the developed eri-tasar SF blend nanofibers following direct mineralization. The results and discussion are presented here.

5.3.1 Characterization of SF/nHAp scaffold

5.3.1.1 Morphological characterization

Figure 5.47 shows the precipitation of nHAp crystals over blended eri-tasar SF nanofibrous scaffold after three cycles of treatments. The nHAp are deposited in the agglomerated form as can be seen from SEM images (a) on close observation it was found that the particles not only deposited on the surface of the fibers but also on the inside of fibers. They also deposited on the fibers below the surface. The particles were of different shapes and sizes in 30-50 nm. The attachment of the nHAp particle to the fibers is further seen under TEM. Figure 5.47 (b & c) clearly shows that the attached nHAp crystals are growing randomly on the SF nanofibers. The sizes of the nHAp particles are not uniform in shape but resemble crystalline structure. Furthermore, the transparent portions of the deposited HAp particles resemble to be crystalline while the dark and opaque portion is the amorphous in nature. The crystallinity of the nHap was further confirmed by XRD analysis. EDX analysis revealed that Ca and P ions are in the ratio of 1.6 confirming the deposition of nHAp over SF nanofibers. Thus, mineralization of nanofibrous scaffold with HAp is expected to provide a favorable environment for bone tissue engineering.

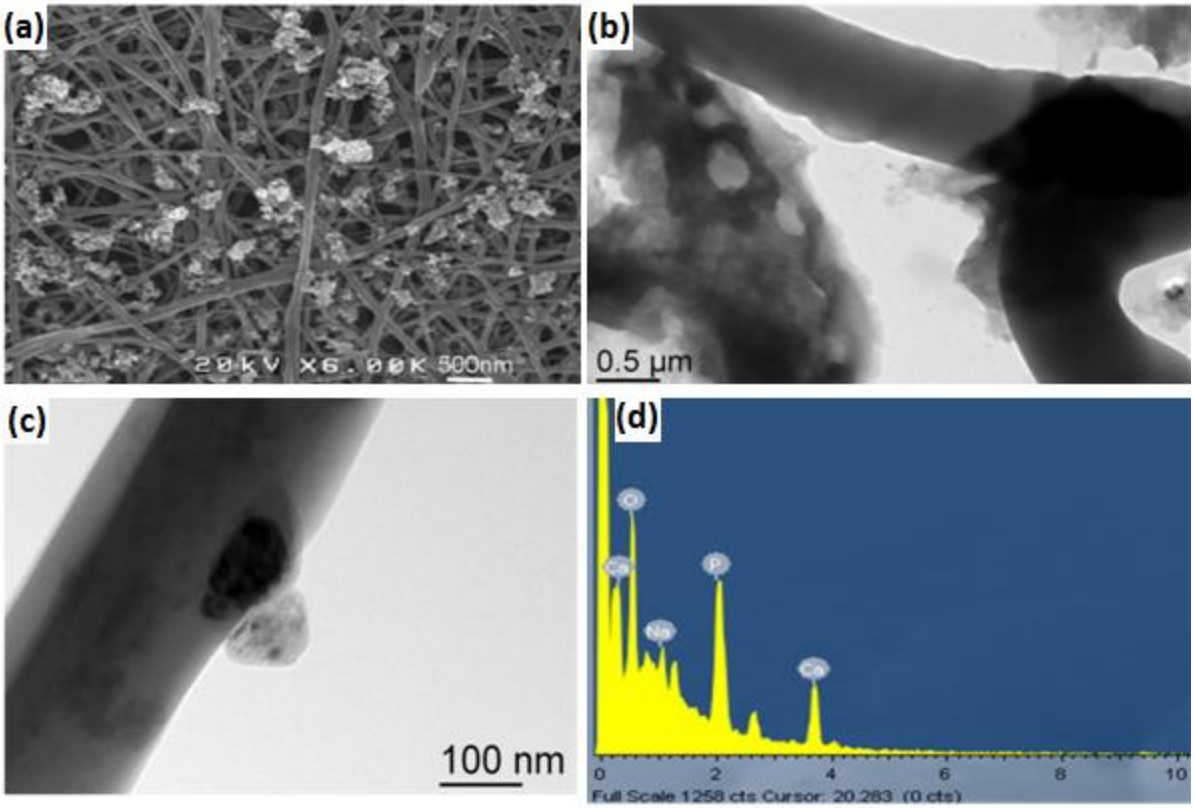

Figure 5.47: (a) SEM (b) and (c) TEM images of nHAp particles deposited over blended eri-tasar SF nanofibers (d) EDX analysis depicts the presence of Ca and P ions on nanofibers.

5.3.1.2 Structural analysis

XRD

Phase analysis of SF/nHAp nanofibrous scaffold was carried out by XRD as shown in Figure 5.48. As it is indicated, the diffraction pattern shows the characteristic peaks of α-helix structure at $21^0(2\theta)$ and β-structure at 29.54(2θ) which confirms the semicrystalline nature of the fiber. A peak at 39.26^0 corresponds to the characteristic peak of HAp. Thus mineralization of SF was proved to be occuring due to the precipitation of HAp over the developed SF nanofibers [94,161,217]. Furthermore, from the XRD study it can be concluded that HAp produced by surface precipitation method is semicrystalline in nature.

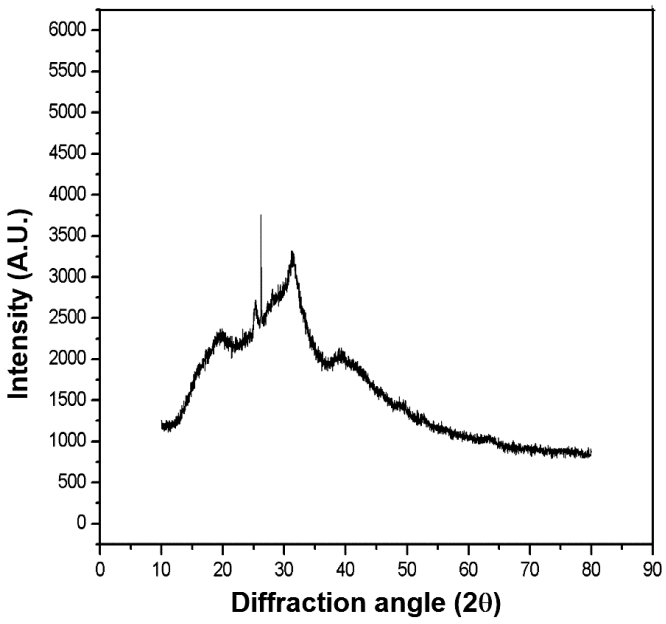

Figure 5.48: XRD of HAp precipitated over SF blend nanofibrous scaffold.

FTIR

Figure 5.49 demonstrates the interaction of functional groups present in SF/nHAp scaffold. The absorption band at 697, 612 and 563 cm^{-1} in Figure 5.48 corresponds to O-P-O bending in the mineralized SF scaffold which indicates the presence of nHAp over nanofibers. The absorption band at 958 cm^{-1} corresponds to o-p-o stretching vibration indicating the presence of PO_4^{3-} group. The C=O stretching vibration of amide I at 1658 cm^{-1} and N-H bending of amide II band at 1524-1530 cm^{-1} for both eri-tasar SF and mineralized SF/nHAp are observed from FT-IR spectra.

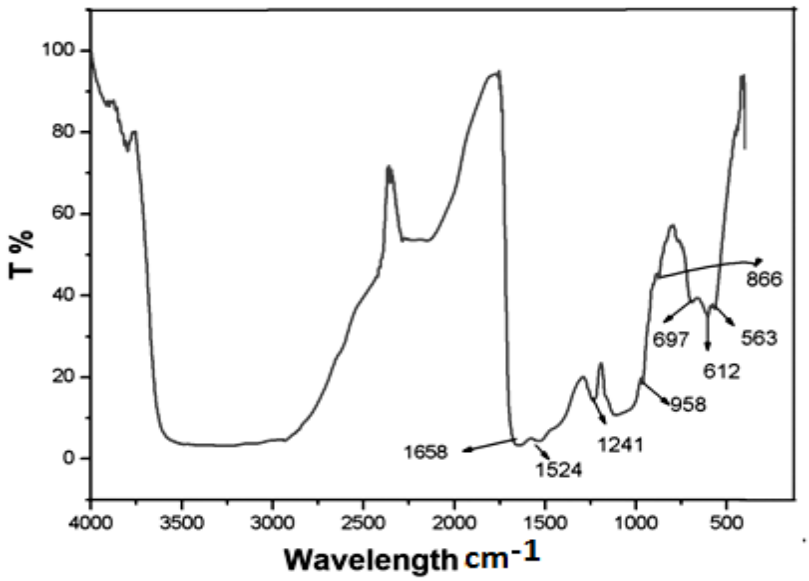

Figure 5.49: FT-IR analysis of SF/nHAp nanofibrous scaffold

On close observation of FT-IR spectra (Figure 5.49), it has been observed that the intensity of two amide peaks present in nHAp deposited on SF nanofibers were repressed severely as compared to pure SF blend scaffold. This may be due to the deposition of HAp over SF nanofibers which can be explained through interaction between Ca^{2+} ions of HAp and C=O bonds in amino acids of scaffold [218]. Consequently, HAp crystals precipitated on the surfaces of SF would provide nucleation site for CaP crystals [219].

5.3.1.3 Thermal analysis

Figure 5.50 shows TGA analysis carried out with SF/nHAp composite scaffold. The observed weight loss at 100^0C is probably due to water evaporation present in the fiber without being chemically attached. In comparison, the weight loss is found to be varying between SF and SF/nHAp scaffold in the range 6-7% (Figure 5.50), higher weight loss observed with pure SF scaffold (10-12% reported earlier). The mineralized SF composite scaffold has started decomposition above 350^0C and its residual weight loss is about 15%. However, a sharp decomposition with weight loss about 30-35% is shown at about 375^0C. It is observed that eri-tasar SF blend/nHAp has started degradation at higher temperature than pure eri-tasar blend SF due to present of inorganic salt HAp [94].

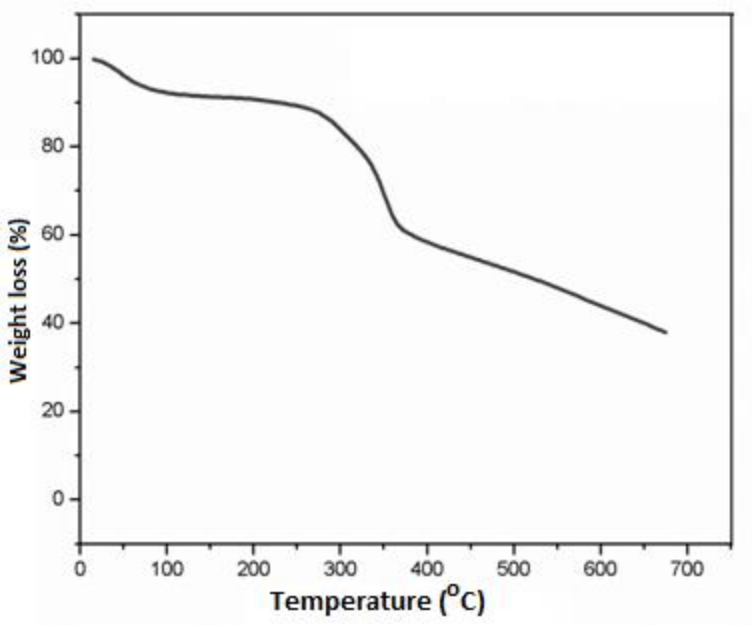

Figure 5.50: TGA of SF/nHAp nanofibrous scaffold

5.3.1.4 Mechanical properties

It has been reported that HAp scaffolds possess poor mechanical strength, particularly low strength and brittleness limit their applications to tissue implants [220]. Therefore, the effect of mineralization using HAp on the tensile strength of SF scaffold was investigated by analyzing the stress-strain curve (Figure 5.51) of the developed scaffold. Four different nanofibrous sheets of identical thickness prepared in different batches were represented by different color codes as depicted in figure. A drastic reduction in ultimate tensile strength and %elongation of SF blend scaffold is observed which is due to the HAp deposition. The corresponding ultimate tensile strength and % extension of HAp mineralized SF scaffolds are measured to be 0.392MPa and 2.895% respectively whereas these values for pure ET scaffold are 1.83 MPa and 7.756% *(Figure 5.15).* Similar results are also reported for PCL/HAp and PLA /HAp electrospun scaffolds [221, 222]. Additionally, it has been observed that the ductile property of SF/nHAp has been reduced which is evident from the nature of graph and measured %extension of the scaffold. The decrease in UTS may be attributed to the restricted free moments of nanofibers resulting due to the presence of nHAp. The deposition of HAp makes nanofibrous matrix more stiff and less plastic because of hard inorganic phase and high charge density of HAp [221]

However, the developed SF/nHAp scaffolds still have the desired tensile strength and % elongation required for its application in non-load bearing bone tissue regeneration.

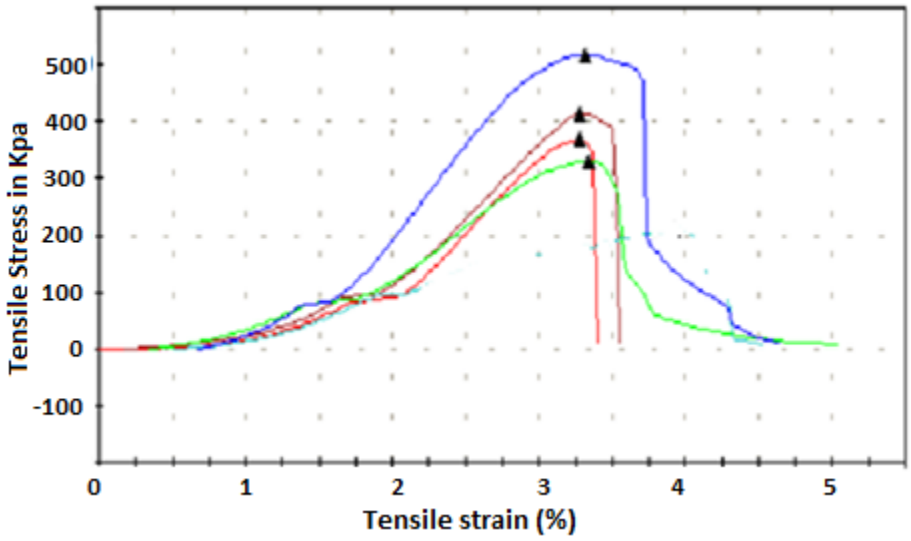

Figure 5.51: Stress strain curve of HAp deposited SF nanofibrous blend scaffold.

Additionally, it has been observed that the ductile property of SF/nHAp has been reduced which can be understood from the nature of graph and extension % of scaffold. However, the developed SF/nHAp scaffolds still have the desired tensile strength required for its application in non-load bearing bone tissue engineering.

5.3.1.5 Water uptake capacity and measured contact angle

Figure 5.52 demonstrates a comparative study of % water uptake observed with SF and SF/nHAp scaffolds. The % water uptake and swelling ratio of SF/nHAp nanofibrous scaffold are measured as 79% and 0.83 after 96 h of treatment in PBS.

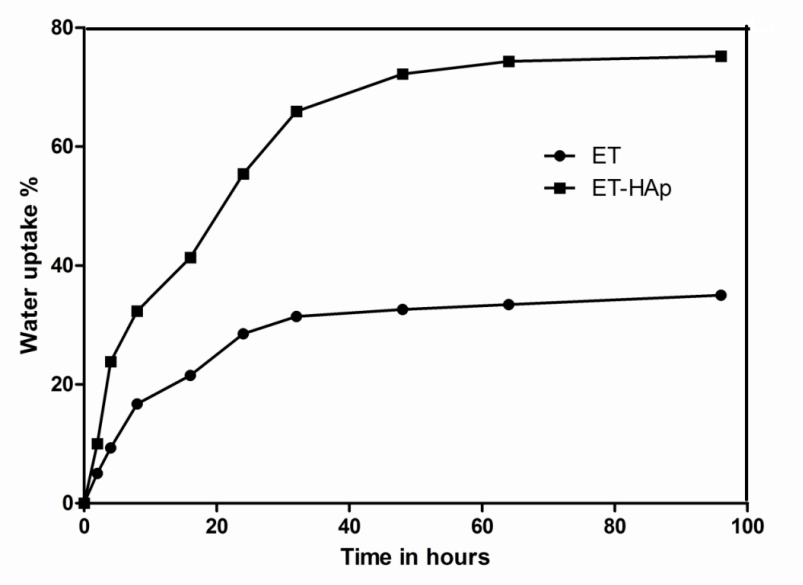

Figure 5.52: Water uptake capacity of SF blend and SF/nHAp scaffold after 96 h of treatment in SBF.

Thus, water uptake capacity and swelling index of SF/nHAp composite scaffold are found to be higher than pure SF blend scaffold (Figure 5.52). The higher water uptake capacity reflects higher hydrophilicity characteristic of composite scaffold. This was further confirmed by water contact angle measurement. The measured contact angle is 53.4 ± 2.7^0 which is lower than SF blend scaffold. Therefore, the developed composite scaffold has shown enhanced surface property that is favorable for bone tissue engineering application.

5.3.1.6 Bioactivity study

The ability of a material to deposit HAp crystal over its surface determines its osteogenic property. Figure 5.53 shows SEM images of mineralized SF scaffold after 14 days of treatment in SBF. nHAp crystals are observed to cover the surface of scaffold that proves the suitability of the composite scaffold for bone tissue regeneration.

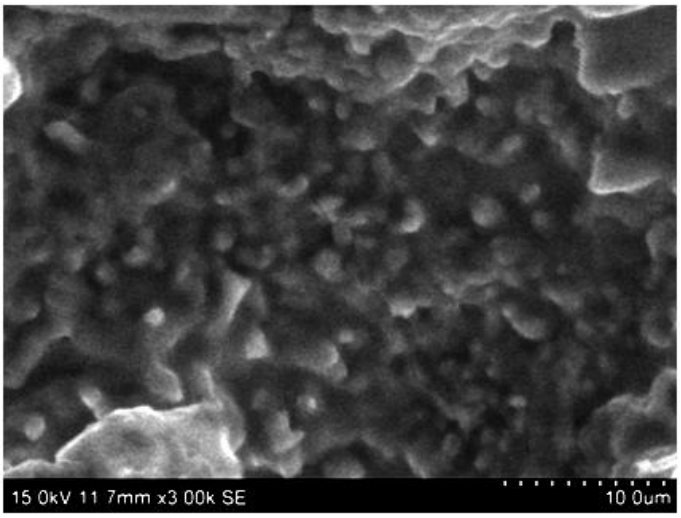

Figure 5.53: Bioactivity of SF blend/nHAp scaffold by SEM after 14 days treatment in SBF

5.3.2 In vitro cell culture study

5.3.2.1 Morphology and attachment of MSCs

As explained in previous chapter, one of the selection criteria of tissue engineered material is the attachment profile of MSCs on scaffold. Several studies have reported that surface precipitation of apatite crystals provides certain degree of toxicity in cell attachment [220]. Therefore, it is important to verify whether the deposition of nHAp has any toxic effect on MSCs attached to the developed composite scaffold. After 48 h of culture, MSCs were found to attach on the nanofibrous composite scaffolds with elongated and well-spread morphology as evident from confocal images (Figure 5.54). This suggests that composite SF/nHAp scaffold is a good substrate for growth and proliferation without significant toxic effect.

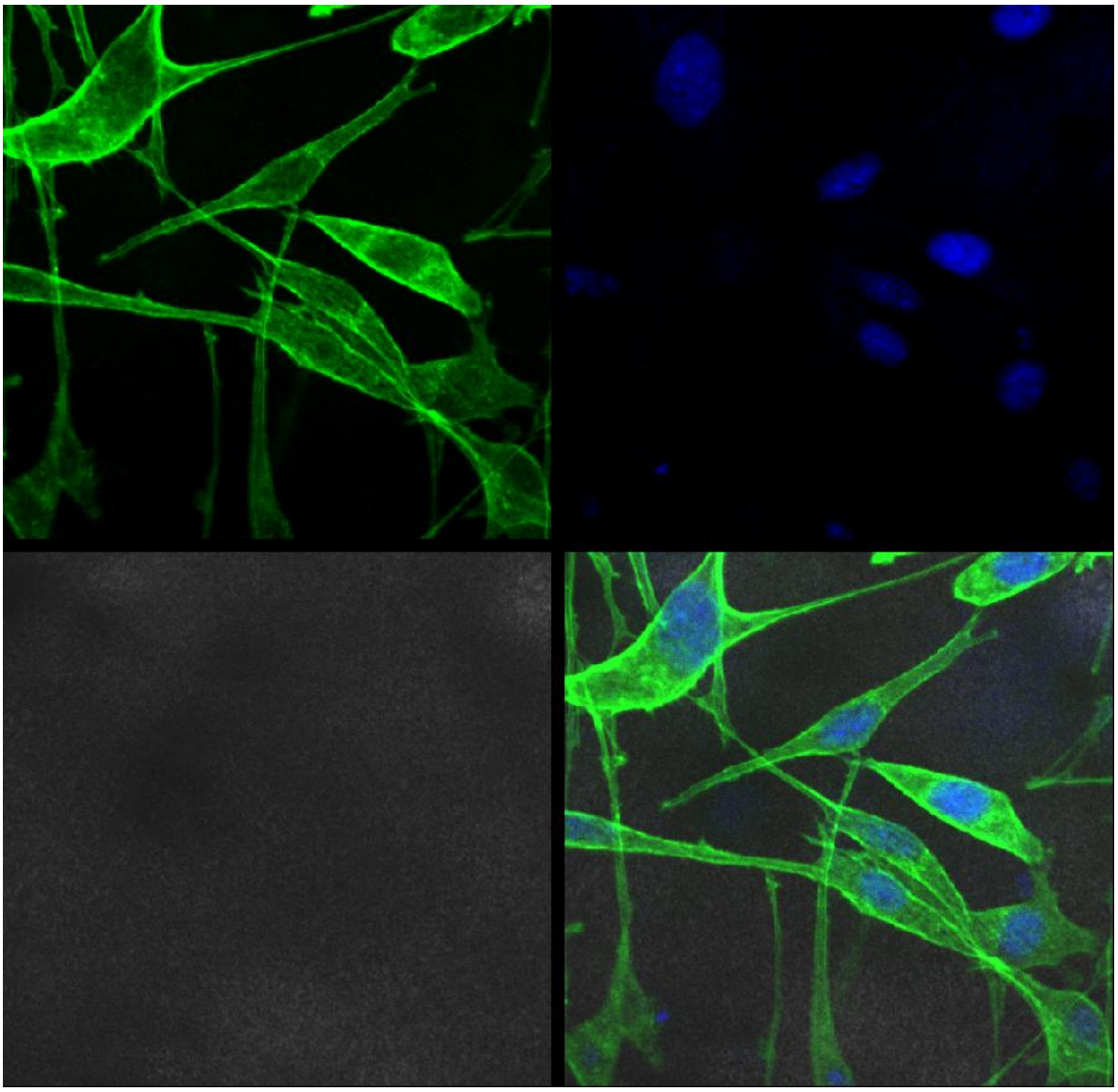

Figure 5.54: Confocal Laser Scanning Microscope images of MSCs attachment over SF/nHAp nanofibrous scaffold. MSC cultures were stained for β-actin (Phalloidin Cytoskeleton-green) and DAPI (nuclei, blue) scale bar 25 µm.

5.3.2.2 Metabolic activity of MSCs

Figure 5.55 (a-b) demonstrate relative cellular metabolic activity of hMSCs grown over SF and SF/nHAp stained with CMFDA dye under fluorescent microscope after 72 h of culture. It has been observed that the fluorescence intensity per cell was slightly higher in case of pure SF blend scaffold. However, the number of cell under the area of observation in SF blend scaffold is higher than that of SF/nHAp scaffold. The results are further quantified by MTT assay.

The metabolic activity of a cell generally takes place in G1 phase which is the pre-DNA synthesis period. It determines the ability of a cell to proceed further in the cell cycle [221]. MTT assay was performed to assess cellular metabolic activity of hMSCs over pure SF blend and SF/nHAp scaffolds based on 3, 5, 7 and 10 days of hMSCs culture as shown in Figure 5.56. Slightly higher cellular metabolic activity is observed with SF blend scaffold than SF/nHAp scaffold. The corresponding cell viability values are steadily increasing up to 10 days in both the cases. Slightly lower metabolic activity observed with the composite scaffold bears no statistical significance claiming the SF/nHAp scaffold of comparable activity.

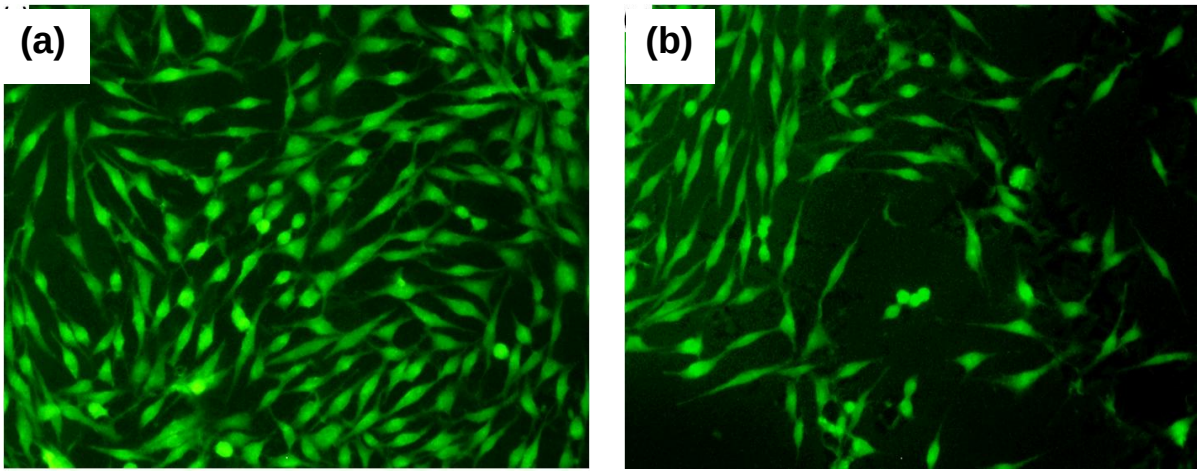

Figure 5.55: Fluorescence microscopic images (CMFDA dye image) showing cell viability and proliferation after 5 days on (a) SF blend and (b) SF/nHAp composite scaffold.

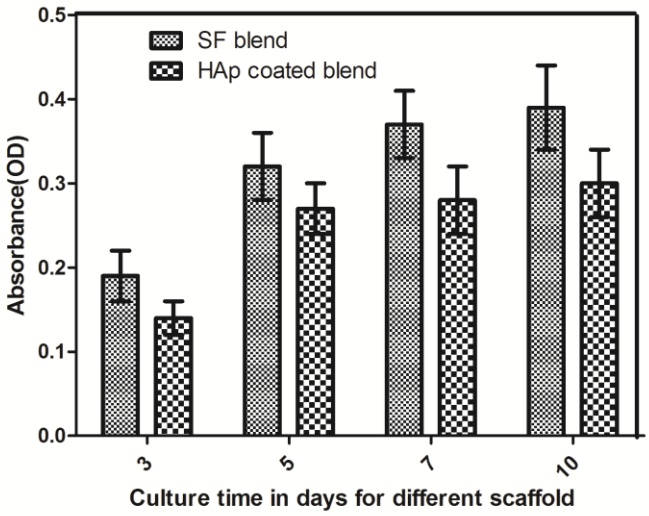

Figure 5.56: MTT assay for cell viability after 3, 5, 7 and 10 days of culture on SF/nHAp composite scaffold

5.3.2.3 Cell Proliferation

The proliferations of MSCs on the scaffolds were observed by SEM after 7 and 14 days of culture on and SF/nHAp scaffold to investigate the effect of deposited nHAp on the cell proliferation. Figure 5.57 (a) and (c) show the proliferation of MSCs after 7 and 14 days of seeding on ET, whereas (b) and (d) over ET/nHAp.. Both types of scaffolds show extensive proliferation and deposition of secretary extracellular matrix substances. The extensive proliferation and deposition make it difficult to visualize the fibrous morphology. As indicated in Figure 5.57, cell proliferation is progressively increased with culture period up to 14 days and then the rate follows a decline in trend which is the case for both pure and HAp deposited scaffold. Furthermore, the proliferation rate of MSCs on SF/nHAp and control (SF) is found to be comparable in nature. SEM study has further indicated that proliferated cells are aggregated and overcrowded with substantial deposition of secretory products in both types of scaffolds with a little higher deposition in SF/nHAp composite scaffold.

Quantitative estimation of cellular proliferation over pure SF blend and SF/nHAp scaffolds was done using Alamar blue assay. Cellular proliferation over SF blend scaffold is found to be higher than that of SF/nHAp. The rate of proliferation is found to increase with the increase in culture period up to 14 days followed by a decline in the growth rate beyond this period as observed in Figure 5.58. However, this slightly higher rate of cell proliferation over SF/nHAp may not differ much to affect differentiation process.

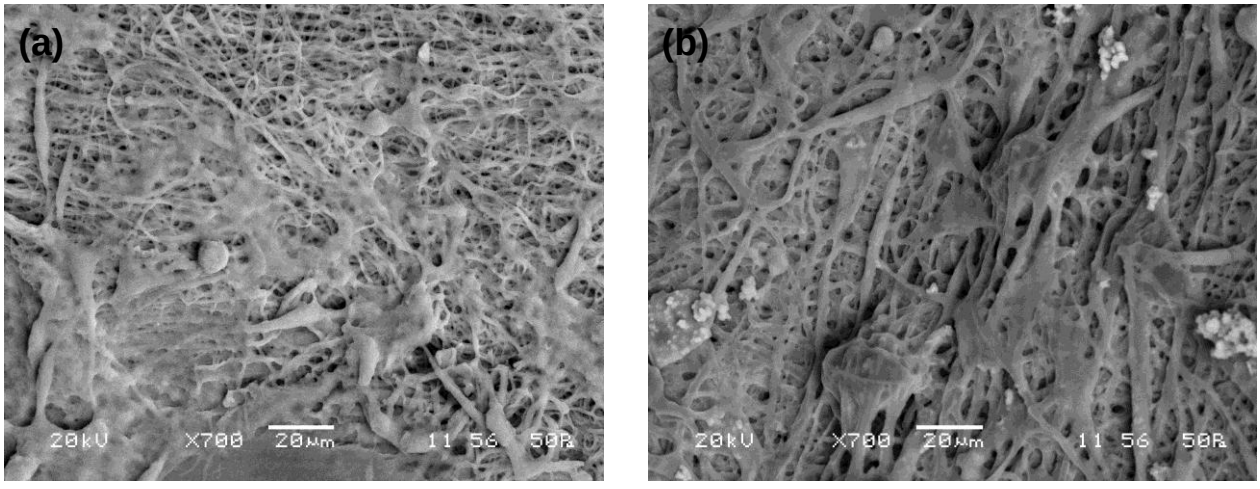

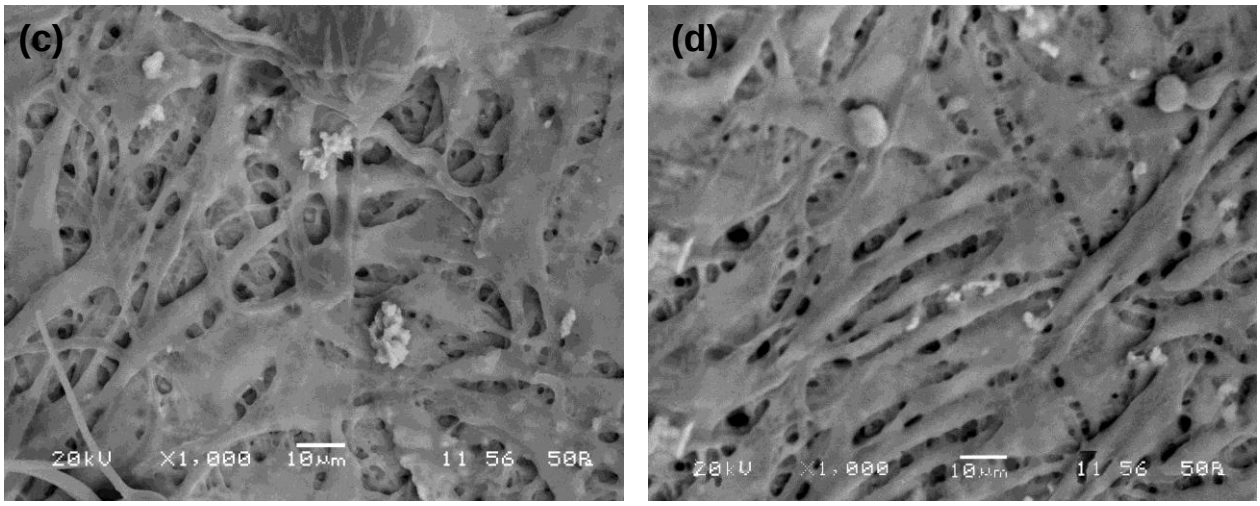

Figure 5.57: SEM images show cellular proliferation after 7 and 14 days of culture over SF blend and SF/nHAp composite scaffolds.

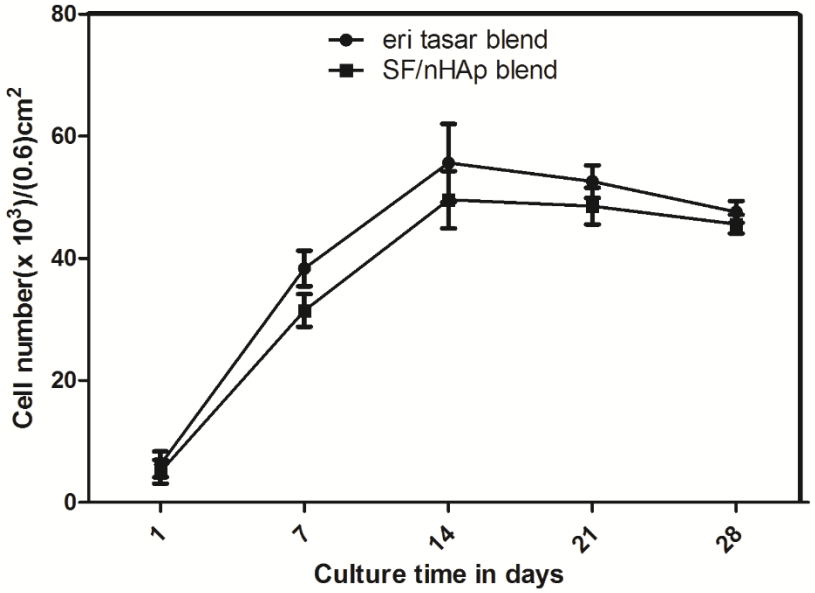

Figure 5.58: Alamar blue assay for hMSC proliferation on blended SF blend and SF/nHAp composite scaffolds over 28 days of cell culture

5.3.2.4 Cell adhesion molecules: CD44 and CD29 (Beta 1 integrin receptors)

As it is observed in the previous chapter, the expression of CD44 and CD29 is an important factor in deciding the suitability of outer matrix environment in cell adhesion processes.

Therefore, the expression of these markers over MSCs on SF/nHAp scaffold was estimated by flow cytometry analysis depicted in Figure 5.59. Both CD29 and CD44 expressions of MSCs were observed in all the scaffolds as well as control with a varying degree of expression. MSCs grown over gelatin scaffold were used as negative control. 12% CD29 and 38% CD44 expressions are achieved after 24 h of MSCs grown over the control. However, the pure SF blend scaffold has shown maximum expression of CD44 (89%) and CD29 (94%). A significant decrease in expression of CD44 (67%) and CD29 (71%) is observed with SF/nHAp scaffold. The reduction in expression may be explained as the reduction in availability of RGD ligand due to surface covered by nHAp. However, their expression level is adequate to drive the cell for proliferation and differentiation.

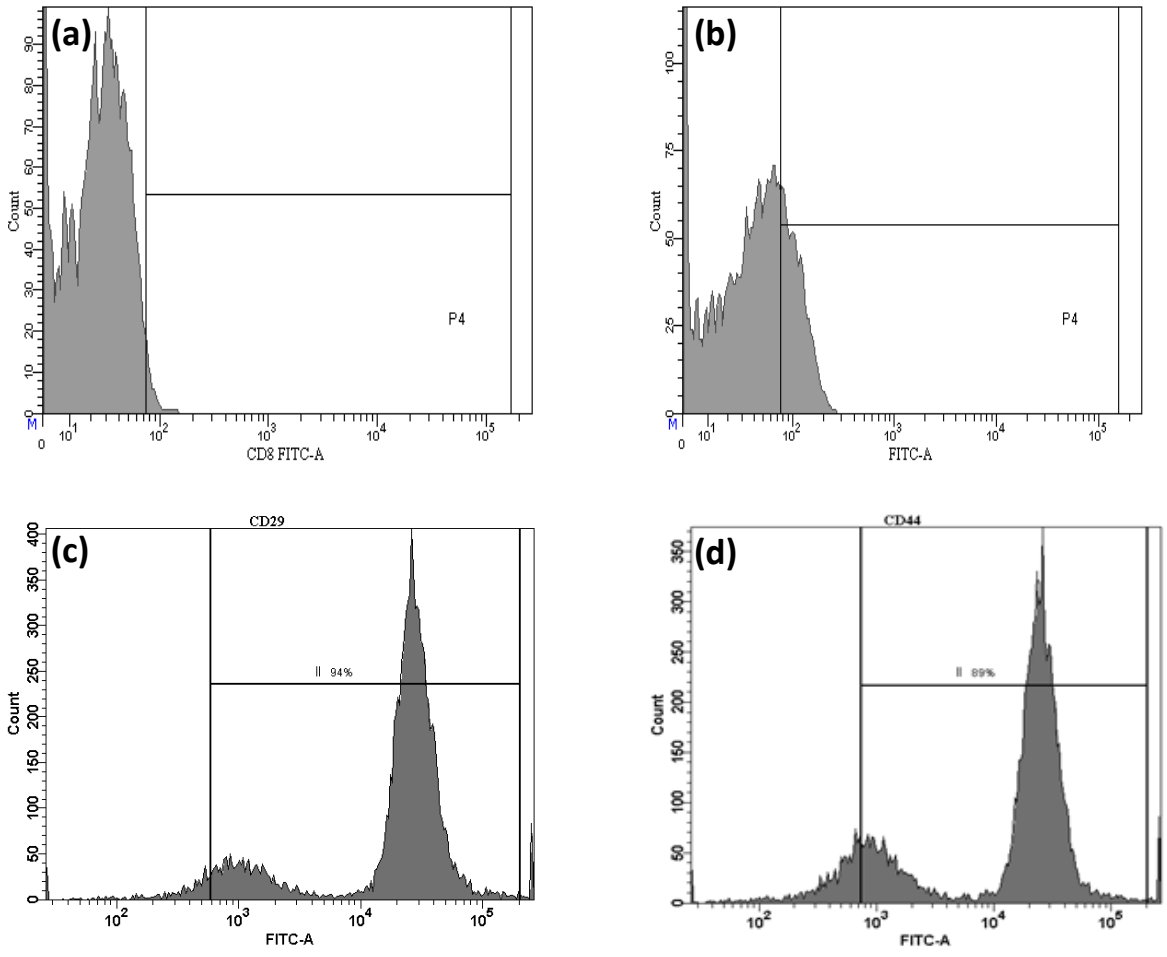

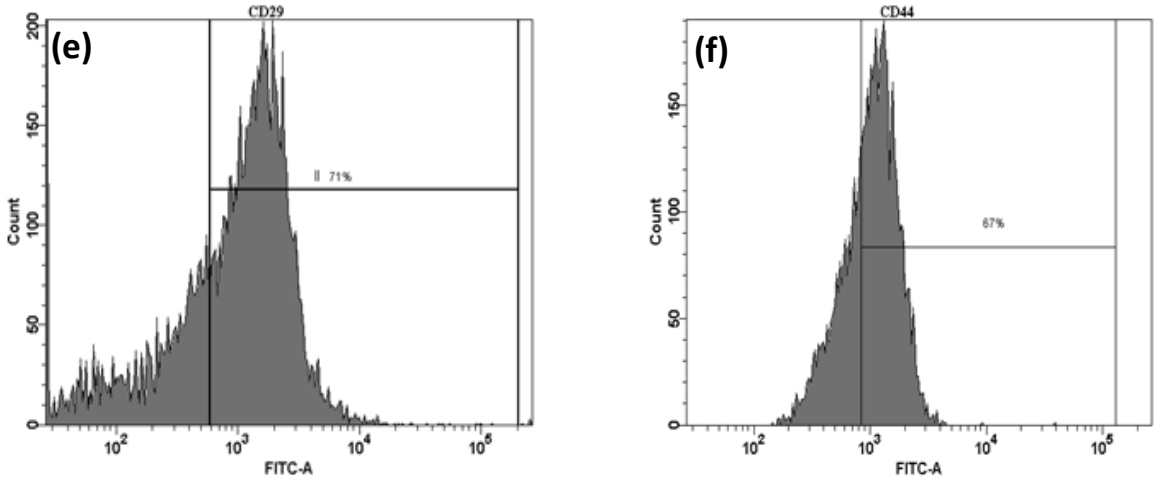

Figure 5.59: Expression of cell adhesion molecules CD 44 and CD 29 (beta 1 integrin) (a) and (b) –ve control, (c) and (d) SF blend scaffold, (e) and (f) SF/nHAp composite scaffold.

5.3.2.6 Osteogenic differentiation of MSCs

The MSCs can differentiate into various cell types such as osteogenic and chondrogenic lineages where the matrix elasticity plays an important role. In contrast, a high density of cells may affect differentiation process even if the elastic modulus of matrix is favorable for osteogenic differentiation [222]. Therefore, the suitability of scaffold to differentiate into osteogenic lineages has been studied through the expression of different markers as well as the study of mineralization.

ALP assay

Figure 5.60 demonstrates ALP activity of MSCs over gelatin, SF blend, SF/nHAp composite scaffolds after 7, 14 and 21 days of culture. It has been observed that the ALP activity is significantly higher over SF and SF/nHAp as compared to gelatin. The absorption intensity which is a measure of ALP activity shows 115% increase in absorption during the period of 7-14 days while after 21 days it shows an increase of 128%. Similarly, the change in absorption intensity after 14 days for SF and SF/nHAp is 160% and 185%, while an increase of 190% and 205% is noticed after 21 days. Thus the rate of ALP production is higher during 7-14 days than the period between 14-21 days. This indicates that major change in osteogenic property occurs between the 7-14 days of growth. Furthermore, the ALP activity is significantly higher over

SF/nHAp as compared to SF scaffold after 21 days. Thus, the study suggests an enhanced osteogenic potential of SF/nHAp composite scaffold due to nHAp deposition.

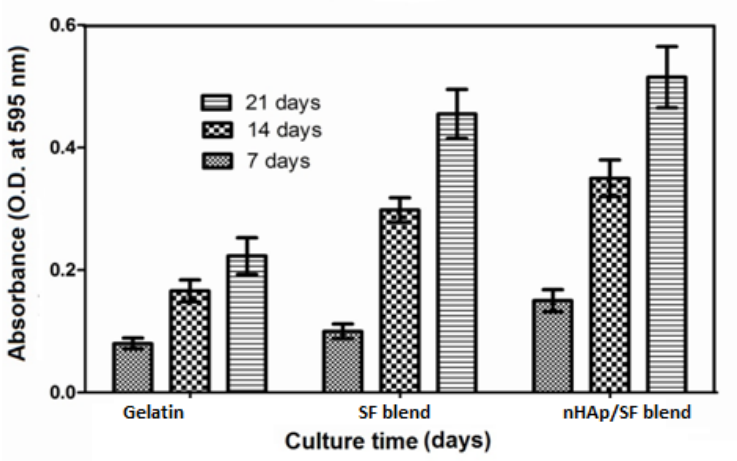

Figure 5.60: ALP activity of hMSCs on gelatin, SF blend and SF/nHAp composite scaffolds after 7, 14 and 21 days of culture

Mineralization of hMSCs on SF/nHAp scaffolds

Immunofluorescence study by alizarin red staining in Figure 5.61 (a-c) clearly indicates significantly higher amount of mineralization over SF blend/nHAp composite scaffold compared to other scaffolds used in this study after 28 days of culture of MSCs. The quantitative estimation of alizarin red assay (Figure 5.61 (d)) also confirms similar results. This shows the highest mineralization activity of differentiated MSCs over HAp precipitated nanofibrous scaffold representing the higher osteogenic potential of SF/nHAp compared to pure SF blend nanofibrous scaffold.

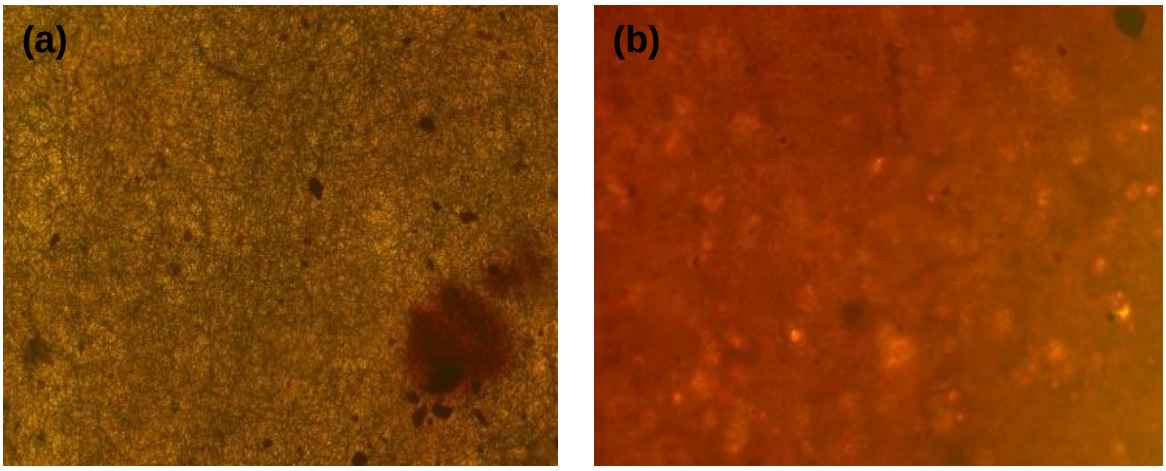

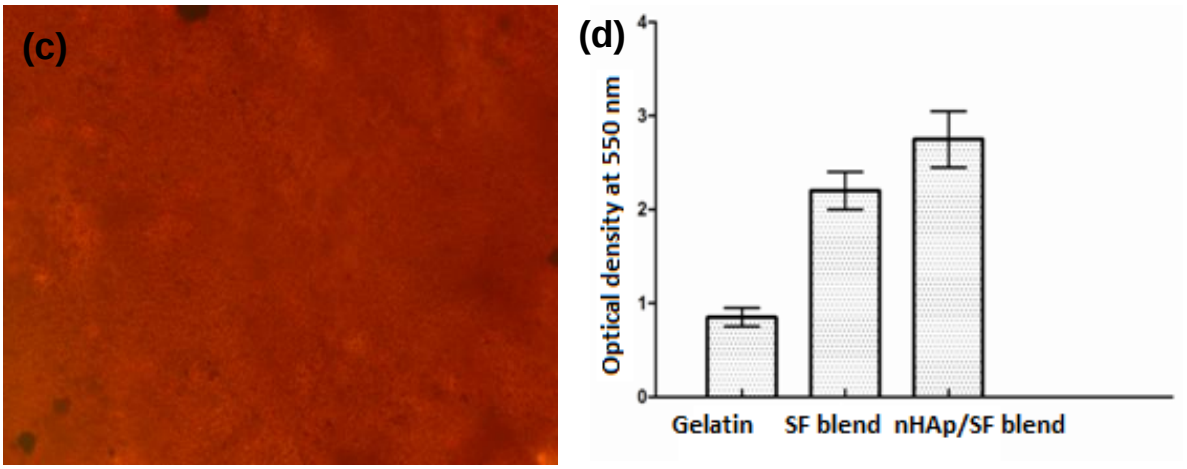

Figure 5.61: Alizarin red assay for mineralization of hMSCs on (a) gelatin (b) SF blend/ (c) SF/nHAp composite scaffolds and (d) their quantitative estimation

The higher osteogenic potential of SF/nHAp scaffold, may be explained as follows-the osteoblast-like cells express calcium receptors [223] and therefore, reside in bone matrix consisting of HAp crystals playing a significant role in osteogenic differentiation. It is reported that the adsorption of proteins and other biologically active molecules to HAp is different than pure SF blend. These proteins and biologically active molecules may mediate the interaction between cells and scaffolds resulting in a difference in osteogenic potential of the scaffolds [224].

Morphological study of differentiated MSCs

Figure 5.62 shows the differentiated MSCs cultured over different nanofibrous matrices for 21 and 28 days of culture. Immunefluorescence study demonstrated the differentiated osteoblast (osteocytes) over gelatin (a & d), SF/nHAp (b & e), SF blend (c & f) after 21 and 28 days respectively. Osteocyte count confirmed that SF/nHAp scaffolds possess maximum number of osteocytes as compared to SF scaffold showing the osteogenic superiority of SF/nHAp scaffold.

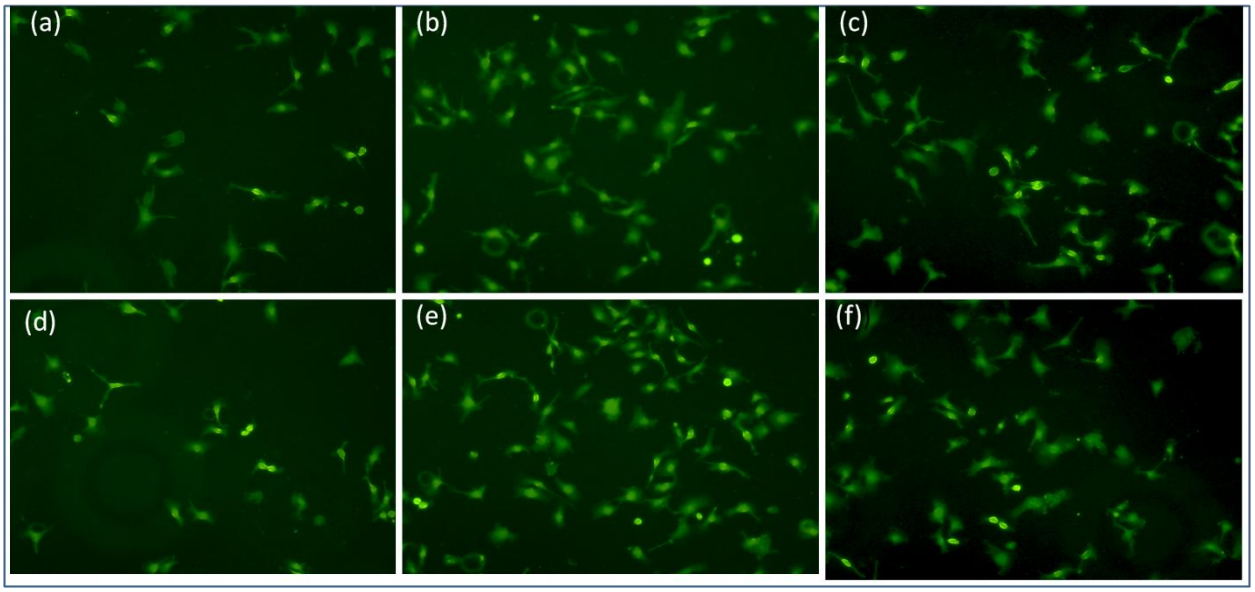

Figure 5.62: Fluorescence microscopy images of differentiated MSCs over (a) & (d) gelatin, (b) & (e) SF/nHAp composite (c) & (f) SF blend scaffolds after 21 and 28 days of treatment with osteogenic medium. The differentiated MSCs show osteocyte like morphology

Together with the mineralized nanofibrous SF blend scaffold (SF/nHAp) has shown enhanced osteogenic differentiation ability of hMSCs derived from umbilical cord blood. Thus, it is proved that the SF/nHAp composite scaffold seeded with hMSCs will be useful to provide tissue engineered construct for repairing various bone defects and diseases.

CHAPTER 6

Summary and Conclusion

In recent years bone tissue engineering has emerged as an alternative but most promising approach for repairing diseased or damaged bone tissue. The design and fabrication of a functional 3D scaffold from a variety of biopolymers that can mimic the porous structure and extracellular matrix function of bone is one of the key challenges in bone tissue engineering. SF derived from silk cocoon is considered as a potential biopolymer because of its high mechanical strength, desired surface and biological property. So far SF derived from *B. Mori* has been widely used for research by the scientists worldwide. However, *B. mori* SF lacks in cell supportive property because of its low hydrophilicity and RGD content that limit their use in tissue engineering. So effort must be given to obtain SF with superior surface property from other varieties of silk cocoons. It is further evident that a single biomaterial may not possess all the desired properties of scaffold and thus there is need for the development of a polymer blend and/or composite material with an appropriate composition from suitable biopolymers and other biomaterials. In this context, nHAp is reported to be an attractive component for developing polymer composite for bone tissue regeneration.

Besides material properties, structural characteristics of the scaffold is an another important aspect as the macroporous feature of scaffold cannot exactly mimic the dimension scale of the ECM and as a result most of the scaffolds do not recapitulate the cell microenvironment for the proper proliferation, differentiation and neo tissue formation. In this context, artificial ECM made from polymeric nanofibers is considered as the most favorable feature for tissue regeneration because nanofibers have more resemblance with body tissue that can mimic ECM to a greater extent. Keeping the above issue, the main aim of this dissertation work was to develop a potential SF biopolymer and its composites (using nHAp) with better surface property, desired mechanical and biological properties for its use in bone tissue engineering.

The most encouraging results achieved from this research are summarized as follows:

i. In this phase of research, an attempt has been made to explore and develop SF biopolymers from two locally grown silk cocoons namely eri (*P. ricini*) and tasar (*A. myilitta*). First of all, SFs from both varieties of silk cocoons were extracted by standard degumming method and lyophilized. Then a suitable solvent system was selected based on the solubility and spinnability of silk fibroins and a spinnable SF blend solution with optimum blend ratio of eri:tasar 70:30 (w/w) was prepared using the selected solvent system with composition

choloform:formic acid of 40:60 (v/v). Finally, randomly oriented SF blend nanofibers were generated by electrospinning method and characterized. SF blend solution 8% w/v was found to be the most favourable concentration for nanofiber formation. The average diameter of nanofiber is 350 nm, the range being 300-500 nm.

ii. The second phase of research work includes the fabrication and characterization of 3D nanofibrous scaffold from spinnable SF blend solution which was developed in the phase I. The nanofibrous scaffold of thickness 300 μm was prepared by electrospinning of SF blend solution. The average pore size and porosity of the scaffold were measured as 2-6 μm and 76±5% respectively. The ultimate tensile strength and % elongation of the scaffold are 1.76 MPa and 7.776%. The scaffold possesses desirable surface property as assessed by swelling and contact angle measurements. The scaffold is proved to be suitable for not-load bearing bone tissue regeneration based on the above physicochemical characterization.

iii. In this phase, the degradation mechanism of electro spun SF nanofibrous mat was studied. It has been found that the amorphous region containing hydrophilic amino acid with bulky side chain were first degraded resulting release of stable crystal blocks which has been removed from the solution without being degraded. Further it has been observed that besides β-sheet content hydrophilic amino acid content as well as available nano structures (nanofibrils) play a dominant role in degradation of silk fibroin nanofibers. Based on this mechanism, SF with more controllable degradation behavior can be established.

iv. In this part of thesis work, the developed SF scaffolds were further characterized for their cell supportive property by in vitro cell culture study. The scaffold has shown excellent cell attachment, cell proliferation and cellular metabolic activity. The scaffold has further exhibited its osteoinductive property as confirmed by ALP activity, biomineralisation assay, osteocalcein and RUNX2 expression representing the suitability of the scaffold for bone tissue engineering. The scaffold has also shown better surface and osteoductive property than the SF scaffold derived from most widely used *B. Mori* silk.

In this phase, the osteogenic property of the developed SF blend scaffold was further improved by the deposition of nHAp on the surface of nanofibers to make the scaffold more potential for bone tissue engineering application. The HAp with 30-50 nm size was deposited on the scaffold

by surface precipitation method. Similar to SF blend scaffold, the composite scaffold was characterized for surface, mechanical and biological property and the results were compared with the results obtained with pure SF blend scaffold. It has been demonstrated that the developed composite scaffold has shown improved surface property and osteogenic differentiation ability as compared to SF blend as well as the widely used SF scaffold derived from *B. mori*. Overall, in this study a novel 3D electrospun nanofibrous scaffold has been developed from SF blend that was derived from two locally grown silk cocoons such as eri and Tasar. The surface and osteoinductive property of the scaffolds were further improved by nHAp deposition and thus SF/HAp scaffold were developed. In conclusion, the results suggest that the developed SF blend derived from eri and tasar can be used as a base polymeric scaffold material for various tissue engineering applications including bone tissue regeneration. Further, SF/nHAp nanostructure developed in this study can pave the way to provide a promising scaffold exclusively for bone tissue engineering in future.

Future work

The developed eri-tasar scaffold can be further modified for proper vascularization. 3D designing of the scaffold with different geometry can be done by adopting layer-by-layer deposition method. The prepared nanofibrous scaffold can be further coated with different bioactive molecules to develop smart material with improved property for bone tissue engineering application. Further, in vivo preclinical trial may be given for biocompatibility study.

Bibliography

1. Mow, V.C. and R. Huiskers, Basic orthopaedic biomechanics and mechano-biology. 2005: Lippincott Williams & Wilkins.
2. Stroncek, J.D. and W.M. Reichert, Overview of wound healing in different tissue types. Indwelling Neural Implants: Strategies for contending with the in vivo environment, 2008.
3. Hutmacher, D.W., Scaffolds in tissue engineering bone and cartilage. Biomaterials, 2000. 21(24): p. 2529-2543.
4. Cheng, K. and W.S. Kisaalita, Exploring cellular adhesion and differentiation in a micro-/nano-hybrid polymer scaffold. Biotechnology progress, 2010. 26(3): p. 838-846.
5. Levenberg, S. and R. Langer, Advances in tissue engineering. Current topics in developmental biology, 2004. 61: p. 113-134.
6. Hubbell, J.A., Materials as morphogenetic guides in tissue engineering. Current opinion in biotechnology, 2003. 14(5): p. 551-558.
7. Adams, J.C. and F.M. Watt, Regulation of development and differentiation by the extracellular matrix. DEVELOPMENT-CAMBRIDGE-, 1993. 117: p. 1183-1183.
8. Martin, P., Wound healing--aiming for perfect skin regeneration. Science, 1997. 276(5309): p. 75-81.
9. Vacanti, J.P. and R. Langer, Tissue engineering: the design and fabrication of living replacement devices for surgical reconstruction and transplantation. The Lancet, 1999. 354: p. S32-S34.
10. Pfeiffer, E., et al., The effects of glycosaminoglycan content on the compressive modulus of cartilage engineered in type II collagen scaffolds. Osteoarthritis and Cartilage, 2008. 16(10): p. 1237-1244.
11. Harley, B.A., et al., A new technique for calculating individual dermal fibroblast contractile forces generated within collagen-GAG scaffolds. Biophysical journal, 2007. 93(8): p. 2911-2922.
12. Yang, S., et al., The design of scaffolds for use in tissue engineering. Part I. Traditional factors. Tissue engineering, 2001. 7(6): p. 679-689.
13. Cascalho, M. and J.L. Platt, Xenotransplantation and other means of organ replacement. Nature Reviews Immunology, 2001. 1(2): p. 154-160.

14. Even-Ram, S., V. Artym, and K.M. Yamada, Matrix control of stem cell fate. Cell, 2006. 126(4): p. 645-647.
15. Sokolsky-Papkov, M., et al., Polymer carriers for drug delivery in tissue engineering. Advanced drug delivery reviews, 2007. 59(4): p. 187-206.
16. Ratner, B., et al., Biomaterials science: an introduction to materials in medicine. San Diego, California, 2004: p. 162-164.
17. Abbott, W.M., et al., Effect of compliance mismatch on vascular graft patency. Journal of vascular surgery, 1987. 5(2): p. 376-382.
18. Currie, L.J., J.R. Sharpe, and R. Martin, The use of fibrin glue in skin grafts and tissue-engineered skin replacements: a review. Plastic and reconstructive surgery, 2001. 108(6): p. 1713-1726.
19. Tran, R.T., et al., A new generation of sodium chloride porogen for tissue engineering. Biotechnology and applied biochemistry. 58(5): p. 335-344.
20. Ma, Z., et al., Paraffin spheres as porogen to fabricate poly (Lâ€ • lactic acid) scaffolds with improved cytocompatibility for cartilage tissue engineering. Journal of Biomedical Materials Research Part B: Applied Biomaterials, 2003. 67(1): p. 610-617.
21. Langer, J.S., Instabilities and pattern formation in crystal growth. Reviews of Modern Physics, 1980. 52(1): p. 1.
22. Frenot, A. and I.S. Chronakis, Polymer nanofibers assembled by electrospinning. Current Opinion in Colloid & Interface Science, 2003. 8(1): p. 64-75.
23. Pham, Q.P., U. Sharma, and A.G. Mikos, Electrospinning of polymeric nanofibers for tissue engineering applications: a review. Tissue engineering, 2006. 12(5): p. 1197-1211.
24. Sill, T.J. and H.A. von Recum, Electrospinning: applications in drug delivery and tissue engineering. Biomaterials, 2008. 29(13): p. 1989-2006.
25. Tirtaatmadja, V., G.H. McKinley, and J.J. Cooper-White, Drop formation and breakup of low viscosity elastic fluids: Effects of molecular weight and concentration. Physics of fluids, 2006. 18: p. 043101.
26. Fridrikh, S.V., et al., Controlling the fiber diameter during electrospinning. Physical review letters, 2003. 90(14): p. 144502-144502.
27. Yu, J.H., S.V. Fridrikh, and G.C. Rutledge, The role of elasticity in the formation of electrospun fibers. Polymer, 2006. 47(13): p. 4789-4797.

28. Friedenstein, A.J., et al., Heterotopic transplants of bone marrow. Transplantation, 1968. 6(2): p. 230-247.
29. Horwitz, E.M., et al., Clarification of the nomenclature for MSC: The International Society for Cellular Therapy position statement. Cytotherapy, 2005. 7(5): p. 393-395.
30. Erices, A., P. Conget, and J.J. Minguell, Mesenchymal progenitor cells in human umbilical cord blood. British journal of haematology, 2000. 109(1): p. 235-242.
31. Campagnoli, C., et al., Identification of mesenchymal stem/progenitor cells in human first-trimester fetal blood, liver, and bone marrow. Blood, 2001. 98(8): p. 2396-2402.
32. Tran, R.T., et al., Biodegradable Injectable Systems for Bone Tissue Engineering.
33. Kruyt, M., et al., Bone tissue engineering and spinal fusion: the potential of hybrid constructs by combining osteoprogenitor cells and scaffolds. Biomaterials, 2004. 25(9): p. 1463-1473.
34. Marra, K.G., et al., In vitro analysis of biodegradable polymer blend/hydroxyapatite composites for bone tissue engineering. Journal of biomedical materials research, 1999. 47(3): p. 324-335.
35. Yunos, D.M., O. Bretcanu, and A.R. Boccaccini, Polymer-bioceramic composites for tissue engineering scaffolds. Journal of Materials Science, 2008. 43(13): p. 4433-4442.
36. Gasser, B., About composite materials and their use in bone surgery. Injury, 2000. 31: p. D48-D53.
37. Wang, M., Developing bioactive composite materials for tissue replacement. Biomaterials, 2003. 24(13): p. 2133-2151.
38. Boccaccini, A. R., et.al., Polymer-bioceramic composites for tissue engineering scaffolds, J. Mater. Sci. 2008. 43: p. 4433-4442
39. Wang, G., et al., Construction of A Fluorescent Nanostructured Chitosan-Hydroxyapatite Scaffold by Nanocrystallon Induced Biomimetic Mineralization and Its Cell Biocompatibility. ACS Applied Materials & Interfaces, 2011. 3(5): p. 1692-1701.
40. Turco, G., et al., Alginate/hydroxyapatite biocomposite for bone ingrowth: a trabecular structure with high and isotropic connectivity. Biomacromolecules, 2009. 10(6): p. 1575-1583.
41. Maas, M., et al., Preparation of mineralized nanofibers: collagen fibrils containing calcium phosphate. Nano letters, 2011. 11(3): p. 1383-1388.

42. Zhao, F., et al., Effects of hydroxyapatite in 3-D chitosan–gelatin polymer network on human mesenchymal stem cell construct development. Biomaterials, 2006. 27(9): p. 1859-1867.
43. Peter, M., et al., Preparation and characterization of chitosan–gelatin/nanohydroxyapatite composite scaffolds for tissue engineering applications. Carbohydrate Polymers, 2010. 80(3): p. 687-694.
44. Miao, X., et al., Porous calcium phosphate ceramics modified with PLGA–bioactive glass. Materials Science and Engineering: C, 2007. 27(2): p. 274-279.
45. Miao, X., et al., Mechanical and biological properties of hydroxyapatite/tricalcium phosphate scaffolds coated with poly (lactic-co-glycolic acid). Acta Biomaterialia, 2008. 4(3): p. 638-645.
46. Kim, H.W., J.C. Knowles, and H.E. Kim, Development of hydroxyapatite bone scaffold for controlled drug release via poly (ϵ-caprolactone) and hydroxyapatite hybrid coatings. Journal of Biomedical Materials Research Part B: Applied Biomaterials, 2004. 70(2): p. 240-249.
47. Boccaccini, A., et al., Biodegradable polymer-bioceramic composite scaffolds for bone tissue engineering. J Biomed Mater Res, 2001; 55: p. 151-7
48. Chen, Q.Z., I.D. Thompson, and A.R. Boccaccini, 45S5 Bioglass< sup>®</sup>-derived glass–ceramic scaffolds for bone tissue engineering. Biomaterials, 2006. 27(11): p. 2414-2425.
49. Correia, C., et al., Development of silk-based scaffolds for tissue engineering of bone from human adipose-derived stem cells. Acta Biomaterialia, 2012. 8(7): p. 2483-2492.
50. Thomas, V., D.R. Dean, and Y.K. Vohra, Nanostructured biomaterials for regenerative medicine. Current Nanoscience, 2006. 2(3): p. 155-177.
51. Desai, T.A., Micro-and nanoscale structures for tissue engineering constructs. Medical Engineering & Physics, 2000. 22(9): p. 595-606.
52. Elsdale, T. and J. Bard, Collagen substrata for studies on cell behavior. The Journal of cell biology, 1972. 54(3): p. 626-637.
53. Folkman, J. and A. Moscona, Role of cell shape in growth control. 1978.

54. Woo, K.M., V.J. Chen, and P.X. Ma, Nano-fibrous scaffolding architecture selectively enhances protein adsorption contributing to cell attachment. Journal of Biomedical Materials Research Part A, 2003. 67(2): p. 531-537.
55. Ito, Y., et al., A composite of hydroxyapatite with electrospun biodegradable nanofibers as a tissue engineering material. Journal of bioscience and bioengineering, 2005. 100(1): p. 43-49.
56. Venugopal, J., et al., Biocomposite nanofibres and osteoblasts for bone tissue engineering. Nanotechnology, 2007. 18(5): p. 055101.
57. Venugopal, J., et al., Electrospun-modified nanofibrous scaffolds for the mineralization of osteoblast cells. Journal of Biomedical Materials Research Part A, 2008. 85(2): p. 408-417.
58. Venugopal, J.R., et al., Nanobioengineered electrospun composite nanofibers and osteoblasts for bone regeneration. Artificial organs, 2008. 32(5): p. 388-397.
59. Prabhakaran, M.P., J. Venugopal, and S. Ramakrishna, Electrospun nanostructured scaffolds for bone tissue engineering. Acta Biomaterialia, 2009. 5(8): p. 2884-2893.
60. Fini, M., et al., The healing of confined critical size cancellous defects in the presence of silk fibroin hydrogel. Biomaterials, 2005. 26(17): p. 3527-3536.
61. Sofia, S., et al., Functionalized silk-based biomaterials for bone formation. Journal of biomedical materials research, 2001. 54(1): p. 139-148.
62. Meinel, L., et al., Silk implants for the healing of critical size bone defects. Bone, 2005. 37(5): p. 688-698.
63. Rockwood, D.N., et al., Ingrowth of human mesenchymal stem cells into porous silk particle reinforced silk composite scaffolds: An in vitro study. Acta Biomaterialia, 2011. 7(1): p. 144-151.
64. Nazarov, R., H.-J. Jin, and D.L. Kaplan, Porous 3-D scaffolds from regenerated silk fibroin. Biomacromolecules, 2004. 5(3): p. 718-726.
65. Meinel, L., et al., Bone tissue engineering using human mesenchymal stem cells: effects of scaffold material and medium flow. Annals of biomedical engineering, 2004. 32(1): p. 112-122.

66. Yan, L.-P., et al., Macro/microporous silk fibroin scaffolds with potential for articular cartilage and meniscus tissue engineering applications. Acta Biomaterialia, 2012. 8(1): p. 289-301.
67. Mandal, B.B., et al., High-strength silk protein scaffolds for bone repair. Proceedings of the National Academy of Sciences, 2012. 109(20): p. 7699-7704.
68. Karageorgiou, V. and D. Kaplan, Porosity of 3D biomaterial scaffolds and osteogenesis. Biomaterials, 2005. 26(27): p. 5474-5491.
69. Singh, H., et al., Flow modelling within a scaffold under the influence of uni-axial and bi-axial bioreactor rotation. Journal of biotechnology, 2005. 119(2): p. 181-196.
70. Williams, J.M., et al., Bone tissue engineering using polycaprolactone scaffolds fabricated via selective laser sintering. Biomaterials, 2005. 26(23): p. 4817-4827.
71. Chen, Y., S. Zhou, and Q. Li, Microstructure design of biodegradable scaffold and its effect on tissue regeneration. Biomaterials, 2011. 32(22): p. 5003-5014.
72. Engler, A.J., et al., Matrix elasticity directs stem cell lineage specification. Cell, 2006. 126(4): p. 677-689.
73. Bailey, B.M., L.N. Nail, and M.A. Grunlan, Continuous gradient scaffolds for rapid screening of cell-material interactions and interfacial tissue regeneration. Acta biomaterialia.
74. Jin, H.-J. and D.L. Kaplan, Mechanism of silk processing in insects and spiders. Nature, 2003. 424(6952): p. 1057-1061.
75. Rising, A., et al., Spider silk proteins-mechanical property and gene sequence. Zoological science, 2005. 22(3): p. 273-281.
76. Zhou, C.Z., et al., Silk fibroin: structural implications of a remarkable amino acid sequence. Proteins: Structure, Function, and Bioinformatics, 2001. 44(2): p. 119-122.
77. Rockwood, D.N., et al., Materials fabrication from Bombyx mori silk fibroin. Nature protocols. 6(10): p. 1612-1631.
78. Vollrath, F. and D.P. Knight, Liquid crystalline spinning of spider silk. Nature, 2001. 410(6828): p. 541-548.
79. Lazaris, A., et al., Spider silk fibers spun from soluble recombinant silk produced in mammalian cells. Science, 2002. 295(5554): p. 472-476.

80. Sen, K. and K. Babu, Studies on Indian silk. I. Macrocharacterization and analysis of amino acid composition. Journal of applied polymer science, 2004. 92(2): p. 1080-1097.
81. Raghu, A. and S. Ananthamurthy, Nanorheology of regenerated silk fibroin solution. Bulletin of Materials Science, 2008. 31(3): p. 359-365.
82. Stevens, M.M. and J.H. George, Exploring and engineering the cell surface interface. Science, 2005. 310(5751): p. 1135-1138.
83. Ramakrishna, S., An introduction to electrospinning and nanofibers. 2005: World Scientific.
84. Chen, C., et al., Preparation of non-woven mats from all-aqueous silk fibroin solution with electrospinning method. Polymer, 2006. 47(18): p. 6322-6327.
85. Jin, H.-J., et al., Electrospinning Bombyx mori silk with poly (ethylene oxide). Biomacromolecules, 2002. 3(6): p. 1233-1239.
86. So Hyun, K., et al., Silk fibroin nanofiber. Electrospinning, properties, and structure. Polymer Journal, 2003. 35(2): p. 185-190.
87. Zarkoob, S., et al., Structure and morphology of electrospun silk nanofibers. Polymer, 2004. 45(11): p. 3973-3977.
88. Ohgo, K., et al., Preparation of non-woven nanofibers of Bombyx mori silk, Samia cynthia ricini silk and recombinant hybrid silk with electrospinning method. Polymer, 2003. 44(3): p. 841-846.
89. Li, C., et al., Electrospun silk-BMP-2 scaffolds for bone tissue engineering. Biomaterials, 2006. 27(16): p. 3115-3124.
90. Li, C., et al., Silk apatite composites from electrospun fibers. Journal of Materials Research, 2005. 20(12): p. 3374-3384.
91. Zhang, Y., et al., Chitosan nanofibers from an easily electrospinnable UHMWPEO-doped chitosan solution system. Biomacromolecules, 2007. 9(1): p. 136-141.
92. Landis, W., et al., Mineral and organic matrix interaction in normally calcifying tendon visualized in three dimensions by high-voltage electron microscopic tomography and graphic image reconstruction. Journal of structural biology, 1993. 110(1): p. 39-54.
93. Rho, J.-Y., L. Kuhn-Spearing, and P. Zioupos, Mechanical properties and the hierarchical structure of bone. Medical Engineering & Physics, 1998. 20(2): p. 92-102.

94. Wei, K., et al., Fabrication of nano-hydroxyapatite on electrospun silk fibroin nanofiber and their effects in osteoblastic behavior. Journal of Biomedical Materials Research Part A, 2011. 97(3): p. 272-280.
95. Pal, S., et al., An Emerging Functional Natural Silk Biomaterial from the only Domesticated Non-mulberry Silkworm Samia ricini. Macromolecular bioscience, 2013.
96. Altman, G.H., et al., Silk-based biomaterials. Biomaterials, 2003. 24(3): p. 401-416.
97. Sukigara, S., et al., Regeneration of Bombyx mori silk by electrospinning"part 1: processing parameters and geometric properties. Polymer, 2003. 44(19): p. 5721-5727.
98. Zhu, J., et al., Electrospinning and rheology of regenerated Bombyx mori silk fibroin aqueous solutions: The effects of pH and concentration. Polymer, 2008. 49(12): p. 2880-2885.
99. Garcia-Fuentes, M., et al., Silk fibroin/hyaluronan scaffolds for human mesenchymal stem cell culture in tissue engineering. Biomaterials, 2009. 30(28): p. 5068-5076.
100. Burdick, J.A. and R.L. Mauck, Biomaterials for Tissue Engineering Applications.
101. Sashina, E.S., et al., Structure and solubility of natural silk fibroin. Russian journal of applied chemistry, 2006. 79(6): p. 869-876.
102. Srisuwan, Y. and P. Srihanam, Dissolution of Philosamia ricini silk film: properties and functions in different solutions. Journal of Applied Sciences, 2009. 9(5): p. 978-982.
103. Min, B.-M., et al., Formation of silk fibroin matrices with different texture and its cellular response to normal human keratinocytes. International journal of biological macromolecules, 2004. 34(5): p. 223-230.
104. Sukigara, S., et al., Regeneration of< i> Bombyx mori</i> silk by electrospinning—part 1: processing parameters and geometric properties. Polymer, 2003. 44(19): p. 5721-5727.
105. Jin, H.-J., et al., Human bone marrow stromal cell responses on electrospun silk fibroin mats. Biomaterials, 2004. 25(6): p. 1039-1047.
106. Puelacher, W., et al., Femoral shaft reconstruction using tissue-engineered growth of bone. International journal of oral and maxillofacial surgery, 1996. 25(3): p. 223-228.
107. Livingston, T., P. Ducheyne, and J. Garino, In vivo evaluation of a bioactive scaffold for bone tissue engineering. Journal of biomedical materials research, 2002. 62(1): p. 1-13.

108. Zhu, L., et al., Tissue-engineered bone repair of goat-femur defects with osteogenically induced bone marrow stromal cells. Tissue engineering, 2006. 12(3): p. 423-433.

109. Kang, S.-W., et al., Surface modification with fibrin/hyaluronic acid hydrogel on solid-free form-based scaffolds followed by BMP-2 loading to enhance bone regeneration. Bone. 48(2): p. 298-306.

110. Liu, X., et al., Enhanced bone regeneration in rat calvarial defects implanted with surface-modified and BMP-loaded bioactive glass (13-93) scaffolds. Acta biomaterialia.

111. Brown, R.A. and J.B. Phillips, Cell responses to biomimetic protein scaffolds used in tissue repair and engineering. International review of cytology, 2007. 262: p. 75-150.

112. Vepari, C. and D.L. Kaplan, Silk as a biomaterial. Progress in polymer science, 2007. 32(8): p. 991-1007.

113. Duan, B., W.L. Cheung, and M. Wang, Optimized fabrication of Caâ€“P/PHBV nanocomposite scaffolds via selective laser sintering for bone tissue engineering. Biofabrication. 3(1): p. 015001.

114. Fratzl, P., et al., Structure and mechanical quality of the collagenâ€“mineral nano-composite in bone. Journal of Materials Chemistry, 2004. 14(14): p. 2115-2123.

115. Jin, H.-J., et al., Biomaterial Films of Bombyx M ori Silk Fibroin with Poly (ethylene oxide). Biomacromolecules, 2004. 5(3): p. 711-717.

116. Stewart, R.J. and C.S. Wang, Adaptation of caddisfly larval silks to aquatic habitats by phosphorylation of h-fibroin serines. Biomacromolecules. 11(4): p. 969-974.

117. Kearns, V., et al., Silk-based biomaterials for tissue engineering. Topics in tissue engineering, 2008. 4: p. 5.

118. Mandal, B.B. and S.C. Kundu, • Bioengineered silk gland fibroin protein: Characterization and evaluation of matrices for potential tissue engineering applications. Biotechnology and bioengineering, 2008. 100(6): p. 1237-1250.

119. Datta, A., A.K. Ghosh, and S.C. Kundu, Differential expression of the fibroin gene in developmental stages of silkworm, Antheraea mylitta (Saturniidae). Comparative Biochemistry and Physiology Part B: Biochemistry and Molecular Biology, 2001. 129(1): p. 197-204.

120. Xiaosong, Gu., et. Al., "The effects of different sterilization methods on silk fibroin." Journal of Biomedical Science and Engineering 4, (2011): 4(5) p. 397-402.

121. Cao, Z., et al., The preparation of regenerated silk fibroin microspheres. Soft Matter, 2007.3(7): p. 910-915.

122. Ki, C.S., et al., Characterization of gelatin nanofiber prepared from gelatin–formic acid solution. Polymer, 2005. 46(14): p. 5094-5102.

123. Min, B.-M., et al., Electrospinning of silk fibroin nanofibers and its effect on the adhesion and spreading of normal human keratinocytes and fibroblasts in vitro. Biomaterials, 2004. 25(7): p. 1289-1297.

124. Lowery, J.L., Characterization and modification of porosity in electrospun polymeric materials for tissue engineering applications, 2009, Massachusetts Institute of Technology.

125. Lu, Q., et al., Degradation mechanism and control of silk fibroin. Biomacromolecules, 2011. 12(4): p. 1080-1086.

126. Andiappan, M., et al., Electrospun eri silk fibroin scaffold coated with hydroxyapatite for bone tissue engineering applications. Progress in Biomaterials, 2013. 2(1): p. 6.

127. Skinner, F., Y. Rotenberg, and A. Neumann, Contact angle measurements from the contact diameter of sessile drops by means of a modified axisymmetric drop shape analysis. Journal of colloid and interface science, 1989. 130(1): p. 25-34.

128. Zhu, H., et al., Fabrication and characterization of bioactive silk fibroin/wollastonite composite scaffolds. Materials Science and Engineering: C, 2010. 30(1): p. 132-140.

129. Wongnarat, C. and P. Srihanam, Degradation Behaviors of Thai Bombyx mori Silk Fibroins Exposure to Protease Enzymes, 2013. 5(1). P. 61-66

130. Fuss, I.J., et al., Isolation of whole mononuclear cells from peripheral blood and cord blood. Current protocols in immunology, 2009: p. 7.1. 1-7.1. 8.

131. Cartmell, S.H., et al., Effects of medium perfusion rate on cell-seeded three-dimensional bone constructs in vitro. Tissue engineering, 2003. 9(6): p. 1197-1203.

132. Wang, H., et al., Biocompatibility and osteogenesis of biomimetic nano-hydroxyapatite/polyamide composite scaffolds for bone tissue engineering. Biomaterials, 2007. 28(22): p. 3338-3348.

133. Hedley, D.W., et al., Method for analysis of cellular DNA content of paraffin-embedded pathological material using flow cytometry. Journal of Histochemistry & Cytochemistry, 1983. 31(11): p. 1333-1335.

134. Schagemann, J.C., et al., The effect of scaffold composition on the early structural characteristics of chondrocytes and expression of adhesion molecules. Biomaterials, 2010. 31(10): p. 2798-2805.

135. Lisignoli, G., et al., Hyaluronan-based polymer scaffold modulates the expression of inflammatory and degradative factors in mesenchymal stem cells: Involvement of Cd44 and Cd54. Journal of cellular physiology, 2006. 207(2): p. 364-373.

136. Ravichandran, R., et al., Precipitation of nanohydroxyapatite on PLLA/PBLG/Collagen nanofibrous structures for the differentiation of adipose derived stem cells to osteogenic lineage. Biomaterials, 2012. 33(3): p. 846-855.

137. De Jong, J., et al., Dimethylmethylene blue-based spectrophotometry of glycosaminoglycans in untreated urine: a rapid screening procedure for mucopolysaccharidoses. Clinical chemistry, 1989. 35(7): p. 1472-1477.

138. Gregory, C.A., et al., An Alizarin red-based assay of mineralization by adherent cells in culture: comparison with cetylpyridinium chloride extraction. Analytical biochemistry, 2004. 329(1): p. 77-84.

139. Park, M.H., et al., Differential expression patterns of Runx2 isoforms in cranial suture morphogenesis. Journal of Bone and Mineral Research, 2001. 16(5): p. 885-892.

140. Sreenivasa, I. and V. MR, HL and Nadiger, GS, 2005, Development and study of the properties of Eri silk and polyester blended yarn. Man-Made Textiles India. 48(1): p. 15-18.

141. Kulkarni, A.A. and G. Mahale, Physical properties of developed viscose rayon and eri silk union fabrics. Karnataka Journal of Agricultural Sciences, 2012. 24(4).

142. Reneker, D.H. and A.L. Yarin, Electrospinning jets and polymer nanofibers. Polymer, 2008. 49(10): p. 2387-2425.

143. Luo, C., M. Nangrejo, and M. Edirisinghe, A novel method of selecting solvents for polymer electrospinning. Polymer, 2010. 51(7): p. 1654-1662.

144. Haroosh, H.J., D.S. Chaudhary, and G.D. Ingram, Effect of solution concentration and co-solvent ratio on electrospun peg fibers. Chemeca 2011: Engineering a Better World: Sydney Hilton Hotel, NSW, Australia, 18-21 September 2011, 2011: p. 1535.

145. Cheng, M.-L., et al., Processing and characterization of electrospun poly (3-hydroxybutyrate-3-hydroxyhexanoate) nanofibrous membranes. Polymer, 2008. 49(2): p. 546-553.

146. Ayutsede, J.E., Regeneration of bombyx mori silk nanofibers and nanocomposite fibrils by the electrospinning process, 2005, Drexel University.

147. Fuller, C.S., Frontiers in Chemistry, Volume I—The Chemistry of Large Molecules (Burk, RE; Grummitt, Oliver; eds.). Journal of Chemical Education, 1943. 20(9): p. 466.

148. Tan, E., S. Ng, and C. Lim, Tensile testing of a single ultrafine polymeric fiber. Biomaterials, 2005. 26(13): p. 1453-1456.

149. Shenoy, S.L., W.D. Bates, and G. Wnek, Correlations between electrospinnability and physical gelation. Polymer, 2005. 46(21): p. 8990-9004.

150. Van der Schueren, L., et al., An alternative solvent system for the steady state electrospinning of polycaprolactone. European Polymer Journal, 2011. 47(6): p. 1256-1263.

151. Haroosh, H.J., D.S. Chaudhary, and Y. Dong, Effect of solution parameters on electrospun PLA/PCL fibers. Chemeca 2011: Engineering a Better World: Sydney Hilton Hotel, NSW, Australia, 18-21 September 2011, 2011: p. 1525.

152. McKee, M.G., C.L. Elkins, and T.E. Long, Influence of self-complementary hydrogen bonding on solution rheology/electrospinning relationships. Polymer, 2004. 45(26): p. 8705-8715.

153. Colby, R.H., et al., Effects of concentration and thermodynamic interaction on the viscoelastic properties of polymer solutions. Macromolecules, 1991. 24(13): p. 3873-3882.

154. Demir, M.M., et al., Electrospinning of polyurethane fibers. Polymer, 2002. 43(11): p. 3303-3309.

155. Sell, S., et al., Extracellular matrix regenerated: tissue engineering via electrospun biomimetic nanofibers. Polymer International, 2007. 56(11): p. 1349-1360.

156. Ranjan, A. and T.J. Webster, Increased endothelial cell adhesion and elongation on micron-patterned nano-rough poly (dimethylsiloxane) films. Nanotechnology, 2009. 20(30): p. 305102.

157. Curtis, A. and C. Wilkinson, Topographical control of cells. Biomaterials, 1997. 18(24): p. 1573-1583.

158. Lowery, J.L., N. Datta, and G.C. Rutledge, Effect of fiber diameter, pore size and seeding method on growth of human dermal fibroblasts in electrospun poly (ε-caprolactone) fibrous mats. Biomaterials, 2010. 31(3): p. 491-504.

159. Van Bael, S., et al., The effect of pore geometry on the in vitro biological behavior of human periosteum-derived cells seeded on selective laser-melted Ti6Al4V bone scaffolds. Acta Biomaterialia, 2012. 8(7): p. 2824-2834.

160. Shinsako, K., et al., Effects of bead size and polymerization in PMMA bone cement on vancomycin release. Bio-Medical Materials and Engineering, 2008. 18(6): p. 377-385.

161. Ren, Y., et al., Preparation and characterization of Antheraea pernyi silk fibroin based nanohydroxyapatite composites. Journal of bioactive and compatible polymers, 2007. 22(5): p. 465-474.

162. Ho, M.-p., H. Wang, and K.-t. Lau. Thermal properties and structure conformation on silkworm silk fibre. in Proceedings of the Composites Australia and CRC-ACS Conference (CRCACS 2012). 2012. Composites Australia.

163. Lindahl, O. (1976) Mechanical properties of dried defatted spongy bone. Acta orthop. stand. *47,* I I-19.

164. Evans, F. G. and King, A. L. (1961) Regional ditTerences in some physical properties of human spongy bone. Biomechunical Studies of the Musculo-Skeletal System (Edited by Evans, F. G.) pp. 49-67. C. C. Thomas, Springfield, IL.

165. Marques, A., Biofunctionality and immunocompatibility of starch-based biomaterials. 2004.

166. Davies, J. and N. Baldan, Scanning electron microscopy of the bone-bioactive implant interface. Journal of biomedical materials research, 1997. 36(4): p. 429-440.

167. Marcolongo, M., et al., Bioactive glass fiber/polymeric composites bond to bone tissue. Journal of biomedical materials research, 1998. 39(1): p. 161-170.

168. Lee, I.-S., et al., Various Ca/P ratios of thin calcium phosphate films. Materials Science and Engineering: C, 2002. 22(1): p. 15-20.

169. Tofighi AN, Krause M, Lee DD. Machinable preformed calcium phosphate bone substitute material implants. Google Patents; 2005.

170. Cao, Y. and B. Wang, Biodegradation of silk biomaterials. International journal of molecular sciences, 2009. 10(4): p. 1514-1524.

171. Gellynck, K., et al., Biocompatibility and biodegradability of spider egg sac silk. Journal of Materials Science: Materials in Medicine, 2008. 19(8): p. 2963-2970.

172. Li, X., P.T. Eles, and C.A. Michal, Water Permeability of Spider Dragline Silk. Biomacromolecules, 2009. 10(5): p. 1270-1275.

173. Zhou, P., et al., Structure of Bombyx mori silk fibroin based on the DFT chemical shift calculation. The Journal of Physical Chemistry B, 2001. 105(50): p. 12469-12476.

174. Hu, X., D. Kaplan, and P. Cebe, Determining beta-sheet crystallinity in fibrous proteins by thermal analysis and infrared spectroscopy. Macromolecules, 2006. 39(18): p. 6161-6170.

175. Wilson, D., R. Valluzzi, and D. Kaplan, Conformational transitions in model silk peptides. Biophysical journal, 2000. 78(5): p. 2690-2701.

176. Rajkhowa, R., et al., Structure and biodegradation mechanism of milled Bombyx mori silk particles. Biomacromolecules, 2012. 13(8): p. 2503-2512.

177. Lu, Q., et al., Silk Self-Assembly Mechanisms and Control From Thermodynamics to Kinetics. Biomacromolecules, 2012. 13(3): p. 826-832.

178. Szakonyi, G. and R. Zelkó, The effect of water on the solid state characteristics of pharmaceutical excipients: Molecular mechanisms, measurement techniques, and quality aspects of final dosage form. International journal of pharmaceutical investigation, 2012. 2(1): p. 18.

179. Tanaka, M., et al., Cold crystallization of water in hydrated poly (2-methoxyethyl acrylate)(PMEA). Polymer International, 2000. 49(12): p. 1709-1713.

180. Scrivener, K. and J.P. Skalny, Conclusions of the international RILEM TC 186-ISA workshop on internal sulfate attack and delayed ettringite formation ("6 September 2002, Villars, Switzerland). Materials and structures, 2005. 38(6): p. 659-663.

181. Esch, D.C., Thermal analysis, construction, and monitoring methods for frozen ground. Vol. 9. 2004: ASCE Publications.

182. Berlin, E., P.G. Kliman, and M.J. Pallansch, Effect of sorbed water on the heat capacity of crystalline proteins. Thermochimica Acta, 1972. 4(1): p. 11-16.

183. Mrevlishvili, G.M., Low-temperature heat capacity of biomacromolecules and the entropic cost of bound water in proteins and nucleic acids (DNA). Thermochimica Acta, 1998. 308(1): p. 49-54.

184. Kim, J.H., et al., Preparation and in vivo degradation of controlled biodegradability of electrospun silk fibroin nanofiber mats. Journal of Biomedical Materials Research Part A, 2012. 100(12): p. 3287-3295.

185. Hu, X., D. Kaplan, and P. Cebe, Dynamic protein' water relationships during β-sheet formation. Macromolecules, 2008. 41(11): p. 3939-3948.

186. Hoyt, M.A., et al., Glycine"alanine repeats impair proper substrate unfolding by the proteasome. The EMBO journal, 2006. 25(8): p. 1720-1729.

187. Patel, K. and R.T. Borchardt, Chemical pathways of peptide degradation. III. Effect of primary sequence on the pathways of deamidation of asparaginyl residues in hexapeptides. Pharmaceutical research, 1990. 7(8): p. 787-793.

188. Park, S.-H., et al., Relationships between degradability of silk scaffolds and osteogenesis. Biomaterials, 2010. 31(24): p. 6162-6172.

189. Patra, C., et al., Silk protein fibroin from Antheraea mylitta for cardiac tissue engineering. Biomaterials, 2012. 33(9): p. 2673-2680.

190. Yamaguchp, H., et al., Role of umbilical vein endothelial cells in hematopoiesis. Leukemia & lymphoma, 1998. 31(1-2): p. 61-69.

191. Yang, M.-C., et al., The influence of rat mesenchymal stem cell CD44 surface markers on cell growth, fibronectin expression, and cardiomyogenic differentiation on silk fibroin–hyaluronic acid cardiac patches. Biomaterials, 2010. 31(5): p. 854-862.

192. Zinger, O., et al., Time-dependent morphology and adhesion of osteoblastic cells on titanium model surfaces featuring scale-resolved topography. Biomaterials, 2004. 25(14): p. 2695-2711.

193. Dalby, M., et al., Investigating the limits of filopodial sensing: a brief report using SEM to image the interaction between 10 nm high nano-topography and fibroblast filopodia. Cell biology international, 2004. 28: p. 229-236.

194. Maag, R.S., S.W. Hicks, and C.E. Machamer, Death from within: apoptosis and the secretory pathway. Current opinion in cell biology, 2003. 15(4): p. 456-461.

195. Lee, J.W., W.N. Qi, and S.P. Scully, The involvement of β1 integrin in the modulation by collagen of chondrocyte-response to transforming growth factor-β1. Journal of orthopaedic research, 2002. 20(1): p. 66-75.

196. Loeser, R.F., Integrins and cell signaling in chondrocytes. Biorheology, 2002. 39(1): p. 119-124.

197. Kim, Y.J., et al., A study of compatibility between cells and biopolymeric surfaces through quantitative measurements of adhesive forces. Journal of Biomaterials Science, Polymer Edition, 2003. 14(12): p. 1311-1321.

198. Burridge, K. and M. Chrzanowska-Wodnicka, Focal adhesions, contractility, and signaling. Annual review of cell and developmental biology, 1996. 12(1): p. 463-519.

199. Knudson, W. and R. Loeser, CD44 and integrin matrix receptors participate in cartilage homeostasis. Cellular and Molecular Life Sciences CMLS, 2002. 59(1): p. 36-44.

200. Biggs, M. and M. Dalby, Focal adhesions in osteoneogenesis. Proceedings of the Institution of Mechanical Engineers, Part H: Journal of Engineering in Medicine, 2010. 224(12): p. 1441-1453.

201. Anderson, H.C., et al., Impaired calcification around matrix vesicles of growth plate and bone in alkaline phosphatase-deficient mice. The American journal of pathology, 2004. 164(3): p. 841-847.

202. Liu, F., L. Malaval, and J.E. Aubin, Global amplification polymerase chain reaction reveals novel transitional stages during osteoprogenitor differentiation. Journal of cell science, 2003. 116(9): p. 1787-1796.

203. Heinemann, C., et al., Novel textile chitosan scaffolds promote spreading, proliferation, and differentiation of osteoblasts. Biomacromolecules, 2008. 9(10): p. 2913-2920.

204. Manton, K.J., et al., Glycosaminoglycan and growth factor mediated murine calvarial cell proliferation. Journal of molecular histology, 2007. 38(5): p. 415-424.

205. Salbach, J., et al., Regenerative potential of glycosaminoglycans for skin and bone. Journal of molecular medicine. 90(6): p. 625-635.

206. Cassella, J.P., et al., An electron probe X-ray microanalytical study of bone mineral in osteogenesis imperfecta. Calcif Tissue Int, 1995. 56(2): p. 118-22.

207. Binulal, N., et al., Role of nanofibrous poly (caprolactone) scaffolds in human mesenchymal stem cell attachment and spreading for in vitro bone tissue engineering—response to osteogenic regulators. Tissue Engineering Part A, 2010. 16(2): p. 393-404.

208. Komori, T., Regulation of osteoblast differentiation by transcription factors. Journal of cellular biochemistry, 2006. 99(5): p. 1233-1239.

209. Hattar, S., et al., Potential of biomimetic surfaces to promote in vitro osteoblast-like cell differentiation. Biomaterials, 2005. 26(8): p. 839-848.

210. Varma, H.K., S.N. Kalkura, and R. Sivakumar, Polymeric precursor route for the preparation of calcium phosphate compounds. Ceramics international, 1998. 24(6): p. 467-470.

211. Yu, H.-S., S.-J. Hong, and H.-W. Kim, Surface-mineralized polymeric nanofiber for the population and osteogenic stimulation of rat bone-marrow stromal cells. Materials Chemistry and Physics, 2009. 113(2): p. 873-877.

212. Cassella, J., et al., An electron probe X-ray microanalytical study of bone mineral in osteogenesis imperfecta. Calcified tissue international, 1995. 56(2): p. 118-122.

213. Suchanek, W. and M. Yoshimura, Processing and properties of hydroxyapatite-based biomaterials for use as hard tissue replacement implants. Journal of Materials Research, 1998. 13(01): p. 94-117.

214. Kim, H.-W., H.-E. Kim, and V. Salih, Stimulation of osteoblast responses to biomimetic nanocomposites of gelatin–hydroxyapatite for tissue engineering scaffolds. Biomaterials, 2005. 26(25): p. 5221-5230.

215. Kikuchi, M., et al., Self-organization mechanism in a bone-like hydroxyapatite/collagen nanocomposite synthesized in vitro and its biological reaction in vivo. Biomaterials, 2001. 22(13): p. 1705-1711.

216. Tampieri, A., et al., Biologically inspired synthesis of bone-like composite: Self-assembled collagen fibers/hydroxyapatite nanocrystals. Journal of Biomedical Materials Research Part A, 2003. 67(2): p. 618-625.

217. Zhao, Y., et al., Nonwoven silk fibroin net/nano-hydroxyapatite scaffold: Preparation and characterization. Journal of Biomedical Materials Research Part A, 2009. 91(4): p. 1140-1149.

218. Dhandayuthapani, B., et al., Evaluation of antithrombogenicity and hydrophilicity on Zein-SWCNT electrospun fibrous nanocomposite scaffolds. International journal of biomaterials, 2012.

219. Wang, B., L. Li, and Y. Zheng, In vitro cytotoxicity and hemocompatibility studies of Ti-Nb, Ti-Nb-Zr and Ti-Nb-Hf biomedical shape memory alloys. Biomedical Materials, 2010. 5(4): p. 044102.

220. Zhao, X., et al., Cytotoxicity of hydroxyapatite nanoparticles is shape and cell dependent. Archives of toxicology, 2012: p. 1-16.

221. Havens, C.G., et al., Regulation of late G1/S phase transition and APCCdh1 by reactive oxygen species. Molecular and cellular biology, 2006. 26(12): p. 4701-4711.

222. Xue, R., et al., Effects of matrix elasticity and cell density on human mesenchymal stem cells differentiation. Journal of Orthopaedic Research, 2013.

223. Leis, H., et al., Extracellular Ca2+ sensing by the osteoblast-like cell line, MC3T3-E1. Cell Calcium, 1994. 15(6): p. 447-456.

224. Ma, P.X., et al., Engineering new bone tissue in vitro on highly porous poly (α-hydroxyl acids)/hydroxyapatite composite scaffolds. Journal of biomedical materials research, 2001. 54(2): p. 284-293.

List of Publications

I. Applied Patent

1. Panda, N.; Bissoyi, A.; Biswas, A.; Pramanik, K., "Electrospun silk fibroin blend nanofibrous scaffold and its use in tissue engineering" application no-713/kol/2012.
2. Panda, N.; Biswas, A.; Pramanik, K., "nHAp/SF construct for bone tissue engineering" application no-(To be Filed).

II. Publication in International Journals

1. Panda, N.; Biswas, A.; Pramanik, K.; Sukla, L., Degradation Mechanism and Control of blended eri and tasar silk nano fiber. *Applied Biochemistry and Biotechnology* (accepted 2014).
2. Panda, N.; Biswas, A.; Pramanik, K.; Jonnalagadda, S., Enhanced osteogenic potential of human mesenchymal stem cells on electrospun nanofibrous scaffolds prepared from eri-tasar silk fibroin. *Journal of Biomedical Materials Research Part B: Applied Biomaterials Journal* (accepted 2014).
3. Bissoyi, Akalabya, K. Pramanik, N. Panda, and S. K. Sarangi., Cryopreservation of hMSCs seeded silk nanofibers based tissue engineered construct. *Cryobiology* (2014);68(3):332-342.
4. Biswas, A.; Panda, N.; Bhattarai, P., Preparation and characterization of yttria stabilized zirconia (8YSZ) nanofiber for medical application. *International Journal of Enhanced Research in Science Technology & Engineering*. 2014;3(7):75-78.
5. Panda, N.; Bissoyi, A.; Biswas, A.; Pramanik, K., Directing osteogenesis of stem cells with hydroxyapatite precipitated electrospun eri-tasar silk fibroin nanofibrous scaffold. *J Biomater Sci Polym Ed*. (Accepted).
6. Panda, N.; Jonnalagadda, S.; Pramanik, K., Development and evaluation of cross-linked collagen-hydroxyapatite scaffolds for tissue engineering. *J Biomater Sci Polym Ed.* 2013;24(18):2031-44.

Biography

PERSONAL DETAILS

Name : Niladri Nath Panda
Nationality : Indian
Address : Division of Tissue Engineering
Department of Biotechnology and Medical Engineering,
National Institute of Technology,
Rourkela - 769008,
India
Mobile – 91-9439703540
E-mail: niladri1panda@gmail.com, pandan@nitrkl.ac.in

My research field involves tissue engineering and regenerative medicine pertaining to design, fabrication and simulation of a variety of scaffold material suitable for development of tissue graft. I am interested in structure-property-processing inter-relationship to modify existing polymers to improve mechanical and biological performance of biomaterials that are used in rapid wound healing and fabrication of load bearing implants. In particular, I have focused on exploring issues regarding the assistance offered by scaffold for regeneration of body tissue. For the last 4 years, my research work concentrated on polymeric biomaterials, with emphasis on orthopedic biomaterials, especially the use of biopolymer such as collagen, silk fibroin, chitosan and calcium phosphate based filler for bone and cartilage tissue regeneration. I consider myself fairly adept at solving research problems as I have over 5 years of experience in, understanding and analyzing the scientific concepts to implement research plans for possible scientific outcomes. I possess strong practical background on mammalian cell culture, morphological characterization techniques such as scanning electron microscopy, confocal laser scanning microscopy, X-ray scattering, Fourier Transform Infrared Spectroscopy, differential scanning calorimeter, mechanical testing and wear testing, project management and manuscript writing. On a personal level, I am not only curious about engineering and biological sciences but also have interest in politics, philosophy as well as religion. I am a hardworking dedicated professional and I take pride in exhibiting a strong work ethic seasoned with compassion and care for people.